The Oxidation of Zinc Vapor and Non-stoichiometric Ceria by Water and Carbon Dioxide to Produce Hydrogen and Carbon Monoxide

A DISSERTATION SUBMITTED TO THE FACULTY OF THE GRADUATE SCHOOL OF THE UNIVERSITY OF MINNESOTA BY

Luke J. Venstrom

IN PARTIAL FULFILLMENT OF THE REQUIREMENTS FOR THE DEGREE OF DOCTOR OF PHILOSOPHY

Dr. Jane H. Davidson, Advisor

June, 2012

Abstract

Experimental studies of two pathways for solar thermochemical metal oxide cycles to split water and carbon dioxide are presented. The heterogeneous oxidation of Zn(g) is investigated in Part I, and the oxidation of porous ceria is investigated in Part II.

The heterogeneous oxidation of Zn(g) is proposed as an improved approach for rapid and complete oxidation of Zn. Reaction rates are measured gravimetrically in a quartz tube flow reactor at atmospheric pressure for conditions in which Zn is the limiting reactant, at temperatures between 800 and 1150 K, and for Zn(g), H_2O(g), and CO_2 partial pressures between 10^{-5} and 0.25 atm. The rate of Zn(g) oxidation by CO_2 is between 0.3×10^{-8} and 6.5×10^{-6} mol cm^{-2} s^{-1}, permitting conversions of Zn to ZnO greater than 84% in one second. The rate of Zn(g) oxidation by H_2O is between 0.8×10^{-7} and 1.5×10^{-5} mol cm^{-2} s^{-1} permitting conversions greater than ~80% in one second. A finite volume based numerical model decouples mass transfer and surface kinetics from the reaction rate data. The CO_2-splitting kinetics are second-order, proportional to the Zn(g) and CO_2 concentrations. The kinetic parameter is expressed in Arrhenius form, and the activation energy and pre-exponential factor are 44±3 kJ mol^{-1} and 92±6 mol m^{-2} s^{-1} atm^{-2}, respectively. When expressed in second-order form, the apparent activation energy and pre-exponential factor of H_2O-splitting are -110 kJ/mol and 1.8×10^{-5} mol m^{-2} s^{-1} atm^{-2} between 800 and 1050 K. At 1100 K, the activation energy becomes positive. A precursor mechanism, where the apparent activation energy is the sum of the heat of adsorption of H_2O and the activation energy of the rate-limiting kinetic step is postulated to explain this behavior. The benefit of completely converting Zn via the heterogeneous oxidation of

Zn(g) is an increase in the Zn/ZnO cycle efficiency from ~6% for polydisperse aerosol reactors, which have been limited to Zn conversions of 20% for reaction times on the order of a minute, to 27% and 31% for H_2O- and CO_2-splitting, respectively.

In Part II, the effect of material morphology on the reduction and oxidation of ceria is investigated. The oxidation by H_2O and CO_2 of three-dimensionally ordered macroporous ceria (3DOM CeO_2), which features an interconnected, ordered pore network, solid feature sizes between 80 and 200 nm, and a moderate specific surface area of 10 m^2 g^{-1}, is compared to the oxidation of non-ordered mesoporous ceria and sintered, low porosity ceria at 1100 K in 6 isothermal chemical cycles. The 3DOM CeO_2 increases the maximum H_2 and CO production rates over the low porosity CeO_2 by 125 and 260%, and increases the maximum H_2 and CO production rates over the non-ordered mesoporous CeO_2 by 75 and 175%. 3DOM CeO_2, non-ordered macroporous ceria (NOM CeO_2), and aggregates of ceria nanoparticles are also cyclically reduced at ~1500 K under $p_{O_2} = 10^{-5}$ atm and oxidized at ~1100 K by 25 mol% CO_2. The 3DOM and NOM CeO_2 retain an interconnected, disordered pore network and achieve maximum CO production rates of 6.4 and 4.0 mL min^{-1} g^{-1}, respectively, an order of magnitude increase over the ~0.1 mL min^{-1} g^{-1} rate of CO production of the sintered ceria nanoparticles and low porosity ceria. The present study demonstrates the importance of engineering ceria with interconnected porosity and solid feature sizes on the order of hundreds of nm.

Acknowledgements

Without my faith in God's unconditional love for me and all people, I would not have completed my journey through graduate school. I give God the glory for the contents of this dissertation.

I have been blessed with a companion in life who is patient, supportive, and understanding. She has been with me through the good and through the bad, and her unwavering love during my graduate studies will never be forgotten. To my wife, Laura, I say thank you.

I would like to thank my advisor, Prof. Jane H. Davidson, for the opportunity to join her in conducting cutting-edge research in the solar thermochemistry field. Her expert guidance has significantly enhanced my scholarship, and perhaps totally reconstructed it. I will continue to aspire to be more like her as a scientist, speaker, teacher, and writer.

I would also like to thank Prof. Andreas Stein, and his students Nick Petkovich and Stephen Rudisill, for their partnership in interdisciplinary research. I learned a great deal through our collaboration.

My colleagues in the Solar Energy Laboratory have enhanced my graduate student experience on many levels. For countless discussions initiated on a whim and helpful advice, I thank Josh Quinnell, Brandon Hathaway, Julia Nicodemus, Dan Keene, Katie Krueger, and Peter Krenzke. Their friendship made coming to the Solar Energy Laboratory more enjoyable.

My family and friends have been a constant source of support for me throughout my life. For their confidence and encouragement, I say thank you.

I must also thank a number of faculty at Valparaiso University. Prof. Robert Palumbo invited me to do research with him as an undergraduate, and his invitation changed the course of my life. He will forever receive from me a plethora of thanks. I also thank Prof. Scott Duncan and Prof. Carmine Polito for their support.

Table of Contents

List of Tables

List of Figures

Nomenclature

Roman letters

A	material flow rate [mol s^{-1}]
a	kinetic parameter in equation (2.5), [mol cm^{-2} s^{-1} atm^{-2}]
C	solar concentration ratio [suns]
$\bar{c}_p$	specific molar heat [kJ mol^{-1} K^{-1}]
D	diffusion coefficient [m^2 s^{-1}]
$\widetilde{D}$	chemical, or ambipolar, diffusion coefficient [cm^2 s^{-1}]
$\mathfrak{D}$	diffusivity [m^2 s^{-1}]
$\mathcal{D}_e$	effective intraparticle diffusion coefficient[cm^2 s^{-1}]
d	diameter [mm] or kinetic parameter in equation (2.5), [mol cm^{-2} s^{-1} $atm^{-3/2}$]
$\dot{E}$	rate of energy transfer [kW] or [kJ mol^{-1}]
EN	endothermic reaction step
EX	exothermic reaction step
F	parameter in fully-developed annulus flow velocity profile [kg m s^{-2}]
f	functional relationship
$\bar{G}$	Gibbs free energy [kJ mol^{-1}]
g_{fit}	objective function for mass transfer model optimization
$\bar{H}$	enthalpy [kJ mol^{-1}]
$\bar{h}_f^o$	standard enthalpy of formation [kJ mol^{-1}]
I	terrestrial solar constant, 1000 W m^{-2}
J	diffusion of species [kg m^{-2} s^{-1}]
k	reaction rate parameter, units in context
K	equilibrium constant
L	length [m], [cm], or [mm]
M	molecular weight [g mol^{-1}]
m	mass [kg]
$\dot{m}$	mass flow rate [kg s^{-1}]
N	moles of substance [mol] or number of gas phase constituents
$\dot{n}$	molar flow rate [mol s^{-1}]
P	thermodynamic pressure [bar] or [atm]
p	partial pressure [bar] or [atm]
$\dot{Q}$	net heat transfer rate [kW] or [kJ mol^{-1}]

Q	volumetric gas flow rate [mL min^{-1}]
R	oxidation tube radius [mm]
R_u	universal gas constant, 8.314 J mol^{-1} K^{-1}
Re	Reynolds number
r	reaction rate [mol s^{-1}], or radial coordinate [mm]
$\bar{S}$	entropy [kJ mol^{-1} K^{-1}]
$\dot{S}$	rate of entropy generation, or irreversibility [kW K^{-1}] or [kJ mol^{-1}]
$\bar{s}^o$	standard entropy [kJ mol^{-1} K^{-1}]
T	temperature [K]
t	time [s] or [min]
u	gas velocity in the axial direction [m s^{-1}]
$\vec{u}$	gas velocity vector [m s^{-1}]
U	mass average velocity [m s^{-1}]
V	volume [m^3]
v	gas velocity in the radial direction [m s^{-1}]
$\dot{W}$	rate of work [kW] or [kJ mol^{-1}]
X_{Zn}	conversion of Zn
y	mole fraction in gas phase
z	axial coordinate, mm

Greek letters

α	fraction of Zn converted to ZnO
β	yield of Zn from the solar reactor quencher
Δ	indicates a change in a quantity
∇	gradient operator
δ	ceria non-stoichiometry (in reference to $CeO_{2-\delta}$), moles of oxygen vacancies per mole of ceria
η	efficiency [%]
μ	gas viscosity [kg m^{-1} s^{-1}]
$\tilde{\mu}$	mobility [cm^2 V^{-1} s^{-1}]
ν	stoichiometric coefficient in reaction
Ψ	reaction stoichiometry
ϕ	porosity
ρ	density, [kg m^{-3}]
σ	Stefan-Boltzmann constant, 5.67×10^{-8} 5.67×10^{-8} W m^{-2} K^{-4}
ω	mass fraction in gas phase
τ	first-order time constant [s]

$\bar{\tau}$	tortuosity

Subscripts

absorption	the absorption efficiency
avg	refers to an average quantity
b	backward reaction rate constant, or outer diameter of capillary tube
Carnot	the Carnot efficiency
cycle	cycle efficiency, defined in equation (4.7)
CO	refers to CO product
CO_2	refers to CO_2 reactant or the CO_2 inlet
c	inner diameter of capillary tube
deposition	refers to ZnO mass deposited in the heterogeneous oxidation of Zn(g)
d	duration of H_2 or CO production or time required for complete oxidation
electron	refers to an electron
eff	effective mixture diffusion coefficient
eq	refers to chemical equilibrium
fuel	H_2 or CO product
fuel cell	energy flow from the fuel cell
fuel,max	maximum rate of H_2 or CO production
furnace	the set point of the electric furnace
f	forward reaction rate constant
gen	entropy generated (irreversibility)
hydrolysis	refers to the hydrolysis of Zn (oxidation by H_2O)
h	the hydraulic diameter in an annulus
inert	refers to an inert component
in	energy input or material inflow
i	index for species in equations
j	index for species in equations
k	index for experimental data points
loss	reradiation loss from solar reactor
model	refers to reaction rate predicted in numerical model
m	refers to the reacting mixture
n	refers to direction normal to surface
oxidation	refers to the oxidizer (III in Figure 4.1) or the oxidation of Zn by CO_2
out	energy output or material outflow
o	at the initial state
pore	refers to a pore in a solid
products	refers to the products of the reaction

p	of a particle
quench	energy released in the quencher
reactants	refers to the reactants in a reaction
r	refers to the radial coordinate direction
r	refers to reduction temperature or a reaction
sensible /latent	energy required for raising temperature and changing phase of reactants
solar	solar gain or solar-based reduction of a metal oxide
s	refers to solid (CeO_2) or thermal reservoir temperature
total	fuel production integrated in over time
Zn→ZnO	energy released when unreacted Zn from oxidizer converted to ZnO
Zn	refers to Zn reactant, or the Zn inlet
ZnO	refers to ZnO product
wall	at the wall boundary in the numerical domain

Superscripts

′	per unit mass of solid CeO_2
″	per unit area
‴	per unit solid volume (in a reacting porous media)
i	chemical species entering a process
j	chemical species exiting a process
o	denotes standard thermodynamic state of 298 K, 1 atm, or, indicates a quantity at the inlet of a reactor or control volume
eq	refers to chemical equilibrium

Acronyms

3DOM	three-dimensionally ordered macroporous
D-3DOM	disassembled three-dimensionally ordered macroporous
DS	decomposition synthesized
NOM	non-ordered macroporous

1 Introduction

The world faces significant energy and environmental challenges. Energy demand is exploding while conventional fossil-based energy sources grow scarce. At the same time, continued use of fossil fuels is driving up the concentrations of greenhouse gases in the earth's atmosphere, and causing global average temperatures to increase [1]. Disruptive and sustainable energy technologies present solutions to these issues.

Solar energy is poised to play a significant role in overcoming the energy and environmental crises, but remains vastly underutilized [2]. Enough solar energy strikes the surface of just the Great Basin Desert in North America every year to meet the energy needs of the *entire planet* 6 million times over[1]. Yet, as shown in Figure 1.1, of the 8% of energy that originates from renewable sources, less than 1% is derived from the sun in the United States.

One of the challenges of utilizing the solar resource is overcoming its intermittency. An effective means of storage to buffer daily and seasonal variations in the solar resource is required. One promising approach to store solar energy is to produce fuels using concentrated sunlight as the source of process heat to drive endothermic chemical reactions. Stored as a fuel, solar energy is readily transported so that it can be used when and where it is needed. Two highly desirable fuels are hydrogen (H_2) and carbon monoxide

[1] Based on annual incident solar radiation of 1.5 MWh/m^2, worldwide annual energy demand of 130 GWh, and the area of the Great Basin Desert, 492,000 square kilometers. Note that the Great Basin Desert is the tenth largest desert in the world.

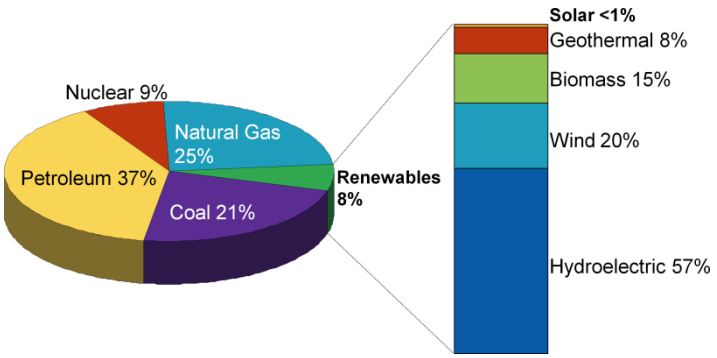

Figure 1.1 The portfolio of energy sources in the U.S.A. (source: U.S. EIA Energy Outlook 2011)

(CO) because these fuels have flexible end uses. Hydrogen can be utilized in fuel cells, H_2 and CO can be cleanly combusted to supply process heat, or H_2 and CO can be mixed to form syngas and further upgraded to liquid combustible fuels in the Fischer-Tropsch or related chemical processes. The latter is considered the *ne plus ultra* as it would provide gasoline, diesel, or jet fuels that are compatible with the existing transportation infrastructure.

The conceptually simplest process to convert solar energy into H_2 and CO is to thermally dissociate water (H_2O) and carbon dioxide (CO_2) with a concentrated beam of solar radiation. However, at atmospheric pressure, temperatures in excess of 3000 K are required to achieve practical extents of H_2O and CO_2 dissociation (Figure 1.2). Such extreme temperatures, along with the need to separate the H_2, CO, and O_2 from the product gas mixture, render direct thermolysis impractical. Direct thermolysis solar reactors achieved thermal efficiencies[2] of less than 3% primarily due to losses by reradiation at the high dissociation temperatures and inefficient product separation [3-11]. More importantly, the reactor materials degrade quickly making the outlook for long-term

[2] Thermal efficiency is defined as the ratio of the higher heating value of the H_2 or CO to the solar input.

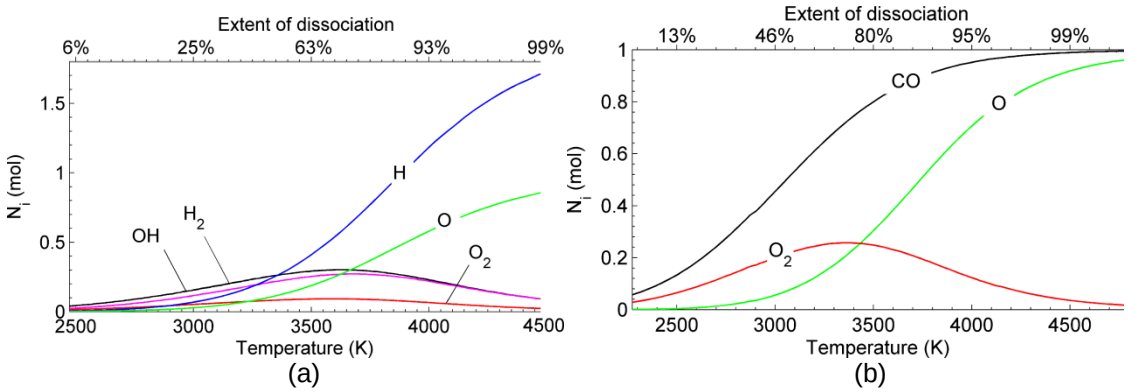

Figure 1.2 The composition at chemical equilibrium for thermal dissociation of 1 mol of (a) H_2O and (b) CO_2 at 1 bar.

performance grim. Lower operating temperatures and a means of avoiding the need to separate H_2, CO, and O_2 are desired.

Both of these goals can be met by splitting H_2O and CO_2 in a series of endothermic and exothermic chemical reactions comprising a thermochemical cycle. In thermochemical cycles, endothermic reactions that proceed at temperatures less than 3000 K are combined with exothermic reactions that ultimately achieve the desired H_2O- or CO_2-splitting. As a result, the operating temperature of the splitting process is lowered, and O_2, H_2, and CO are intrinsically separated. All intermediate chemicals in the series of reactions are recycled so that the net effect is the splitting of H_2O or CO_2 using only process heat derived from the sun.

Hundreds of thermochemical cycles have been proposed dating back to the 1960's when thermochemical cycles were explored as a means of storing waste heat from nuclear reactors [12, 13]. Nuclear waste heat is delivered at a maximum temperature of 1300 K, and this temperature limitation constrained the nuclear cycles to three or more, often complex, chemical reactions. Thermodynamic analyses [14-20] and reviews [21-28] have shown that the work required to separate chemicals in many steps increase irreversibility and limit cycle efficiency. Concentrated solar thermal energy offers the potential to reach

temperatures in excess of 1300 K, opening the door for two-step H_2O- and CO_2-splitting thermochemical cycles with less irreversibility and potentially higher efficiency.

Recent solar thermochemical research has focused on two-step metal oxide redox cycles [29]. In metal oxide cycles, a metal oxide, MO_x, is first reduced at high temperature (up to 2500 K) using concentrated solar energy to supply the required process heat:

$$MO_x \rightarrow MO_{x-y} + \frac{y}{2} O_2 \tag{1.1}$$

In equation (1.1), MO_x represents the metal oxide and MO_{x-y} represents its reduced, or oxygen-deficient, state. The reduced metal oxide is reoxidized at a lower temperature by H_2O or CO_2 to generate H_2 or CO:

$$MO_{x-y} + yH_2O \rightarrow MO_x + yH_2 \tag{1.2}$$

$$MO_{x-y} + yCO_2 \rightarrow MO_x + yCO \tag{1.3}$$

Reactions (1.2) and (1.3) could also be run in parallel to produce H_2 and CO (syngas) concurrently.

Many MO_x/MO_{x-y} pairs have been proposed in the literature, and the most promising are reviewed in Refs. [24, 26, 27, 29]. Candidate MO_x/MO_{x-y} pairs are provided in Table 1.1, which also lists the temperature at which the metal oxide can be reduced, the molecular weight of the metal oxide, and the theoretical gravimetric yield of fuel when the MO_x/MO_{x-y} pair is implemented in the thermochemical cycle. The MO_x/MO_{x-y} pairs can be classified into two categories. In the first category, the metal oxide is completely reduced to a new phase in the MO_{x-y} state. In the second category, the metal oxide is partially reduced such that the phase of the metal oxide is retained, and $y < x$. The extent

Table 1.1 Candidate MO_x/MO_{x-y} pairs for the two-step solar thermochemical cycle, including the temperature at which the metal oxide can be reduced, the molecular weight of MO_x, and the theoretical gravimetric yield of fuel (relative to MO_x).

	Redox Pair MO_x/MO_{x-y}	T_r *(K)*	M_{MO_x} *(g mol^{-1})*	*Fuel Yield (mmol g^{-1})*
Complete Reduction	MgO/Mg	3710	40.3	24.8
	CaO/Ca	4290	56.1	17.8
	ZnO/Zn	2330	81.4	12.3
	GeO_2/GeO	2050	104.6	9.6
	CdO/Cd	1830	128.4	7.8
	SnO_2/SnO	2600	150.7	6.6
Partial Reduction	$CeO_2/CeO_{2-\delta}$	1300–1800	172.1	0.12[a]
	$FeO_{1.33}/FeO_{1.33-\delta}$	1000–2000	231.5	0.3[b]

[a] corresponds to $\delta = 0.02$ at $T_r = 1800$ K and $p_{O_2} = 10^{-2}$ atm

[b] maximum yield experimentally demonstrated at $T_r = 1500$ K and $p_{O_2} \sim 10^{-6}$ atm in Ref. [34]

of the partial reduction is quantified by the non-stoichiometry, δ, of the metal oxide, which indicates the moles of oxygen removed from the metal oxide per mole of the metal oxide. The two categories of metal oxides in the two-step thermochemical cycle balance the factors that influence solar fuel production, including the temperature required to reduce the metal oxide, the gravimetric yield of fuel, and the separation of products, differently.

The complete reduction of the metal oxide in the two-step thermochemical cycle favors high gravimetric fuel yields at the expense of high reduction temperatures and the need to separate gas products. Table 1.1 shows that the metal oxides that are completely reduced produce more fuel than their partial reduction counterparts, ranging from 6.6 mmol/g for SnO_2 to 24.8 mmol/g for MgO. The complete reduction of these metal oxides, however, also requires temperatures above 1800 K. Optical systems can concentrate sunlight by

3000–5000 times[3] and achieve temperatures greater than 2000 K, but are limited to temperatures less than 2500 K because of reradiation losses. This limitation precludes the lowest-molecular weight, highest-gravimetric-fuel-yield metal oxides, such as MgO, from solar thermal reduction (Table 1.1). It is possible to reduce MgO if an electrothermal [30] or carbothermal [31] reduction is used, but both of these hybrid reductions require a work input (electrical or chemical, respectively). Zinc oxide can be reduced using concentrated solar process heat as the exclusive energy input at 2000–2200 K, and also has a favorable theoretical yield of fuel, 12.3 mmol/g, greater than any metal oxide that can be reduced at temperatures below 2500 K. Consequently, it has been identified as highly promising, and receives considerable attention in the literature (see Ref. [29] and the references cited therein).

A challenge associated with the ZnO/Zn pair, and other metal oxides that completely reduce, is their volatility. When reduced, ZnO sublimates into Zn(g) and O_2(g), and the gas products must be separated while preventing their recombination. Efforts to date have focused on a rapid quench. For quench rates of 10^5 K/s and when the Zn(g)-O_2 products are diluted prior to the quench up to 500 times by hot Ar, over 90% of the Zn is recovered as Zn(s) [32]. In a 10 kW_{th} prototype reactor, 60% of the Zn was recovered [33]. Zn(g) and O_2 separation is achieved intrinsically in hybrid reduction processes that either liberate Zn(g) and O_2 physically separated in space (electrothermal reduction) [30] or liberate Zn(g) in an O_2-free environment (carbothermal reduction) [31].

The extreme volatility of the metal oxides that completely reduce is one of the reasons why research is on-going into less volatile, heavier metal oxides that can be partially reduced, such as CeO_2 (ceria) and iron-based oxides. When a metal oxide is partially

[3] Parabolic dish mirrors typically concentrate the sun by a factor of 3000. By adding a secondary parabolic concentrator at the aperture of the receiver, concentrations of 5000 times are possible, and in highly advanced systems, 10,000 suns. Solar optics are reviewed in Refs. [147, 148].

reduced, a small portion of the oxygen atoms are unbound from the crystalline lattice, as quantified by the non-stoichiometry parameter, δ, which gives the moles of oxygen unbound per mole of the metal oxide. A key consequence of the partial reduction is that the metal oxide remains solid, which significantly eases the separation of the O_2 and H_2/CO gas products. In addition, partial reduction proceeds at lower temperatures than those for complete reduction (Table 1.1) if a sweeping gas or vacuum is used to maintain a low oxygen partial pressure atmosphere. Ceria is a promising candidate for solar thermochemical fuel production via partial reduction. Its melting point (2800 K) is 800 K higher than the 1000–2000 K operating temperatures anticipated in the solar thermochemical cycle, rendering it less susceptible to volatilization than the iron-based oxides or ferrites, whose melting points are closer to 2000 K [26, 34, 35]. Ceria is capable of undergoing changes in non-stoichiometry without a significant reorganization of its lattice. At T = 1500 K, ceria retains a cubic fluorite phase when reduced to δ = 0.10 [35]. Solid-state phase changes are common during the thermal reduction of iron-based oxides, and can cause significant loss of reactivity [26]. Furthermore, ceria features a high selectivity to H_2 and CO, producing the gases in the optimum 2:1 H_2:CO ratio for liquid hydrocarbon synthesis [36].

The tradeoff when using ceria, or other non-stoichiometric oxides, for thermochemical fuel production is a drop in the theoretical yield of fuel. Ceria reduced to δ = 0.02 at 1800 K in a $p_{O_2} = 10^{-2}$ atm environment, a condition identified as desirable for solar fuel production [37], produces 0.12 mmol g^{-1} of fuel when oxidized by H_2O or CO_2, 100 times lower than the 12.3 mmol g^{-1} produced in the complete reduction and oxidation of ZnO/Zn. The lower fuel yield in partial reduction based metal oxide thermochemical cycle presents a challenge to its implementation. More metal oxide is required to produce a given amount of fuel, which increases the solar energy input. Furthermore, a large fraction of the input goes towards heating the metal oxide to the requisite reduction temperature,

and is not stored in the H_2 and CO products. Recuperation of this sensible energy is the key to achieving practical solar-to-fuel efficiency [37, 38]. Thus, there are challenges to both the complete reduction and partial reduction versions of the metal oxide thermochemical cycle, and further research is required to realize implementation of either approach.

In addition to those outlined above, a major technical challenge preventing the implementation of the ZnO/Zn solar thermochemical cycle is the kinetically constrained oxidation of Zn(ℓ,s). As Zn(ℓ,s) oxidizes, a layer of the ZnO product grows at the reaction interface, separating the Zn and H_2O/CO_2 reactants, and forcing the reaction to proceed through solid-state diffusion [39, 40]. In an attempt to overcome the diffusion barrier, oxidation at the nano- to microscales has been studied, in both fixed bed [41-48] and aerosol reactor [49-56] configurations. Studies have shown that the oxidation of particles above 100 nm remains diffusion limited. Zinc particles in a 30 mol% H_2O atmosphere at 633 K with a mean diameter of 160 nm require 1.5 h to convert to 80% ZnO [42, 44]. Zinc particles larger than 100 nm oxidized by CO_2 or CO_2/H_2O mixtures also exhibit solid-state diffusion limitations, as shown in Chapter 2, where data from fixed bed reactor systems are comprehensively reviewed.

For monodisperse aerosols of Zn particles with mobility sizes between 50 and 100 nm, complete conversion of zinc was achieved with steam at 448 K in 10 s [57]. However, this experiment was completed at a low aerosol concentration since the monodisperse aerosol was obtained by size selecting particles from a polydisperse aerosol using a differential mobility analyzer (DMA). In experiments with larger concentrations of polydisperse aerosols, agglomeration of the nanoparticles prevents the favorable kinetics observed at low aerosol concentrations [50, 54, 55]. The conversion of zinc was limited to 20% with residence times on the order of seconds, but at the expense of continuous recovery of ZnO for regeneration to Zn [54-56]. Recent work at the University of

Minnesota improved the recovery of the aerosol, achieving particle yields of 96%, but failed to increase conversions [58].

In the present study, the oxidation of Zn(g) is presented as a promising alternative to the oxidation of solid or liquid zinc. This approach circumvents diffusion in the solid ZnO. Interestingly, the homogeneous oxidation of Zn(g) is a thermodynamically unfavorable reaction pathway. It has been shown both theoretically and experimentally that ZnO(g) is not present to an important extent in mixtures of Zn(g) and an oxidizer (O_2, H_2O, or CO_2). The heterogeneous oxidation of Zn(g) is more favorable than the homogeneous oxidation such that Zn(g) and H_2O or CO_2 react on a surface to form ZnO and H_2 or CO. Referring to Zn(g) oxidation as heterogeneous emphasizes the favorability of this reaction pathway, but note that the oxidation of Zn(ℓ,s) is also heterogeneous. Further details on this point are provided in Chapter 2.

The promise of the heterogeneous oxidation of Zn(g) has been inadvertently observed in Zn aerosol reactors [51, 53]. When reactor temperatures were maintained above the Zn saturation temperature, up to 90% of the Zn was converted to ZnO with reaction times on the order of seconds [53]. Prior studies of the heterogeneous oxidation of Zn(g) in tube flow reactors also point to the promise of achieving rapid oxidation rates [59-68]. The rate of the heterogeneous oxidation of Zn(g) by H_2O and CO_2 is between 1×10^{-10} and 5×10^{-7} mol cm^{-2} s^{-1} for temperatures between 700 and 1200 K, and in reacting mixtures composed of more than 10% by H_2 and CO. These reaction conditions reflect those in Zn smelting furnaces, which was the process under study in the prior work. Thus, while the data are promising, further investigation is needed to understand the behavior of the heterogeneous oxidation of Zn(g) for conditions that more closely reflect those to be used for H_2 and CO production in the two-step ZnO/Zn solar thermochemical cycle.

The objectives of the present study are to measure the rate of the heterogeneous oxidation of Zn(g), to demonstrate rapid and complete conversion of zinc, to develop

kinetic models of the reaction suitable for reactor design, and to quantify the benefit that can be realized if heterogeneous Zn(g) oxidation is implemented in the two-step thermochemical cycle. Towards the first two objectives, a reactor is constructed in which the rate of Zn(g) oxidation is measured gravimetrically for temperatures between 800 and 1150 K, Zn(g) concentrations up to 36 mol%, and H_2O/CO_2 concentrations up to 45 mol%. The reactor allows for independent control of the molar flows of Zn(g) and H_2O/CO_2 at the inlet and these flows can be set such that the ratio of H_2O/CO_2 to Zn(g) is between one and 200, ensuring that zinc is the limiting reactant.

To address the third objective of extracting kinetic expressions from the measured oxidation rates, a numerical model of the tube flow reactor is developed to account for the coupling between gas phase mass transfer and intrinsic surface kinetics that is inherent in all heterogeneous reaction systems. In the prior studies of the heterogeneous oxidation of Zn(g), mass transfer is neglected. The researchers justified this assumption using "back-of-the-envelope" calculations of the characteristic mass transfer rates. For temperatures between 800 K and 1200 K, and with mass transfer length scales between 2.5 mm and 23 mm (the radius of the tubes in which Zn(g) was oxidized), mass transfer rates were generally estimated to be 2 or more times faster than the measured surface reaction rate [61, 64, 69]. To safely neglect mass transfer, its characteristic rates should be orders of magnitude faster than the intrinsic rate of the surface reaction [70, 71]. The data in the present study, conducted over similar temperatures and with a shorter length scale for mass transfer of 1.95 mm, show that mass transfer in the Zn(g) oxidation system is not negligible. Thus, a model is developed to properly interpret reaction rate data. A finite-volume based numerical approach is taken to capture the fluid flow, mass transfer, and surface chemistry present in the Zn(g) oxidation tube flow reactor. Regression of the model to the measured reaction rate data allows intrinsic kinetic parameters to be quantified.

A parametric thermodynamic analysis of the ZnO/Zn thermochemical cycle is completed to show that the kinetic benefit associated with the heterogeneous oxidation of Zn(g) outweighs the penalty of adding the latent energy of vaporization. Material, energy, and entropy flows are balanced over all processes in the cycle to calculate the required solar energy input and the fraction of that input stored chemically in the H_2 and CO, i.e., the solar-to-fuel efficiency. The conversion of zinc in the fuel production step of the cycle is treated parametrically to show the effect of incomplete zinc conversion on the efficiency of H_2 and CO production. The analysis shows that if a complete conversion of zinc is achieved via the heterogeneous oxidation of Zn(g), the penalty of generating zinc vapor is offset.

Recently, a 2 kW_{th} prototype scale solar thermochemical reactor based on the partial reduction and oxidation of ceria was constructed and tested in the solar simulator at the ETH in Zurich, Switzerland [72, 73]. The reactor featured porous (80% as fabricated), monolithic ceria [72] and commercially available ceria felt [73] in a fixed bed configuration, producing H_2, CO, and syngas via thermochemical cycling of the ceria materials between ~1800 K in a 10^{-5} atm oxygen partial pressure atmosphere and ~900 K, the temperature at which H_2O and/or CO_2 were split. The reactor demonstrated, for the first time, that ceria can serve as a substrate for thermochemical fuel production on a scale larger than that employed in laboratory, bench-top experiments. The prototype reactor cycled ~300 g of ceria, while bench-top reactors typically cycle ~1 g of ceria. While the demonstration of fuel production is promising, the solar-to-fuel efficiency of the reactor was low (0.4%) in part because of the lack of heat recuperation between the high and low temperature reduction and oxidation steps, but also because of the slow rate of ceria reduction [16]. Given that ceria reduction and oxidation are gas-solid reactions, increasing the specific surface area of the ceria promises to increase production rates and, ultimately, the solar-to-fuel efficiency.

Specific surface area may be increased by introducing porosity and nano- or micro-scale features into the solid [74, 75]. The objective of the present study is to characterize the impact of ceria morphology on the rate of reduction and oxidation. To do so, the rates of oxidation of porous and limited porosity ceria materials are compared. Two reactors are constructed. In the first, the ceria materials are chemically and isothermally cycled at 1100 K, with reduction using H_2. At this temperature, the adverse effects of sintering are mitigated, and the probability of retaining the porous ceria architectures is increased, permitting them to be differentiated. In the second reactor, the ceria materials are thermochemically cycled between ~1500 K and ~1200 K where the effects of sintering are more pronounced. Oxidation is with CO_2.

The dissertation is organized into two parts. The study of the heterogeneous oxidation of Zn(g) is presented in Part I. The oxidation of solid, liquid, and gaseous zinc is first reviewed in Chapter 2. The experimental study of the kinetics of the heterogeneous oxidation of Zn(g) by H_2O and CO_2 is presented in Chapter 3. The quartz tube flow reactor and experimental methodology are described, and the numerical model for fluid flow, mass transfer, and surface chemistry is developed. The model is applied to determine reaction rate expressions for Zn(g) oxidation by H_2O and CO_2 from the measured heterogeneous reaction rates. The rate data are interpreted within the framework of the obtained reaction rate expressions. The results show that the heterogeneous oxidation of Zn(g) is indeed an intriguing pathway for H_2 and CO production in the ZnO/Zn cycle that promises to improve zinc conversions and fuel production rates. In Chapter 4, energy and entropy balances of the ZnO/Zn cycle are completed to show that the high zinc conversions possible via the heterogeneous oxidation of Zn(g) outweigh the penalty associated with adding the Zn vaporization energy.

The study of the reduction and oxidation of ceria is presented in Part II. The thermochemical cycling of ceria is reviewed in Chapter 5. Its non-stoichiometric

thermodynamics is first presented, as they underpin the partial reduction approach to thermochemical fuel production. The oxidation of ceria is then reviewed, which points to the promise of porous architectures for achieving rapid kinetics. The two experimental campaigns undertaken to study the impact of morphology of the rates of oxidation are presented in Chapter 6. The materials synthesized for testing are described. Experiments were conducted isothermally at 1100 K and dynamically at temperatures between 1000 and 1500 K, featuring chemical and thermochemical cycling, respectively.

Part I:
The Oxidation of Zn(g)

2 The Oxidation of Zinc

In this chapter, the oxidation of zinc as a solid, liquid, and gas is reviewed. First, the thermodynamics and kinetics of the oxidation of Zn(ℓ,s) are presented, highlighting the attempts to overcome the passivating nature of the ZnO layer by oxidizing Zn(ℓ,s) at the nm- to µm-scale. The oxidation of gaseous zinc is then introduced as a promising alternative to the oxidation of Zn(ℓ,s) for the production of H_2 and CO in the Zn/ZnO thermochemical cycle. The thermodynamics governing Zn(g) oxidation are presented and discussed, and the literature available for the oxidation of Zn(g) by H_2O and CO_2 is reviewed. Finally, prior results are summarized and the need for additional research, addressed in the present study, is discussed.

2.1 The Oxidation of Solid and Liquid Zinc

2.1.1 The Thermodynamics of Zn(ℓ,s) Oxidation

The change in enthalpy and the change in Gibbs free energy of the oxidation of solid and liquid zinc by H_2O(g) and CO_2(g) are presented in Figure 2.1 for temperatures between 373 and 800 K and 1 bar. The change in enthalpy during oxidation is given by the difference in the enthalpies of the products and reactants at the specified reaction temperature referenced to the standard 298 K, 1 bar state:

$$\Delta\bar{H}_{\mathrm{r}} = \bar{H}_{\mathrm{products}} - \bar{H}_{\mathrm{reactants}} = \sum_i \left(\nu_i \bar{h}^o_{f,i} + \int_{T^o}^{T_r} \nu_i \bar{c}_{p,i} dT \right) \tag{2.1}$$

Reactants and products are distinguished in equation (2.1) by the stoichiometric coefficient, ν_i, which is positive for products and negative for reactants. The energy of the

chemical bonds is included in the enthalpies of formation, $\bar{h}^o_{f,i}$. The change in the Gibbs free energy of the oxidation is calculated according to

$$\Delta\bar{G}_\mathrm{r} = \Delta\bar{H}_\mathrm{r} - T\Delta\bar{S}_\mathrm{r} \tag{2.2}$$

with the change in entropy of oxidation calculated in an analogous way to the change in enthalpy of oxidation (equation (2.1)). An absolute entropy is defined for reactants and products, $\bar{s}^o_i$, that is zero at 0 K, in accordance with the third law of thermodynamics.

$$\Delta\bar{S}_\mathrm{r} = \bar{S}_\mathrm{products} - \bar{S}_\mathrm{reactants} = \sum_i \left(\nu_i \bar{s}^o_i + \int_{0\ \mathrm{K}}^{T_r} \nu_i \frac{\bar{c}_{p,i}}{T} dT \right) \tag{2.3}$$

Thermodynamic data are taken from the HSC 7.0 database [76].

The oxidation of Zn(ℓ,s) by H_2O and CO_2 is exothermic, releasing 55.6 kJ/mol H_2O and 65.5 kJ/mol CO_2 at 298 K. For comparison, the reduction of ZnO requires 350 kJ/mol of process heat at 298 K, five times the amount released in the oxidation of Zn by H_2O and CO_2. The changes in the enthalpies of the reaction in Figure 2.1 at 693 K are associated with the melting of Zn. The change in Gibbs free energy functions is not subject to a jump at the phase transition due to the relation of the change in enthalpy and entropy:

$$\frac{\Delta\bar{H}_\mathrm{phase}}{T} = \Delta\bar{S}_\mathrm{phase} \tag{2.4}$$

The enthalpy of reaction determines the process heat released or required for a reaction, but it is the Gibbs free energy that governs the reaction equilibrium. At fixed temperature and pressure, systems tend towards a state of minimum Gibbs free energy. When solid or liquid zinc is oxidized by H_2O or CO_2, the Gibbs free energy over the 373 to 800 K temperature range is reduced ($\Delta\bar{G}_\mathrm{r} < 0$), indicating that the oxidation of solid and liquid zinc is thermodynamically favored over these temperatures.

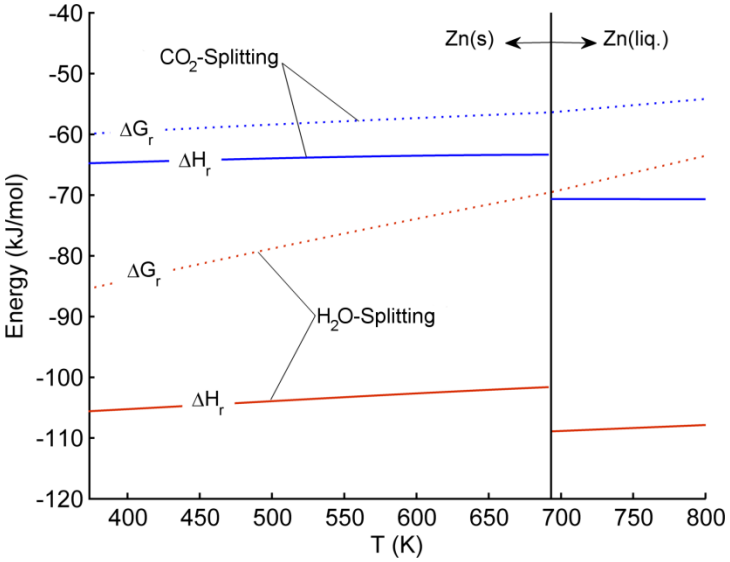

Figure 2.1 The enthalpy of reaction and change in Gibbs free energy for the oxidation of Zn(ℓ,s) by H_2O(g) and CO_2(g)

2.1.2 Zn(ℓ,s) Oxidation Kinetics

While the oxidation of Zn(ℓ,s) is thermodynamically favored, i.e. when at temperatures below 800 K, it is kinetically constrained. The ZnO product forms a passivating layer at the reaction interface that significantly slows the rate of oxidation. It is, in fact, the passivating nature of the ZnO layer that protects galvanized steel from corrosion [77]. Theories for the kinetics of bulk Zn oxidation were developed as early as 1933, and show that the rate of oxidation is controlled by the transport of reacting species via concentration gradients and pressure forces in the zinc oxide layer [78-81].

Many studies document the slow transport of reacting species through ZnO, and hence the slow oxidation rate of bulk Zn [39, 40, 82, 83]. At 323 K in a 95% relative humidity nitrogen atmosphere, 24 hours is required to oxidize 0.02% of the mass of zinc discs that are 10 mm in diameter and 0.5 mm thick, an average oxidation rate of 2×10^{-8} mol cm^{-2} s^{-1} [39]. Water vapor bubbled through liquid zinc held at 700 to 773 K initially oxidizes the

Zn(ℓ) at a rate between 2×10^{-7} mol cm^{-2} s^{-1} and 10×10^{-7} mol cm^{-2} s^{-1}, but the oxidation rate rapidly decreases with the onset of diffusion limitations [82]. The rate of oxidation of Zn particles with mean diameters between 50 µm and 700 µm at temperatures near the zinc melting point is also slowed significantly by the diffusion barrier [83]. Research on the oxidation of solid or liquid Zn for H_2 and CO production in thermochemical processes has thus focused on generating high specific surface areas (reaction surface area per unit volume).

To increase the specific surface area, solid or liquid zinc particles are oxidized at the nano- or micro-scale. Numerous thermogravimetric studies show that, even at these scales, the kinetics of Zn powder oxidation by H_2O [41, 42, 44, 84], CO_2 [43], and H_2O-CO_2 mixtures [45, 46] are diffusion-limited. Ernst *et al.* [44] oxidized powders with a mean particle size of 160 nm and a specific surface area of 5.1 m^2 g^{-1} at temperatures between 603 and 633 K and with H_2O concentrations between 10 and 50 mol%. At 633 K in a 30 mol% H_2O atmosphere, the average oxidation rate over 90 minutes (the time required to reach ~90% conversion) is 5×10^{-11} mol cm^{-2} s^{-1}. After the initial formation of a ZnO layer, which is complete within 30 s, the rate of oxidation is diffusion-limited, and fits a diffusion-limited shrinking core model [71]. Temperature dependence of the effective diffusion coefficient was quantified by an Arrhenius expression with an activation energy of 43 kJ/mol. For similar particle sizes and oxidation conditions, Funke *et al.* [42] report the activation energy to be 132 kJ/mol.

Oxidation of zinc powder by CO_2 and mixtures of H_2O and CO_2 also exhibit diffusion limitations. Loutzenhiser *et al.* [43] oxidized particles with an average diameter of 11.4 µm and a specific surface area of ~4 m^2 g^{-1} at temperatures between 640 and 754 K and for concentrations of CO_2 between 0.5 and 75 mol%. At 673 K in a 0.5% CO_2 atmosphere, the average oxidation rate over four hours (the time required to reach 43% conversion) is 1×10^{-11} mol cm^{-2} s^{-1}, on the same order as that observed in the H_2O system noted above

[44]. Interestingly, over the first minute of oxidation when the ZnO layer is formed, the conversion of zinc decreases from 40% to 25% with increasing CO_2 concentrations from 0.5% to 75%. The authors attribute this unanticipated behavior to the formation of a denser ZnO layer at higher CO_2 concentrations. After the ZnO layer formation, the rate of oxidation is diffusion-limited, and fits a diffusion-limited shrinking core model. The activation energy of the effective diffusion coefficient is 162 kJ/mol. When zinc particles of similar size and specific surface area (~5 m^2 g^{-1}) are oxidized over the same temperature range by mixtures of H_2O and CO_2, the oxidation is again characterized by the formation of a ZnO layer over ~30 s, after which the rate of oxidation is limited by diffusion [46].

Solid and liquid zinc can also be oxidized in an aerosol, which allows the reaction to proceed continuously and potentially circumvents mass and heat transfer limitations at the length scales of the packed bed [85, 86]. At the University of Maryland, monodisperse aerosols of zinc nanoparticles were generated via condensation and then size-selected particles were oxidized in a tube furnace using a tandem differential mobility analyzer (DMA)-aerosol particle mass (APM) analyzer technique [57]. The DMA size selects zinc particles based on their electrical mobility, and the APM measures the mass distribution of the particles before and after oxidation. Zinc nanocrystals with mobility sizes between 50 and 100 nm were completely converted to zinc oxide by clean dry air with reaction times near 2.5 seconds and for temperatures between 673 and 773 K [57]. At 448 K, 70 nm zinc crystals were completely converted by 19 mol% water vapor-argon mixtures with a residence time of 10 seconds [57]. The oxidation by H_2O proceeded through two elementary chemical steps, implying that the oxidation mechanism is different than the mechanism for oxidation at higher temperatures. Zinc was first converted to zinc hydroxide, which was then decomposed to zinc oxide and water vapor. Hydroxide formation was also observed at temperatures below 373K [57]. The kinetics of the reaction of zinc nanocrystals by water vapor were described by an Arrhenius rate expression. The order of the reaction with

respect to water is 0.9±0.1, the pre-exponential factor is 1.8×10^{-3} mol cm^{-2} s^{-1}, and the activation energy is 24 kJ/mol, lower than that reported by the prior thermogravimetric studies. These experiments demonstrate that aerosols of zinc nanoparticles with characteristic sizes less than ~100 nm can achieve favorable kinetics.

Preventing nanoparticle agglomeration in polydisperse aerosols at high concentration, however, has proven challenging in reactors that simultaneously synthesize and oxidize zinc aerosols, and the agglomeration has hindered kinetics [42, 49-56, 87]. Scanning electron micrographs of the product aerosol collected on filters downstream of the reaction zone show that aerosol particles agglomerate into filamentary structures with filament diameters between 50 to 100 nm (Figure 2.2). The overall agglomerated structures are larger with sizes up to 60 µm, and X-ray diffraction analysis has shown that 20%, at most, of the agglomerates are converted to ZnO [54, 87]. Aerosol reactors of this type have residence times on the order of seconds and reaction temperatures up to 700 K. Recent work completed at the University of Minnesota highlights the challenge of oxidizing Zn aerosol by H_2O. In a transverse jet reactor operated at 400–700 K, 70 to 80% of the zinc mass is recovered continuously, and less than 7% of the zinc is converted to ZnO [58].

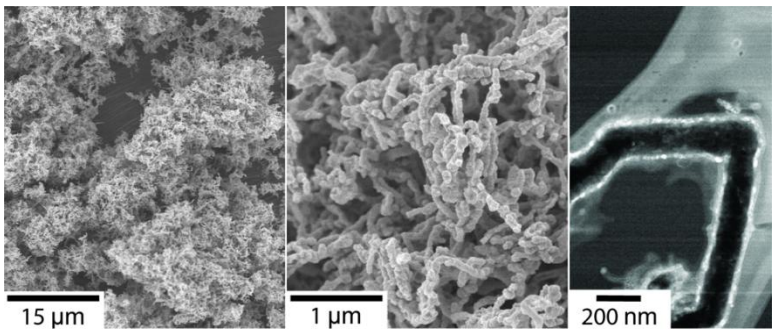

Figure 2.2. (a) SEM images of Zn/ZnO agglomerates, (b) filamentary particles, and (c) a STEM image of a filament. In the STEM image taken using a high-angle annular diffraction field technique, the white corresponds to ZnO and the black to Zn. The images appear in Ref. [54], and are reused with permission.

2.2 The Oxidation of Gaseous Zinc

An intriguing alternative to the oxidation of solid or liquid zinc for the production of H_2 or CO in the Zn/ZnO thermochemical cycle is the oxidation of Zn(g). Oxidizing Zn(g) eliminates the diffusion limitation associated with the ZnO layer, circumventing the requirement of nm-scale reaction surfaces to achieve favorable oxidation kinetics. The thermodynamics and prior studies of the kinetics of Zn(g) oxidation support the promise of this reaction pathway, suggesting that Zn(g) oxidizes faster than Zn(ℓ,s) and, as a result, can be completely converted in short time scales.

2.2.1 Thermodynamics of Zn(g) Oxidation

The oxidation of Zn(g) is heterogeneous, and requires a surface on which to proceed because the homogeneous oxidation of Zn(g) is thermodynamically unfavorable. Palumbo *et al.* [88] developed an expression for the equilibrium constant of the formation of ZnO(g) from Zn(g) and O_2 using data on the Zn-O bond energy [89]. A chemical equilibrium analysis using the derived equilibrium constant shows that in the saturated vapor above ZnO(ℓ,s), the mole fraction of ZnO(g) is at most 5×10^{-5} at 1700 K and 1×10^{-3} at 2400 K. These temperatures are well above those considered in the present study. The low mole fraction of ZnO(g) at equilibrium and the lack of evidence of the formation of ZnO(g) in any kinetic study considering Zn(g) oxidation by O_2 [90-93], H_2O(g) [61], or CO_2 [60, 63-68, 94-96], supports the conclusions that the homogeneous oxidation of Zn(g) does not occur to a significant extent. To oxidize, Zn(g) must first adsorb to a surface on which ZnO can nucleate and grow.

The saturation pressure of zinc, which bounds the maximum concentration of vapor in the reacting gas mixture at any temperature, is shown in Figure 2.3. It increases monotonically with temperature according to the semi-empirical Antoine equation [97].

The saturation pressure is 3 mbar at 800 K and reaches 1000 mbar at 1180 K, the boiling point of Zn at one atmosphere. If operating a reactor at atmospheric pressure, the pressure above that of the partial pressure of Zn(g) must be filled with either excess reactant (H_2O or CO_2) or an inert gas. However, processing excess reactant or large volumes of inert gas is energetically undesirable. Alternatively, one could operate the reactor at a reduced pressure, but a reduced pressure hinders the heterogeneous oxidation of Zn(g) by Le Chatelier's principle. From this perspective, it is advantageous to operate the reactor as close to the normal boiling point of Zn as possible (1180 K), where high Zn(g) concentrations are possible and where inert gas requirements are minimized.

In addition to the saturation pressure of Zn, the chemical equilibrium of the heterogeneous oxidation of Zn(g) reacting system is also important. The change in the Gibbs free energy of the oxidation of Zn(g) by H_2O or CO_2 is shown in Figure 2.4 for a system at 1 bar and for temperatures between 800 and 1200 K. The enthalpy of the reaction is also shown to highlight the fact that the oxidation of Zn(g) is slightly more exothermic than the oxidation of Zn(ℓ,s) (Figure 2.1). The change in the Gibbs free energy

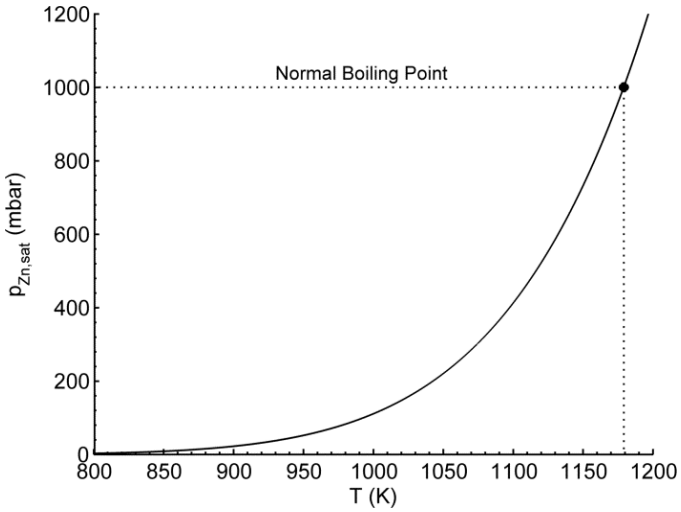

Figure 2.3 The saturation pressure of Zn as given by the Antoine equation [97]

of the oxidation of Zn(g) by H_2O and CO_2 is negative, which indicates that the formation of H_2 or CO and ZnO(s) is favored. The magnitude of the change in the Gibbs free energy, which provides a measure of the propensity of the system to form the desired products, decreases with increasing temperature for Zn(g) oxidation. Consequently, at temperatures above 1200 K, zinc conversion is limited by chemical thermodynamics rather than kinetics.

Gibbs free energy minimization was used to assess the chemical equilibrium [76]. The maximum conversion of Zn(g) that could be achieved at 1 bar for temperatures between 800 and 1180 K if Zn(g) were present in the reacting system at the maximum concentration possible is shown in Figure 2.5(a). The conversion of zinc decreases monotonically with increasing temperature, but conversions greater than 90% are possible up to 1180 K, greater than what has been achieved over the course of hours in the oxidation of Zn(ℓ,s) in fixed beds and aerosols (see section 2.1.2). Furthermore, zinc conversions could be higher if H_2O and CO_2 were initially present in excess of the

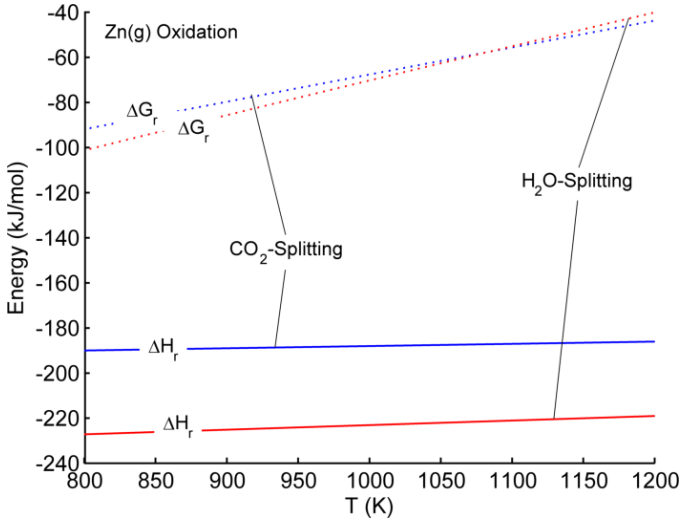

Figure 2.4 The enthalpy of reaction and change in Gibbs free energy for the oxidation of Zn(g) by H_2O(g) and CO_2(g) at 1 bar

stoichiometrically required amount. With H_2O or CO_2 at concentrations double the stoichiometric ratio, conversions above 98% are possible (Figure 2.5(b)). Collectively, Figures 2.3–2.5 show that there is a trade off in the Zn(g) reacting system. High oxidation temperatures increase the maximum concentration of Zn(g) that could be achieved in the reacting volume, but also reduce the thermodynamic potential for attaining high zinc conversions unless excess H_2O or CO_2 is used.

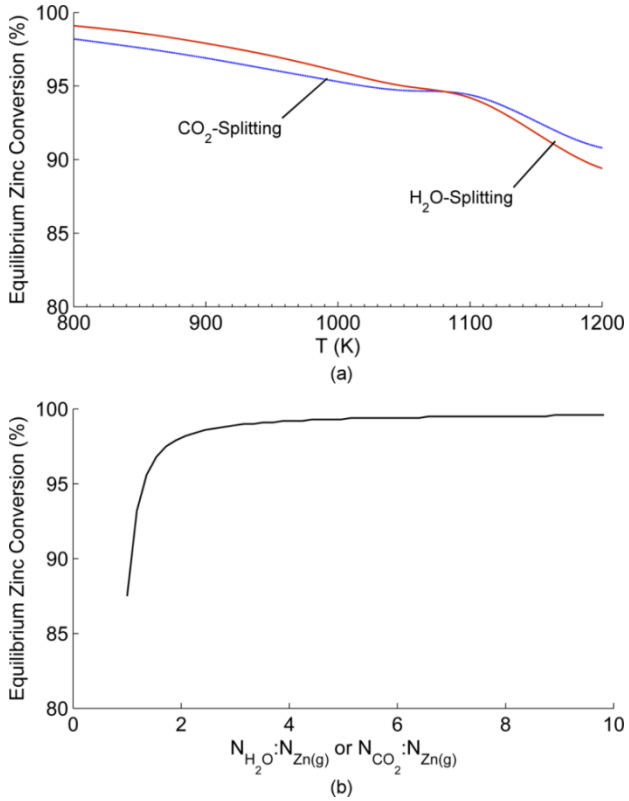

Figure 2.5 (a) The percentage of Zn(g) converted to ZnO(s) at chemical equilibrium with Zn(g) initially present at its saturation pressure and for oxidation with a stoichiometric amount of H_2O and CO_2. (b) The conversion of Zn(g) at equilibrium at 1000 K with excess H_2O or CO_2.

2.2.2 Zn(g) Oxidation Kinetics

The kinetics of the heterogeneous oxidation of Zn(g) by H_2O [61] and CO_2 [60, 63-68, 94-96, 98] have been studied in quartz tube flow reactors. The temperatures and partial pressures of reacting species in the experiments of these prior studies are summarized in Table 2.1 along with the diameter of the reactor tube (if reported). The previous studies considered temperatures between 800 and 1300 K, Zn(g) and H_2O(g) partial pressures between 10^{-5} and 0.3 atm, CO_2 partial pressures between 0 and 0.6 atm, and CO partial pressures between 0 and 0.9 atm.

In all of the prior work, the partial pressures of H_2 and CO (the products of oxidation) are generally greater than the partial pressure of Zn(g). High concentrations of H_2 and CO during Zn(g) oxidation are relevant to pyrometallurgical zinc smelting processes [62], but are not anticipated for thermochemical fuel production. The abundant presence of H_2 and CO reduces the thermodynamic driving force for oxidation, shifting the equilibrium towards the formation of reactants. Figure 2.6 demonstrates the unfavorable

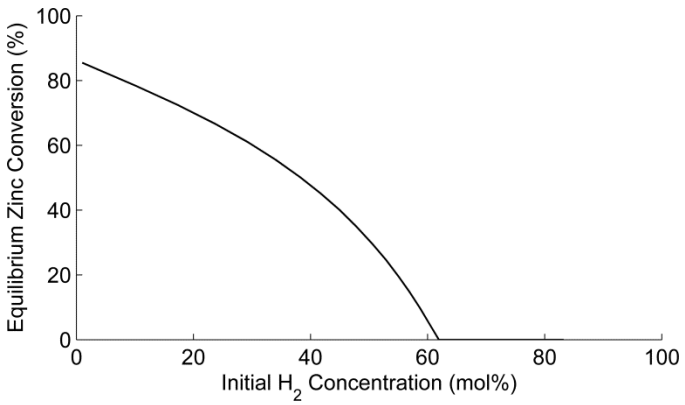

Figure 2.6 The impact of the initial concentration of H_2 on the oxidation of Zn(g) by H_2O(g) at 1000 K and 1 bar. Zn(g) and H_2O(g) are initially at the Zn saturation pressure, and an inert gas is present to ensure that the total pressure is 1 bar.

Table 2.1 Summary of oxidation temperatures, oxidizing gas compositions, and reactor tube diameter for previous studies of Zn(g) oxidation by H_2O and CO_2. The partial pressures of reacting species are reported in atm.

	Clarke and Fray [61]	Fray and colleagues [60, 62, 65, 66, 94]	Leonard, Stansbury [95, 96]	Dell'Amico and See [98]	Lewis and Cameron [63, 64]	Osborne et al. [67]
T (K)	781–1124	973–1273	1013–1273	1023–1273	1073–1273	1000–1173
$p_{Zn(g)}$	6.5×10^{-5}–0.05	0.01–0.17	0.08–0.28	0.01–0.12	0.10–0.20	0.03–0.09
p_{CO_2}		0.01–0.17	0.01–0.39	0.10–0.17	0.0–0.42	0.01–0.58
p_{CO}		0.08–0.90	0.44–0.90	0.11–0.27	0.0–0.53	0.0–0.55
p_{H_2O}	6.5×10^{-5}–0.05					
p_{H_2}	0.02–0.99					
d (mm)	5–10	5–10	not reported	not reported	20	not reported

thermodynamics of Zn(g) oxidation in systems with high H_2 and CO concentrations, using the oxidation of Zn(g) by H_2O(g) in a Zn(g)-H_2O-H_2 mixture at 1000 K as an example. The amount of Zn(g) and H_2O converted into additional H_2 decreases substantially, from 85 to 0%, as the amount of H_2 initially present in the reacting system increases from 1 to 60%. Thus, while the prior work provides insight on the oxidation of Zn(g) by H_2O and CO_2, it must be carefully interpreted for the conditions anticipated in the two-step Zn/ZnO cycle.

Clarke and Fray [61] measured the kinetics of the heterogeneous oxidation of Zn(g) by H_2O. The diameter of the tube in which Zn(g) was oxidized varied between 5 and 10 mm. Zn(g) and H_2O(g) were generated by reducing ZnO with H_2 at temperatures in excess of 1500 K, thereby restricting the relative amounts of Zn(g) and H_2O(g) in the reacting mixture to a stoichiometric ratio (1 H_2O to 1 Zn(g) molecule). For temperatures between782 and 1077 K, Zn(g)/H_2O partial pressures up to 0.05 atm, and H_2 partial pressures between 0.02 and 0.99 atm, the rate of oxidation is between 2×10^{-8} and 6×10^{-7} mol cm^{-2} s^{-1}. The rate of Zn(g) oxidation is on the same order or faster than the rate of Zn(ℓ,s) oxidation prior to the onset of diffusion limitations [44, 82]. The data fit a semi-empirical reaction rate expression,

$$r'' = \left(a + d p_{H_2}^{1/2}\right)\left(p_{Zn(g)} - p_{Zn(g)}^{eq}\right), \tag{2.5}$$

that is first order with respect to zinc. Of note is that the reaction rate increases proportional to the square root of the partial pressure of H_2. The kinetic parameters a and d are provided in Table 2.2. A limitation of expression (2.5) is that it implicitly accounts for the influence of H_2O on kinetics through the equilibrium Zn(g) pressure. The implicit dependence requires that a thermodynamic calculation be made each time that the reaction rate is evaluated.

Table 2.2. The kinetic constants in the semi-empirical reaction rate expression suggested by Clarke and Fray (1979)

T	$a \times 10^5$	$d \times 10^5$
(K)	*(mol cm^{-2} sec^{-1} atm^{-1})*	*(mol cm^{-2} sec^{-1} $atm^{-3/2}$)*
781	3.64	2.91
876	3.13	2.92
921	2.69	2.88
979	2.88	3.93
1023	2.68	5.29
1077	2.67	7.39
1124	4.19	69.16

While there is only a single study, to my knowledge, of the oxidation of Zn(g) by H_2O-H_2 mixtures, there are many studies of the oxidation of Zn(g) by CO_2-CO mixtures [60, 63-68, 94-96, 98]. The consensus in the literature is that the rate of Zn(g) oxidation is on the order of 10^{-9} mol cm^{-2} s^{-1} when the partial pressure of CO initially present in the reacting mixture is greater than ~0.2 atm. When the CO partial pressure is reduced to below ~0.2 atm, the rate of Zn(g) oxidation increases up to two orders of magnitude, and is closer to 10^{-7} mol cm^{-2} s^{-1}. Rapid Zn(g) oxidation is desired in the solar thermochemical Zn/ZnO cycle, and so results for the CO-rich conditions in which Zn(g) oxidation rates are low are not included in the review that follows. For the more relevant results obtained when the initial concentration of CO is less than ~0.2 atm and Zn(g) oxidation rates are more rapid, the literature is unclear regarding the influence of temperature and reacting mixture compositions on the kinetics of Zn(g) oxidation.

Fray and co-workers [60, 65, 66, 68, 94] characterized the kinetics of the reaction of Zn(g) and CO_2-CO mixtures for temperatures between 781 and 1070 K, Zn(g) partial pressures between 0.01 and 0.1 atm, and for stoichiometric feed conditions (1 CO_2 to 1 Zn(g) molecule). When the CO partial pressure is below 0.2 atm, the rate of Zn(g) oxidation by CO_2 is between 2×10^{-8} and 3×10^{-7} mol s^{-1} cm^{-2}, on the same order of, or

faster than, the rate of oxidation of Zn(s) powders *prior* to the onset of diffusion limitations [43]. The data fit a semi-empirical rate expression that is first order with respect to zinc:

$$r'' = k\left(p_{\mathrm{Zn(g)}} - p^{\mathrm{eq}}_{\mathrm{Zn(g)}}\right) \tag{2.6}$$

Temperature dependence of the rate parameter, k, is captured in an Arrhenius expression with an activation energy of 46 kJ/mol and a pre-exponential factor of 9.075×10^{-4} mol cm^{-2} s^{-1} atm^{-2}. Similar to the limitation of expression (2.5), expression (2.6) accounts implicitly for the influence of CO_2 on kinetics through the equilibrium Zn(g) partial pressure. This limitation likely contributes to the poor agreement with data obtained in different experiments [63, 98], where errors between the measured and predicted rates of oxidation up to 75% are reported. A more explicit dependence on CO_2 is anticipated and desired.

Lewis and Cameron [63, 64, 69] characterized the Zn(g) oxidation kinetics for larger Zn(g) partial pressures between 0.1 and 0.2 atm. Gaseous zinc was generated by evaporating zinc in an inert gas flow so that non-stoichiometric amounts of Zn(g) and CO_2 were obtained at the reactor inlet. For temperatures between 1073 and 1273 K and for CO_2 partial pressures between 0.05 and 0.25 atm, the rate of oxidation is between 4×10^{-8} and 5×10^{-7} mol cm^{-2} s^{-1}, on the same order as the rates measured by Fray and coworkers [60, 94]. The data fit a reversible, second-order rate equation that is first order with respect to both Zn(g) and CO_2:

$$r'' = k\left(p_{\mathrm{Zn(g)}}p_{\mathrm{CO_2}} - \frac{p_{\mathrm{CO}}}{K_{\mathrm{eq}}}\right) \tag{2.7}$$

Temperature dependence of the reaction rate is captured in the equilibrium constant, K_{eq}, and in the kinetic parameter, k. For the kinetic parameter, the Arrhenius expression

activation energy is 166 kJ/mol and the pre-exponential factor is 16.1 mol cm^{-2} s^{-1} atm^{-2}. The reported activation energy is three times the value reported by Clarke and Fray [60] for similar temperatures.

Osborne et al. [67] developed a phenomenological rate expression based on a postulated sequence of elementary chemical steps that can be applied over the temperature range from 1003 to 1273 K. However, the reaction rate data reported are not normalized by the reaction surface area, and the surface area is not reported, rendering interpretation of the results or the rate expression impossible.

The results of Leonard [95] and Stansbury [96] starkly contrast the literature with regard to the oxidation of Zn(g) by CO_2-CO mixtures. For all temperatures and oxidizing gas compositions considered, oxidation is reported to be zeroth-order, following the equations:

$$\log r'' = -\frac{2.9 \times 10^3}{T} - 1.6 \quad 1038\ \text{K} < T \leq 1156\ \text{K} \tag{2.8}$$

$$\log r'' = -\frac{1.8 \times 10^3}{T} - 2.8 \quad 1156\ \text{K} < T \leq 1273\ \text{K} \tag{2.9}$$

The kinetic expressions developed in the literature for the oxidation of Zn(g) by CO_2 are compared in Figure 2.7 at 1100 K. The expressions are plotted only for the range of the partial pressure of Zn(g) in the experiments from which the expressions were developed. Depending on the reaction rate expression, the rate of Zn(g) oxidation at 1100 K varies by up to four orders of magnitude. While any number of factors could account for the differences in the kinetic expressions, the variability might be a result of the different sizes of reaction tubes implemented in the previous studies, which varied between 5 mm [60] and 20 mm [63]. The reaction tube diameter impacts the rate of mass transfer during oxidation. There is more resistance to mass transfer the larger the diameter

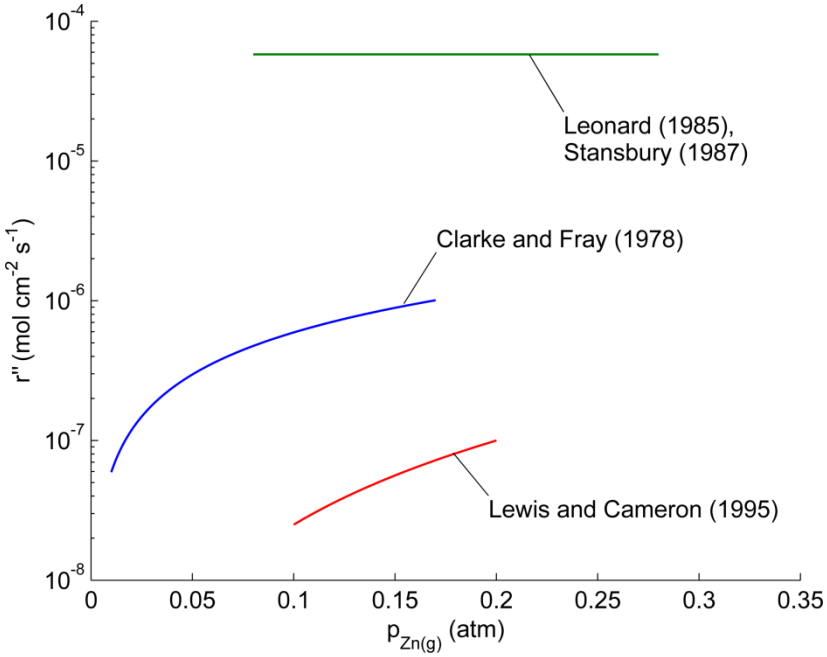

Figure 2.7 Comparison of reaction rates predicted for the heterogeneous oxidation of Zn(g) by CO2 from the kinetic expression developed by Lewis and Cameron [64]**, Clarke and Fray** [60]**, and Leonard/Stansbury** [95, 96]

of the tube. The measured rate of oxidation are likely underreported since mass transfer limitations were present. The data in Figure 2.7 support this hypothesis. The rate of oxidation predicted by the reaction rate expression developed from experiments conducted in a 20 mm i.d. tube (equation (2.7)) is lower than the oxidation rate predicted by the reaction rate expression developed from experiments conducted in a 5 mm i.d. tube (equation (2.6)). The data for the oxidation of Zn(g) by O_2, a related system, also support this hypothesis. In similarly sized reactor tubes, mass transfer limits the rate of Zn(g) oxidation by O_2 [93].

2.3 Summary and Discussion

The oxidation of Zn(ℓ,s) by H_2O and CO_2 for particle sizes above 100 nm and for temperatures below 800 K is limited by diffusion through the ZnO layer that forms at the

reaction interface, and the oxidation kinetics follow the diffusion-limited shrinking core model [43-45]. As a result of the diffusion limitation, minutes are required to convert up to ~80% of the zinc, with exact times dependent on the size of the Zn(ℓ,s) particle [84]. Average oxidation rates over the time required to convert 50% or more of the zinc are on the order of 10^{-11} mol cm^{-2} s^{-1} (section 2.1.2). Also, continuous oxidation of Zn(ℓ,s) as an aerosol is hindered by particle agglomeration, and the maximum zinc conversion that has been achieved is ~20% with a residence time on the order of seconds [54]. Oxidizing Zn(ℓ,s) thus presents a challenge for H_2 and CO production in the two-step Zn/ZnO thermochemical cycle.

The heterogeneous oxidation of Zn(g) is a promising alternative to Zn(ℓ,s) oxidation, and the kinetic studies in the literature point to this promise. For temperatures between 700 and 1200 K, the rate of oxidation is between 10^{-8} and 10^{-7} mol cm^{-2} s^{-1}, even when the reacting system contains high concentrations of H_2 and CO that were shown to thermodynamically hinder Zn(g) oxidation (Figure 2.6). Unlike Zn(ℓ,s) oxidation, the heterogeneous oxidation of Zn(g) is not limited by the solid-state diffusion of reacting species through the ZnO product. As a result, rapid and complete conversion of zinc is a tantalizing possibility.

While the prior kinetic studies point to the promise of the heterogeneous oxidation of Zn(g) by H_2O and CO_2 for the production of H_2 and CO, there are a number of shortcomings. First, data for Zn(g) oxidation conditions relevant to H_2 and CO production in the Zn/ZnO solar thermochemical cycle are, for the most part, unavailable because oxidizing gas compositions in the prior studies reflect those of zinc smelting processes [62]. Second, the rate of the heterogeneous oxidation of Zn(g) by CO_2 predicted by the available reaction rate expressions vary by as much as 4 orders of magnitude (Figure 2.7). The variability of the data in the CO_2 system raises concern about the data from the one study available on the oxidation of Zn(g) by H_2O. Finally, comparing data from the Zn(g)-CO_2

oxidation studies reveals that the transport of Zn(g) and CO_2 in the gas phase may have influenced the rate of Zn(g) oxidation, as the measured rate of oxidation correlates with the diameter of the tube in which the Zn(g) is oxidized. The experimental study presented in Chapter 3 addresses these issues.

3 The Kinetics of the Heterogeneous Oxidation of Zn(g) by CO_2 and H_2O

The heterogeneous oxidation of Zn(g) is a promising means of producing H_2 and CO from H_2O and CO_2 in the two-step Zn/ZnO solar thermochemical cycle. Oxidizing Zn(g) eliminates the kinetic limitation imposed by the passivating ZnO layer that forms on the surface of Zn(ℓ,s), and the prior data, as reviewed in Chapter 2, suggest that the rate of oxidation could be increased by an order of magnitude when oxidizing Zn(g) compared to Zn(ℓ,s). With the onset of diffusion limitations at temperatures of 650 to 750 K, the rate of Zn(ℓ,s) oxidation by H_2O and CO_2 decreases from $\sim 5 \times 10^{-8}$ mol cm^{-2} s^{-1}, with the exact rate dependent on particle size, to a rate undetectable by thermogravimetric analyzers [43, 44, 46, 84]. The rate of Zn(g) oxidation by H_2O and CO_2 is on the order of 10^{-7} mol cm^{-2} s^{-1} for temperatures between 800 and 1200 K when the reacting mixture initially contains H_2 and CO at concentrations above the concentration of Zn(g), H_2O, and CO_2, a condition that likely inhibits kinetics [60, 61, 63]. In this chapter, the experimental investigation of the heterogeneous oxidation of Zn(g) at atmospheric pressure and for temperatures between 800 and 1150 K, Zn(g) concentrations up to 36 mol%, and H_2O/CO_2 concentrations up to 45 mol%, is presented. Mass transfer in the heterogeneous reaction system is accounted for in a numerical model that decouples the intrinsic surface kinetics from the global reaction rates. The results demonstrate the rapid rate of the heterogeneous oxidation of Zn(g) for conditions anticipated in the Zn/ZnO solar thermochemical cycle, and kinetic expressions suitable for future reactor design and scale up are developed.

3.1 Experimental Methodology

As discussed in Chapter 2, prior studies of Zn(g) oxidation completed in tube flow reactors neglect the impact of gas phase mass transfer on kinetics. The reported rates of oxidation, however, depend on the diameter of the reactor tube, suggesting that mass transfer may have slowed the oxidation to an extent that the surface kinetics are underreported. To achieve a more accurate measurement of the Zn(g) oxidation rates at the reaction surface, a reactor is designed and an experimental approach developed to separate surface kinetics from mass transfer. For the design, a stagnant film model was used to estimate the rate of mass transfer as a function of the reactor tube diameter. Predictions for mass transfer were compared to the Zn(g) oxidation rates reported in the prior studies. For temperatures between 900 and 1150 K, the predicted rate of mass transfer was 2 to 10 times faster in a 4 mm diameter reactor tube than the reported Zn(g) oxidation rates (reviewed in Chapter 2). The small flow passage, smaller than those used in previous work, was thus selected to minimize the effects of mass transfer. Preliminary results showed that, despite the design effort, mass transfer still significantly influenced the measured rate of Zn(g) oxidation. A numerical model was therefore developed to account for the effect of mass transfer.

The tube flow reactor developed allows for the accurate control of the primary oxidation parameters: the oxidation temperature and the concentrations of the Zn(g), H_2O(g), and CO_2 reactants. An electric tube furnace controls the oxidation temperature to within $\pm$10 K, mass flow controllers deliver gases to the reactor with an accuracy of $\pm$1% of the desired flow rate, and a custom designed LabVIEW program ensures that all testing equipment operates harmoniously. Reaction conditions are chosen with the goal of achieving rapid production of H_2 and CO, and to reflect conditions anticipated in the

Zn/ZnO thermochemical cycle. The rates of fuel production are measured by analyzing the composition of the product gas flow.

3.1.1 The Tube Flow Reactor

The isothermal tube flow reactor, comprised of concentric quartz tubes, is depicted in Figure 3.1. The outermost tube has an outer diameter (o.d.) of 25 mm, an inner diameter (i.d.) of 23 mm, and is sealed at its ends with stainless steel flanges. A pool of liquid zinc (99.999% pure, metals basis) rests at the bottom of the outer tube to serve as the source of Zn(g) in the reactor. A capillary tube with a 3 mm o.d. and a 1 mm i.d. delivers gas containing H_2O(g) or CO_2 to the reactor. The CO_2 and H_2O(g) flows are controlled with mass flow controllers[4], except in H_2O-splitting experiments at $T \leq 900$ K when H_2O(g) is delivered to the reactor by saturating a flow of Ar with distilled and degassed $H_2O(\ell)$. The tip of the capillary tube protrudes into a third tube, referred to as the oxidation tube, which has an o.d. of 6 mm and an i.d. of 3.9 mm. It is in the oxidation tube that reactants mix and Zn(g) heterogeneously oxidizes. Insulating tube mounts hold the reactor in an electric furnace (Thermolyne 79500), and the furnace maintains the reactor temperature between 800 and 1150 K.

During an experiment, Ar (grade 5.0 purity) enters the annulus between the outer tube and the inner tube through the flanges at the end of the reactor. The Ar saturates with Zn(g) via evaporation of the liquid pool, forming a gas mixture of Zn(g) and Ar. The Zn(g)-Ar mixture flows from left to right into the gap between the capillary tube and the oxidation tube. After passing through the gap, the Zn(g)-Ar flow mixes with the oxidizing gas flow from the capillary tube and reacts on all available surfaces, depositing ZnO on the surface and releasing H_2 or CO into the flow. Where the Zn(g)-Ar mixture and oxidizing

[4] The details of the flow controllers, including their accuracy, are provided in Appendix A. All gas flows are metered with mass flow controllers in the present study.

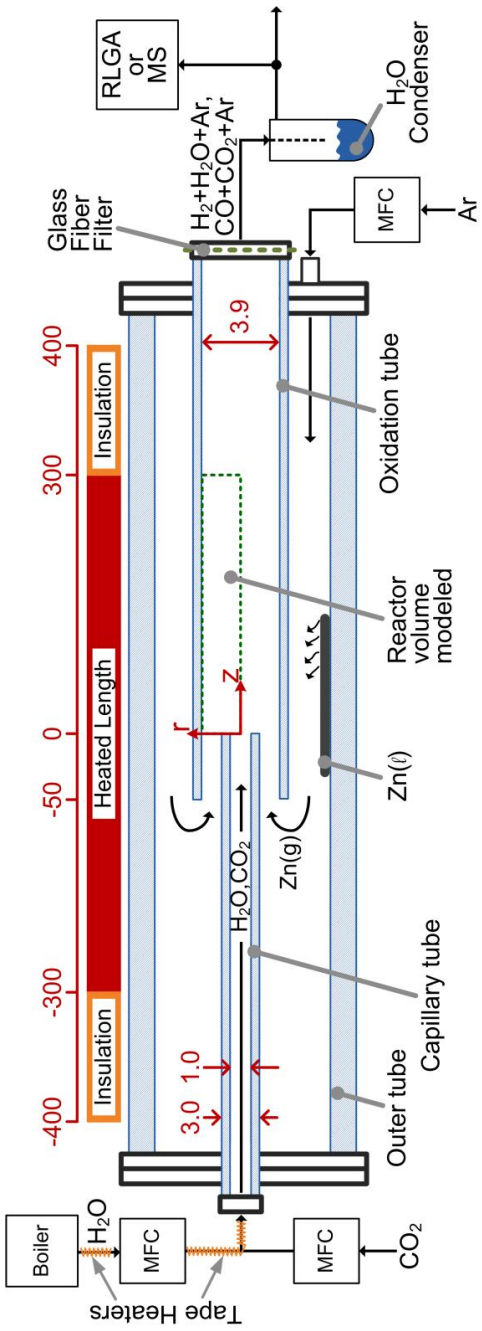

Figure 3.1 The quartz tube flow reactor (not to scale). Dimensions are in mm.

gas mixture come into contact with one another is considered the reactor inlet (labeled z = 0 in Figure 3.1). Reaction proceeds over an isothermal length of 300 mm. Upon exiting the heated zone of the reactor, the temperature of the product gas drops rapidly and unreacted Zn(g) condenses on the cooler surfaces of the oxidation tube. Prior to chemical analysis, the product gas passes through a glass fiber filter to remove any remaining Zn(g), and, when H_2O is present, a condenser to remove unreacted and condensable H_2O. The composition of the product gas is measured with a mass spectrometer (Inficon Transpector CPM, abbreviated MS) during H_2O-splitting or a Raman Laser Gas Analyzer (Atmosphere Recovery Inc. 129a, abbreviated RLGA) during CO_2-splitting to ascertain the total rate of H_2 and CO production. The MS could not be used to measure CO because of fragmentation errors, further explained in Appendix A. The MS and RLGA are calibrated using known mixtures of a solute (H_2, CO, CO_2) diluted with Ar. The accuracy of the MS is 2% of the reading, and the accuracy of the RLGA is ±0.2 mol% of the solute. The calibration and accuracy of these instruments are discussed further in Appendix A.

The temperature along the axis of the oxidation tube in the reactor is measured in an experiment with identical total gas flow conditions to the oxidation experiments using a chromel–alumel (type K) thermocouple with an exposed 1.6 mm diameter junction. The gas flow rate has no impact on the measured temperature for the range of flow rates considered in the present experiments. The axial temperature normalized by the furnace set point temperature is shown in Figure 3.2 for set point temperatures of 900 and 1200 K. Isothermal reaction conditions are maintained within ±10 K for a 300 mm length extending from the inlet of the reactor inlet to a position just upstream of the insulating tube mounts. The shape of the temperature distribution is similar for all furnace set points.

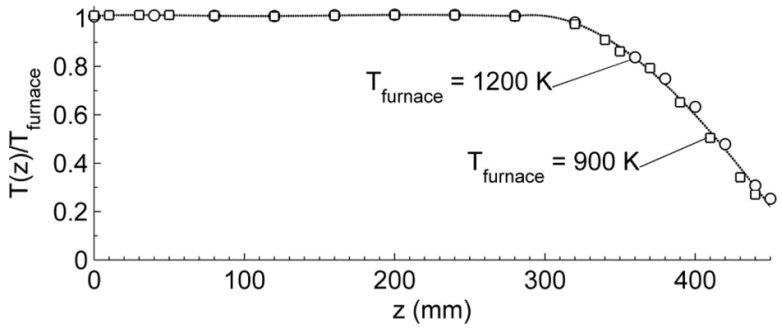

Figure 3.2 The reactor centerline temperature along the axis of the oxidation tube normalized by the electric furnace set point, $T_{furnace}$. Isothermal conditions exist over the first 300 mm of the oxidation tube.

3.1.2 Experimental Procedure

At the start of each experiment, the quartz tubes are washed with soap and water and outer tube, the capillary tube, the oxidation tube, the glass fiber filter, and the Zn are measured. The reactor is assembled, sealed, and purged. The furnace is then raised to and held at a temperature of 523 K while purging the reactor with Ar. This temperature is high enough to desorb any residual H_2O on the tube surfaces, but below the melting point of zinc (690 K) to prevent premature evaporation. After holding the reactor at 523 K, the purge flow to the reactor is turned off and the furnace set-point is raised to the desired oxidation temperature (800–1150 K depending on the experiment). As the gas volume in the reactor heats, gas is displaced from the reactor. The displacement rate is monitored with a bubble flow meter. The reactor system is considered fully heated when the rate of gas displacement is less than 5 mL min^{-1} (the total reactor volume is 300 mL). Flows to the reactor are then turned on to initiate heterogeneous Zn(g) oxidation. Oxidation proceedes until a steady rate of fuel production is achieved and is maintained for 4-90 mintues depending on the oxidation temperature. These durations ensure that measurable amounts of ZnO are deposited on the oxidation tube surfaces. Oxidation is terminated by turning

off the oxidizing gas flow and the furnace. When oxidation has ceased, all flows to the reactor are stopped, and the reactor is allowed to cool to room temperature.

After an experiment, the masses of the outer tube, the capillary tube, the oxidation tube, the glass fiber filter, and any remaining Zn(s) are measured, and the Zn species mass balance is conducted. In all experiments, the evaporated Zn mass is accounted for within 5%. The mass of ZnO deposited on the surface of the oxidation tube is measured by removing the ZnO in small sections with hydrochloric acid. A small length of the oxidation tube is dipped in the acid so that the ZnO deposited there dissolves. The tube is then removed from the acid, the hydrochloric acid evaporated, and the tube re-weighed. The difference in the mass of the tube before and after the removal of the ZnO is taken as the mass of ZnO deposited in that section. This process is repeated until all of the ZnO is removed from the tube. Elemental Zn is not co-deposited with ZnO. Hydrogen is not produced during ZnO removal and analysis of the hydrochloric acid solution after ZnO removal using atomic absorption spectroscopy indicates that the amount of Zn present balances with the mass of ZnO removed.

3.1.3 Data Analysis

The heterogeneous reaction rate is calculated from

$$r''(z) = \frac{m_{\mathrm{ZnO}}(z)}{M_{\mathrm{ZnO}}(\pi d \Delta z) t_{\mathrm{d}}} \tag{3.1}$$

where d is the inner diameter of the oxidation tube (3.9 mm), Δz is the length of the section over which the ZnO mass, m_{ZnO}, is removed, and t_{d} is the time over which H_2 and CO is produced in the experiment. An implicit assumption in equation (3.1) is that the reaction is steady over t_{d}. Figure 3.3 shows the rate of H_2 and CO production at the reactor outlet during an experiment for temperatures between 800 and 1150 K. Data for CO production is shown in Figure 3.3(a), and data for H_2 production is shown in

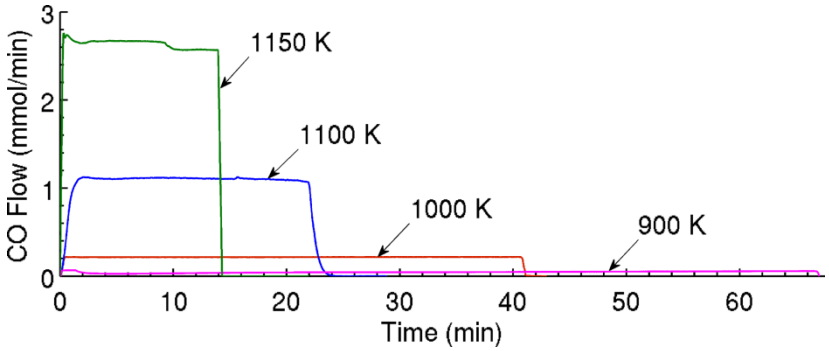

(a)

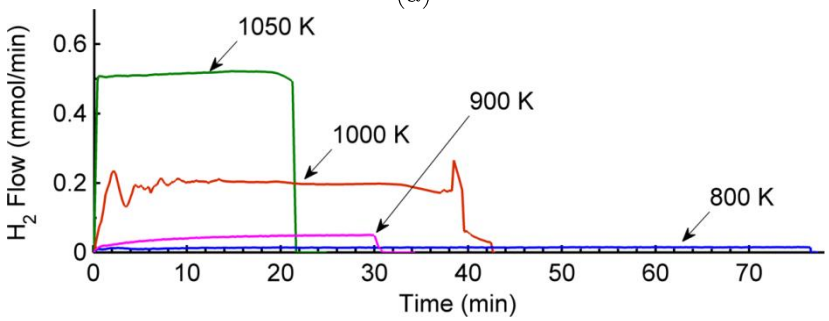

(b)

Figure 3.3 (a) The rate of CO production for temperatures from 900 to 1150 K, and (b) the rate of H_2 production for temperatures from 800 to 1100 K.

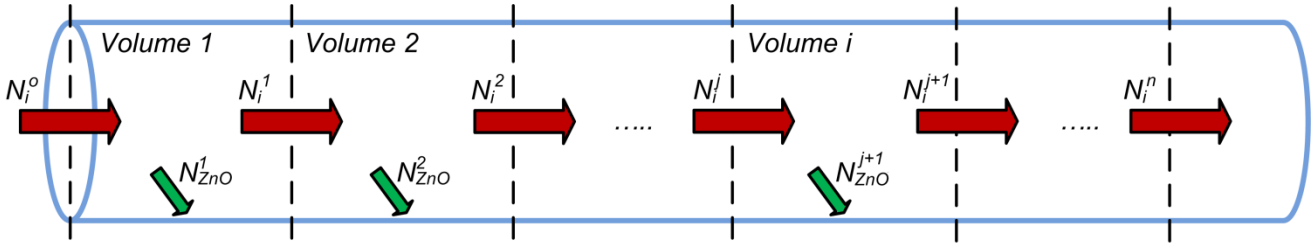

Figure 3.4 Schematic showing the technique to calculate the average composition of reacting gases. The oxidation tube is divided into discrete control volumes and a mass balance is applied to each volume to determine the species flow in and out. The schematic is drawn for the H_2O system, but it is trivially extended to the CO_2 system.

Figure 3.3(b). In all experiments, steady fuel production is achieved within ~2 min, and the steady-state is sustained for the duration of the experiment.

Using the heterogeneous reaction rate and the known inlet molar flow rates of reacting gas species, mass balances are constructed to quantify the average composition of the reacting species along the tube axis. This technique is described pictorially in Figure 3.4. First, the mixing cup concentration of gases at the reactor inlet is calculated by integrating the known species flow rates over the duration of the experiment:

$$N_{\mathrm{i}}^{o} = \int_{0}^{t_{\mathrm{d}}} \dot{n}_{\mathrm{i}}^{o}\, dt \tag{3.2}$$

In the case of Zn, the inlet molar flow rate is calculated from:

$$\dot{n}_{\mathrm{Zn}}^{o} = \frac{m_{\mathrm{Zn}}^{o}}{M_{\mathrm{Zn}} t_{\mathrm{d}}} \tag{3.3}$$

which assumes that the flow of zinc that enters the oxidation tube during the experiment is steady. Oxidation of zinc on the tube walls removes Zn(g) and H_2O or CO_2 from the gas stream while adding H_2 or CO. If N_{ZnO}^{1} is the number of moles of ZnO deposited in the first section of the tube, then the number of moles of the gaseous species i leaving the first section is

$$N_{\mathrm{i}}^{1} = N_{\mathrm{i}}^{o} + \nu_{\mathrm{i}} N_{\mathrm{ZnO}}^{1} \tag{3.4}$$

The number of moles of species i in the first section of the tube is taken to be the average of the moles entering and exiting the section.

$$N_{\mathrm{i,avg}}^{1} = \frac{N_{\mathrm{i}}^{o} + N_{\mathrm{i}}^{1}}{2} \tag{3.5}$$

Finally, the partial pressure of species i in the first section is calculated based on the average number of moles present and the total pressure in the reactor, P, which is

approximately atmospheric pressure due to the low pressure drop required to drive the low flow rates.

$$p_{\mathrm{i}}^{1} = \left(\frac{N_{\mathrm{i,avg}}^{1}}{\sum N_{\mathrm{i,avg}}^{1} + N_{\mathrm{inert}}} \right) P \tag{3.6}$$

The number of moles of the inert gas present is included, and is the same across all sections since the inert gas does not participate in the reaction. This procedure, written out for the first section, is repeated for each section of the tube to yield the mixing cup axial concentration profiles of the reaction species in the experiment.

The mean residence time of the reacting flow is based on the average velocity of the flow over the isothermal length of the oxidation tube:

$$\bar{t} = \frac{\pi d^2}{4} \int_0^{300\ \mathrm{mm}} \frac{\bar{\rho}_{\mathrm{m}}}{\dot{m}_{\mathrm{m}}} dz \tag{3.7}$$

The mass flow rate of gases along the oxidation tube, $\dot{m}_{\mathrm{m}}$, and the average gas mixture density, $\bar{\rho}_{\mathrm{m}}$, are known from the mass balances outlined above (Figure 3.4). The total percentage of Zn(g) that is heterogeneously oxidized in the tube flow reactor is defined as:

$$X_{\mathrm{Zn}} = \frac{M_{\mathrm{Zn}}}{M_{\mathrm{ZnO}}} \frac{\int_0^{300\ \mathrm{mm}} m_{\mathrm{ZnO}}\, dz}{m_{\mathrm{Zn}}^{o}} \tag{3.8}$$

Process and systematic uncertainties were propagated to the measured surface reaction rate and overall zinc conversion using the sequential perturbation method. The details of the uncertainty analysis are provided in Appendix A.

3.2 Numerical Model for Mass Transfer and Surface Chemistry

A steady-state, two-dimensional model of the tube flow reactor decouples the combined effects of mass transfer and surface kinetics from the measured reaction rates, and allows a kinetic expression to be extracted from the data. The governing equations of the model

express the conservation of mass, momentum, and species in the reactor. The reactor is assumed to be isothermal and axisymmetric. The computational domain is shown in Figure 3.5. It spans the length of the oxidation tube over which Zn(g) and $H_2O(g)/CO_2$ mix, and extends from the center of the oxidation tube to its inner surface in the radial direction. The left plane of the computational domain coincides with the tip of the capillary tube at the reactor inlet ($z = 0$). The governing equations are solved using the finite-volume based SIMPLE algorithm modified for use on a collocated grid, and the second-order accurate power law is used to upwind the convection-diffusion discretization [99, 100]. The code to implement the numerical method is written in FORTRAN.

Conservation of mass is given by

$$\frac{1}{r}\frac{\partial}{\partial r}(r\rho_{\mathrm{m}}v_{\mathrm{r}}) + \frac{\partial}{\partial z}(\rho_{\mathrm{m}}u) = 0 \tag{3.9}$$

where the density is that of the mixture of reacting and inert species (Zn(g), CO_2, CO, and Ar or Zn(g), H_2O, H_2, and Ar). It is assumed that the mixture of gases behaves ideally so

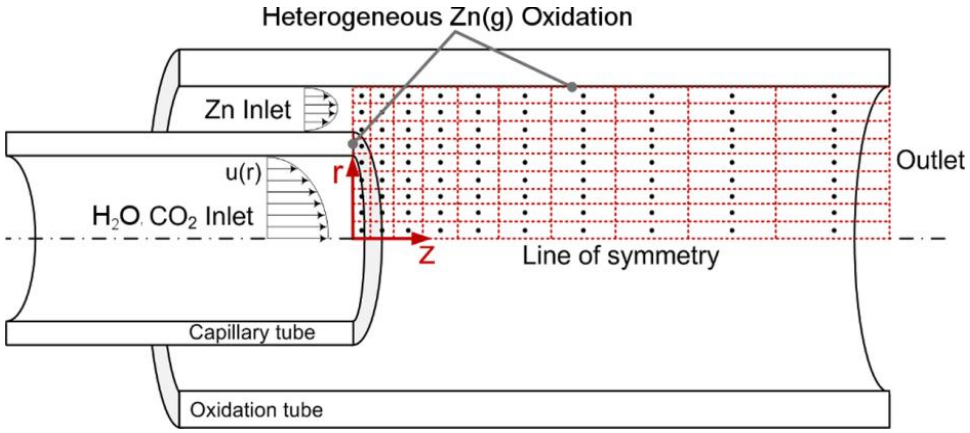

Figure 3.5 The numerical domain and computational grid (shown coarse for clarity) utilized in the mass transfer model of the heterogeneous oxidation of Zn(g) tube flow reactor. The sketch is not to scale.

that the density can be calculated using the ideal gas equation of state.

$$\rho_m = \frac{P\left(\sum_{\mathrm{i}} \frac{\omega_{\mathrm{i}}}{M_{\mathrm{i}}}\right)^{-1}}{R_u T} \tag{3.10}$$

The mixture density varies primarily due to changes in composition (ω_{i}). The temperature is constant and, due to the low mass flow rates in the reactor, the pressure gradients are low.

The differential equations for the conservation of momentum are

$$\begin{aligned} &\frac{1}{r}\frac{\partial}{\partial r}(r\rho_{\mathrm{m}} v_{\mathrm{r}}^2) + \frac{\partial}{\partial z}(\rho_{\mathrm{m}} u v_r) \\ &= \frac{1}{r}\frac{\partial}{\partial r}\left(r\mu\left(2\frac{\partial v_r}{\partial r} - \frac{2}{3}\nabla\cdot\vec{\boldsymbol{u}}\right)\right) + \frac{\partial}{\partial z}\left(\mu\left(\frac{\partial u}{\partial r} + \frac{\partial v_r}{\partial z}\right)\right) - \frac{\partial P}{\partial r} \\ &- \frac{1}{r}\left(\mu\left(\frac{2v_r}{r} - \frac{2}{3}\nabla\cdot\vec{\boldsymbol{u}}\right)\right) \end{aligned} \tag{3.11}$$

in the radial direction, and

$$\begin{aligned} &\frac{1}{r}\frac{\partial}{\partial r}(r\rho_{\mathrm{m}} v_r u) + \frac{\partial}{\partial z}(\rho_{\mathrm{m}} u^2) \\ &= \frac{1}{r}\frac{\partial}{\partial r}\left(r\mu\left(\frac{\partial u}{\partial r} + \frac{\partial v_r}{\partial z}\right)\right) + \frac{\partial}{\partial z}\left(\mu\left(2\frac{\partial u}{\partial z} - \frac{2}{3}\nabla\cdot\vec{\boldsymbol{u}}\right)\right) - \frac{\partial P}{\partial z} \end{aligned} \tag{3.12}$$

in the axial direction, respectively, accounting for spatial changes in density and viscosity due to changes in composition. The viscosity of the reacting flow is calculated using a mass-average of the pure species viscosities,

$$\mu = \sum_{\mathrm{i}=1}^{\mathrm{N}} \omega_{\mathrm{i}}\mu_{\mathrm{i}}\,, \tag{3.13}$$

and the viscosities of the pure species are evaluated using tabulated data [101]. Because the density, velocity, and viscosity of the tube flow change as a result of the heterogeneous oxidation of Zn(g), the Reynolds number is calculated using the average composition and total mass flow rate at the inlet:

$$\mathrm{Re} = \frac{4\dot{m}_{\mathrm{m}}^{o}}{\pi\mu d} \tag{3.14}$$

The Reynolds number is <2300 (see Table 3.1 and Table 3.2), and thus the assumption of laminar flow is justified.

The transport of species mass is given by

$$\frac{1}{r}\frac{\partial}{\partial r}\left(r\rho_{\mathrm{m}}v_{\mathrm{r}}\omega_{\mathrm{i}} + r\mathrm{J}_{\mathrm{i,r}}\right) + \frac{\partial}{\partial z}\left(\rho_{\mathrm{m}}u\omega_{\mathrm{i}} + \mathrm{J}_{\mathrm{i,z}}\right) = 0 \tag{3.15}$$

where $\mathrm{J}_{\mathrm{i,r}}$ and $\mathrm{J}_{\mathrm{i,z}}$ are the diffusive species fluxes in the radial and axial directions. Equation (3.15) is solved for Zn(g), H_2O(g)/CO_2, and H_2/CO, and the concentration of the inert Ar is calculated by applying mass conservation, $\sum \omega_{\mathrm{i}}$=1, throughout the numerical domain. This approach enforces the necessary condition that there is net transport of mass by advection only, i.e., $\sum \mathrm{J}_{\mathrm{i}}$=0 in both the axial and radial directions.

The diffusion of species is modeled using a Fickian constitutive relationship:

$$\mathrm{J}_{\mathrm{i},n} = -\rho_{\mathrm{m}} D_{\mathrm{i,eff}} \frac{\partial \omega_i}{\partial n} \tag{3.16}$$

where $n = r$ for diffusion in the radial direction and $n = z$ for diffusion in the axial direction. The effective diffusion coefficients for the reacting species are calculated using a mixing law [102].

$$D_{\mathrm{i,eff}} = \frac{1 - y_{\mathrm{i}}}{\sum_{\mathrm{j=1,i\neq j}}^{\mathrm{N}} \frac{D_{\mathrm{ij}}}{y_{\mathrm{j}}}} \tag{3.17}$$

The binary diffusivities of the reacting species are estimated according to the Chapman-Enskog theory in the absence of experimental data. The collision cross-section and collision integrals of Zn(g) are estimated using the method described in Ref. [103].

Fickian diffusion is strictly valid only for binary mixtures. Diffusion in mixtures of more than two species is governed by the Stefan-Maxwell equation. The solution of the Stefan-Maxwell equation, however, requires the inversion of a full matrix at each face of

every control volume in the numerical domain, which is computationally expensive. It is thus common practice to approximate multicomponent diffusion with the Fickian form using the effective diffusion coefficient defined by equation (3.17). The approximation is excellent for dilute mixtures where all but one species is present at low concentrations ($\omega_i \ll 1$ for all i except N, for which $\omega_N \approx 1$) [102]. This condition is valid for the present experiments completed at T $\lesssim$ 900 K where the reacting mixture is mostly Ar (see Table 3.1 and Table 3.2). At higher temperatures, Zn(g), H_2O(g)/CO_2, and H_2/CO are all present at appreciable concentrations and the Fickian assumption less accurately predicts the multicomponent diffusion. Errors of 15% are possible, particularly in the H_2O-splitting system that contains H_2 [104].

In the radial direction, symmetry boundary conditions are applied at the centerline of the oxidation tube,

$$\frac{\partial \omega_i}{\partial r}(0,z) = 0, \quad \frac{\partial u}{\partial r}(0,z) = 0, \; v(0,z) = 0, \tag{3.18}$$

At $r = R$, Zn(g) is oxidized. The rate of Zn(g) oxidation is a function of the prevailing composition, $r'' = f\big(\omega_i(R,z)\big)$, with the functional form given by the kinetic expression. For the species transport equations, the net rate of addition or removal of a species by the combined effects of advection and diffusion must balance the surface reaction rate:

$$\omega_i(R,z)\dot{m}''_{\text{deposition}} + J_i(R,z) = \nu_i M_i r''. \tag{3.19}$$

$\dot{m}''_{\text{deposition}}$ is the deposited mass flux, and is known from the surface reaction rate.

$$\dot{m}''_{\text{deposition}} = \sum_i \nu_i M_i r'' \tag{3.20}$$

For the continuity and momentum equations, the deposition of mass at the wall is analogous to suction in a boundary layer flow. The suction velocity is calculated as

$$v_{\mathrm{n,wall}} = \frac{\dot{m}''_{\mathrm{deposition}}}{\rho_{\mathrm{m}}} \tag{3.21}$$

where the subscript 'n' on the velocity denotes the direction normal to the wall. The tangential velocity at the wall is zero, consistent with the no-slip condition.

Between $r = r_c$ and $r = r_b$ at the reactor inlet, the tip of the capillary tube is modeled. Zn(g) can oxidize on this surface, and boundary conditions analogous to (3.19)–(3.21) are applied. The Zn(g)-Ar mixture enters the numerical domain adjacent to the oxidation tube inner surface. The velocity profile is assumed to be fully-developed, and the Zn(g) and Ar concentrations are uniform.

$$\begin{gathered} u(r,0) = \frac{-F}{4\mu}\left(R^2 - r^2 + \left(R^2 - r_b^2\right)\frac{\ln(R/r)}{\ln(r_b/R)}\right), \\ \omega_{\mathrm{Zn(g)}}(r,0) = \omega^o_{\mathrm{Zn(g)}}, \qquad \omega_{\mathrm{Ar}}(r,0) = 1 - \omega^o_{\mathrm{Zn(g)}}, \\ r_{\mathrm{b}} \le r < R \end{gathered} \tag{3.22}$$

The fully-developed velocity profile is for flow in an annulus. The 5 mm annulus length upstream of the reactor inlet is ~10 times longer than the estimated developing length. Furthermore, assuming a uniform velocity at the inlet, rather than a fully-developed one, does not significantly impact the results. The term F is described in Appendix B. The remaining velocity and species concentration variables are zero at the inlets. At the center of the oxidation tube, the CO_2 flow from the capillary tube enters the reactor. Similar to the Zn inlet, the velocity profile is fully developed. The gas is pure CO_2.

$$u(r,0) = 2\left(\frac{\dot{m}_{\mathrm{CO_2}}}{\rho_{\mathrm{CO_2}}\pi r_c^2}\right)\left[1 - \left(\frac{r}{r_b}\right)^2\right], \qquad \omega_{\mathrm{CO_2}}(r,0) = 1, \qquad 0 \le r < r_{\mathrm{c}} \tag{3.23}$$

The fully-developed velocity profile is for flow in a circular duct.

The numerical grid is stretched along the axial coordinate to pack computational cells near the inlet where reaction rates are high, the flow is developing, and steeper gradients are anticipated. By comparing the converged velocity and species fields on successively finer grids, it was determined that 3200 computational cells arranged in an 80 × 40 array

is sufficient for achieving numerical accuracy better than experimental accuracy. Additional grid refinement was found to change the predicted Zn(g) oxidation rates along the tube axis less than the uncertainty in the measured oxidation rates.

To extract kinetic parameters from the experimental data, regression of the numerically predicted and measured Zn(g) oxidation rates is achieved by adjusting the value of the kinetic parameters to minimize a root-sum-squared error objective function.

$$g_{\text{fit}} = \sqrt{\sum_{\mathrm{k}} \left(r''_{\mathrm{k}} - r''_{\mathrm{model,k}} \right)^2} \tag{3.24}$$

where the index k indicates summation over all axial locations of the experimental data. Minimization of the objective function is achieved using the program GenOpt [105]. A hybrid algorithm is implemented that combines particle swarm optimization (PSO) with the Hooke-Jeeves optimization to search for the global minimum in the objective function. The sole requirement placed on the kinetic expressions is that they include dependence on both the Zn(g) and CO_2 or H_2O(g) concentrations. This requirement is both intuitive and important for correctly resolving the kinetics in experiments where both the oxidizing agent and Zn(g) may be the limiting reactant locally in the reactor, despite one or the other being present in excess globally (discussed further in section 3.3). The simplest kinetic expression, i.e. the one with fewest parameters that adequately describe the data is selected.

3.3 Results and Discussion

In this section, the kinetic expressions obtained via optimization of the mass transfer model are presented and discussed. With the kinetic expressions in hand, the advantage of the heterogeneous oxidation of Zn(g) for H_2 and CO production is demonstrated. First, to provide the necessary context for the discussion of kinetics, the experimental conditions of the present study are presented in detail.

The experiments completed are listed in Table 3.1 for the CO_2 system and Table 3.2 for the H_2O system. The tables include the oxidation temperature, the CO_2, H_2O, and Ar gas flow rates (reported at 298 K and 1 bar), the inlet Zn(g) and H_2O(g)/CO_2(g) concentrations, the reaction stoichiometry, the mean gas residence time in the reactor, and the overall percentage of zinc heterogeneously oxidized. In the CO_2 system, pure CO_2 was delivered to the reactor so that $\omega^o_{CO_2} = 100$ wt% in all experiments, while in the H_2O system, mixtures of H_2O and Ar were delivered to the reactor so that the concentration of H_2O(g) at the inlet ranges from 1.3 to 100 wt%. In both reaction systems, the concentration of Zn(g) at the inlet varies dramatically, from 0.3 to 68.6 wt% in the CO_2 system and from 0.4 to 59.6 wt% in the H_2O system. The large variation is due to the exponentional increase of the zinc saturation pressure with temperature (see Chapter 2 for information about the Zn saturation pressure).

The total volumetric flow rates of Ar range from 50 to 300 mL/min in both the CO_2 and H_2O systems. In the case of the H_2O system, the Ar flow is distributed between the Zn and H_2O inlets. The reaction stoichiometries vary between unity and 200 for CO_2-slitting, and between 1.2 and 8 for H_2O-splitting, ensuring that Zn(g) is always the limiting reactant globally. The Reynolds number of the reacting flows range from 10–100. It is anticipated that any turbulence quickly dissipates near the inlet as a fully-developed laminar velocity profile develops. The developing length is between 5 and 50 mm (the

Table 3.1 Experimental parameters in the study of the heterogeneous oxidation of Zn(g) by CO_2, including the inlet Zn(g) and CO_2 concentrations, the gas flow rates, the mean gas residence time, and the overall conversion of zinc.

Experiment	T_{ox} (K)	Q_{Ar} (mL/min)	Q_{CO_2} (mL/min)	Ψ	Re	ω^o_{Zn} (wt%)	$\omega^o_{CO_2}$ (wt%)	$\bar{t}$ (s)	X_{Zn} (%)
1	800	68.3	24.4	200	20	0.3	100	0.8	94
2	900	91.4	6.4	3.4	18	3.3	100	1.0	94
3	1000	18.3	34.2	20	12	13.1	100	0.8	98
4	1000	40.7	34.5	7.1	17	16.4	100	0.7	96
5	1100	45.8	37.4	1.5	23	46.6	100	0.6	97
6	1100	45.1	273	9.5	81	51.2	100	0.1	85
7	1150	49.4	67.1	1.0	42	68.6	100	0.4	88

Table 3.2 Experimental parameters in the study of the heterogeneous oxidation of Zn(g) by H_2O, including the inlet Zn(g) and H_2O(g) concentrations, the gas flow rates, the mean gas residence time, and the overall conversion of zinc.

Experiment	T_{ox} (K)	$Q_{Ar,Zn\ Carrier}$ (mL/min)	$Q_{Ar,H_2O\ Carrier}$ (mL/min)	$Q_{H_2O}{}^*$ (mL/min)	Ψ	Re	ω^o_{Zn} (wt%)	$\omega^o_{H_2O}$ (wt%)	$\bar{t}$ (s)	X_{Zn} (%)
1	800	124	25	0.70	2.5	26	0.4	1.3	0.5	100
2	900	52	51	1.4	1.6	17	2.8	1.3	0.7	98
3	900	53	52	1.4	1.9	17	3.0	1.3	0.7	97
4	1000	75	0	30	7.8	15	8.5	100	0.6	98
5	1050	52	32	73	5.0	24	33.3	53.0	0.4	76
6	1100	50	50	50	1.7	27	51.8	33.1	0.3	84
7	1100	50	49	50	1.2	32	61.2	33.5	0.3	81

*Reported assuming H_2O is an ideal gas at 273 K and 1 atm.

length of the isothermal region is 300 mm), as predicted using the numerical fluid flow model.

For the total gas flow rates, reacting compositions, and for temperatures between 800 and 1150 K, the mean residence time of gas in the reactor is less than or equal to one second in both the CO_2 and H_2O systems.

3.3.1 Kinetic Models for the Heterogeneous Oxidation of Zn(g)

All oxidation conditions were simulated and optimized to determine a kinetic expression and associated kinetic parameters. Through the model, the influence of mass transfer on the measured oxidation rates is elucidated.

3.3.1.1 CO_2 System

Figure 3.6 shows the measured and predicted rates of the heterogeneous oxidation of Zn(g) by CO_2 along the axis of the oxidation tube at each set temperature. Oxidation rates are on the order of 10^{-8}–10^{-5} mol cm^{-2} s^{-1} between 800 and 1150 K, and represent at least an order of magnitude increase over the rates previously observed in the interface-controlled regime of the oxidation of Zn(s) particles by CO_2 [43]. The rate of oxidation increases to a maximum between $z = 5$ mm and $z = 20$ mm as the reacting flow develops and Zn(g) and CO_2 mix, and then decreases as Zn(g) and CO_2 are consumed. The best fit between the model and data is obtained using a second-order kinetic expression, with first-order dependence on both the Zn(g) and CO_2:

$$r'' = k_{\text{Zn-CO}_2} p_{\text{Zn(g)}} p_{\text{CO}_2} \tag{3.25}$$

The possibility of non-linear dependence of the reaction on the Zn(g) and CO_2 concentration was explored, but there was not a statistically significant improvement in the fit attainable with the additional degrees of freedom. The simplicity, and in particular

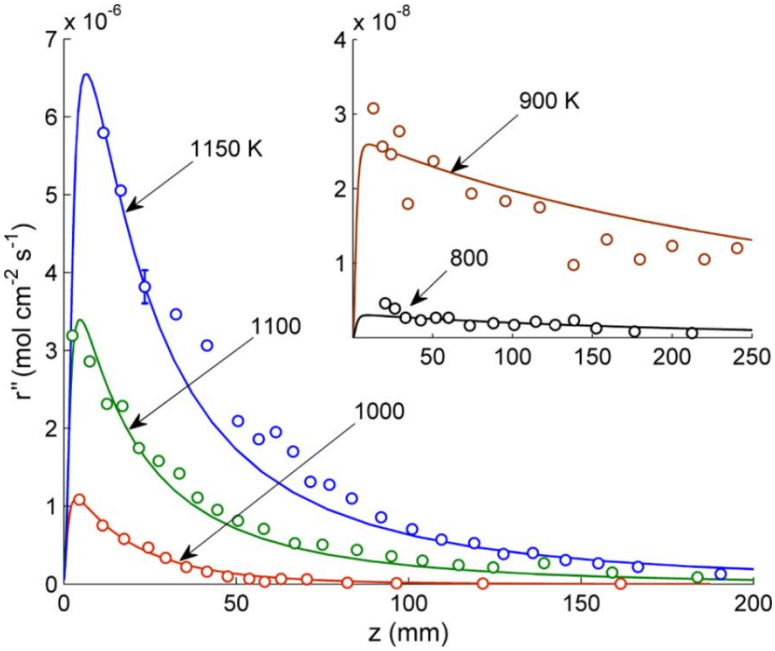

Figure 3.6 The rate of the heterogeneous oxidation of Zn(g) by CO_2 as a function of axial position in the reactor. The points are the experimental data and the lines are the optimized model. Experiment 5 (see Table 3.1) is shown as representative of the rates achieved at 1100 K.

the linearity, of the reaction rate expression should be viewed as an advantage for its intended application in reactor design. Non-linear reaction rate expressions required more tedious analysis, and are often linearized for use in models with analytical solutions [71].

Figure 3.7 is an Arrhenius plot of the rate parameter, $k_{\text{Zn-CO}_2}$, for each experiment reported in Table 3.1. Two experiments were completed at 1100 K with different relative amounts of CO_2 and Zn(g), Ψ=1.5 and Ψ=9.5, as a check on the robustness of the reaction rate expression. The values of the rate parameter, 0.68 and 0.75 mol m^{-2} s^{-1} atm^{-2}, are identical within experimental uncertainty. For comparison, Figure 3.7 includes the rate constants obtained in a prior study which did not consider mass transfer limitations [64]. The activation energy for the heterogeneous oxidation of Zn(g) by CO_2 is 44±3 kJ/mol, in

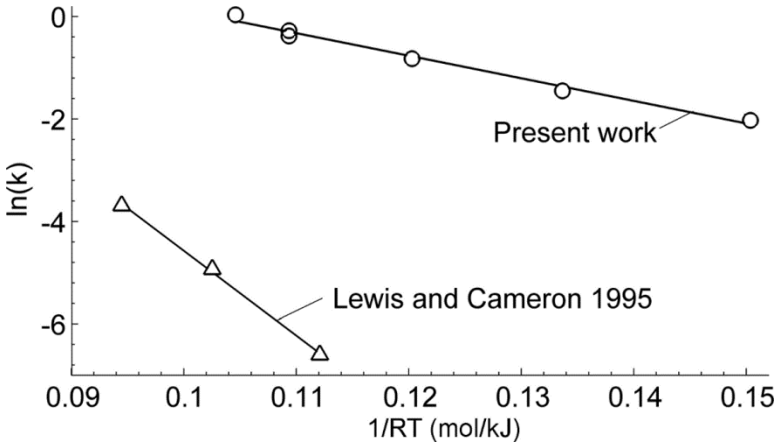

Figure 3.7 Arrhenius plot of the temperature dependent constant determined for rate expression (3.25) via optimization of the mass transfer model for temperatures spanning 800 to 1150 K.

agreement with the values reported in [60, 98], and the pre-exponential factor is 92±6 mol m^{-2} s^{-1} atm^{-2}. The rate constants obtained in the present work are as much as 3.5 times greater than the values reported by [64] for temperatures between 1100 and 1150 K (where the two data sets overlap). The difference is most likely due to the neglect of the radial transport of Zn(g) and CO_2 on the measured rate of heterogeneous oxidation in the prior work. This omission would lead to an under prediction of the rate of the intrinsic surface kinetics.

To highlight the importance of gas phase mass transfer on the rates of oxidation, the rate data were also analyzed neglecting mass transfer; that is, assuming that there are no radial gradients of concentration in the reactor. Under this assumption, the mixing cup Zn(g) and CO_2 partial pressures determined from the mass balances applied along the oxidation tube are compared directly to the rate of Zn(g) oxidation along the reactor axis to determine kinetic information. A result is provided in Figure 3.8 for 1150 K. The reaction rate constant, is 6.8×10^{-5} mol cm^{-2} s^{-1} atm^{-2}, which is 26% lower than the value extracted from the model of mass transfer. Thus, even with a length scale for gas phase

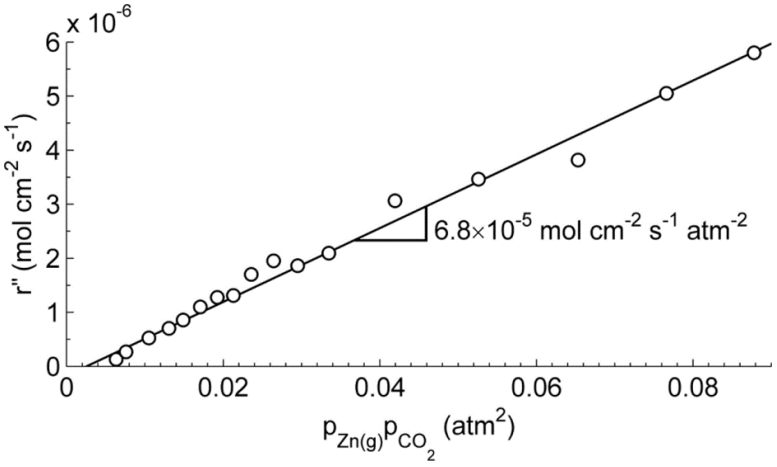

Figure 3.8 The rate of the heterogeneous oxidation of Zn(g) by CO_2 for T=1150 K as a function of the product of the mixing cup partial pressures of Zn(g) and CO_2. The slope of the best fit line corresponds to the apparent rate constant of the reaction including the combined effects of mass transfer and surface kinetics.

mass transfer as small as 1.95 mm (the radius of the oxidation tube), the rate of the heterogeneous oxidation of Zn(g) by CO_2 at 1150 K is fast enough to be on the order of the rate of mass transfer. This finding has important implications for the design of a CO_2 reduction reactor. To realize the full potential of the heterogeneous oxidation of Zn(g), the reactor should have length scales for mass transfer shorter than 1.95 mm, so that the rate of delivery of the Zn(g) and CO_2 reactants to the reaction surface does not slow the reaction.

For the oxidizing conditions in the CO_2–splitting experiments, the rate of the reverse reaction is negligible. According to the law of mass action, the forward and reverse reaction rate constants are related through the equilibrium constant according to:

$$K_{\mathrm{eq}} = \frac{k_{\mathrm{f}}}{k_{\mathrm{b}}} \tag{3.26}$$

The equilibrium constant is 1.5×10^{6} at 800 K and 2.4×10^{2} at 1150 K [76]. Applying the forward reaction rate constants measured in the present study, the reverse reaction rate constants are 8×10^{-8} at 800 K and 4×10^{-3} mol m^{-2} s^{-1} atm^{-1} at 1150 K. Using the CO partial

pressure at the reactor outlet, 0.001 atm at 800 K and 0.5 atm at 1150 K, the rate of the reverse reaction is estimated to be between 4×10^{-15} and 2×10^{-7} mol cm^{-2} s^{-1}. These rates are two or more orders of magnitude slower than the measured rates of Zn(g) oxidation at the respective temperatures, indicating that the reverse Zn(g) oxidation reaction is negligibly slow relative to the oxidation of Zn(g) by CO_2 for the conditions of the present study. On the other hand, in prior work, the reverse reaction was faster relative to the forward reaction because temperatures exceeded 1150 K where the equilibrium constant is closer to unity and CO partial pressures were higher, up to 0.9 atm [63]. To account for the reverse reaction, the prior kinetic expressions include a reverse reaction rate term [64, 67].

An explicit dependence of the rate expression for the heterogeneous oxidation of Zn(g) on CO_2 is important for reactor design. Without an explicit dependence of the rate on CO_2, a finite reaction rate is predicted even when there is insufficient CO_2 to react with the Zn(g). Consider the influence of the reacting flow field on the global reaction rates measured at 1100 K in case 5, where the CO_2 inlet mass flow rate is greater than the mass flow rate at the Zn inlet. The velocity field, Zn(g) concentration field, and CO_2 concentration field are shown in Fig. 9. The streamlines in Fig. 9(a) show that the rapid mass flow from the CO_2 inlet entrains the slower moving Zn(g)-Ar mixture away from the wall, carrying it downstream, as is seen in the Zn(g) and CO_2 concentration fields (Figs. 9(b) and (c)). CO_2 is present at a lower concentration than Zn(g) at the oxidation tube inner surface for the first 20 mm downstream of the reactor inlet. Over this length, CO_2 is the limiting reactant for oxidation, despite the fact that Zn(g) is the limiting reactant globally (Ψ=9.5) rendering the explicit dependence of the heterogeneous oxidation on CO_2 critical for capturing the kinetics. The rate expression obtained in the present work is general, and applies over a wide range of temperatures and Zn(g)/CO_2 concentrations.

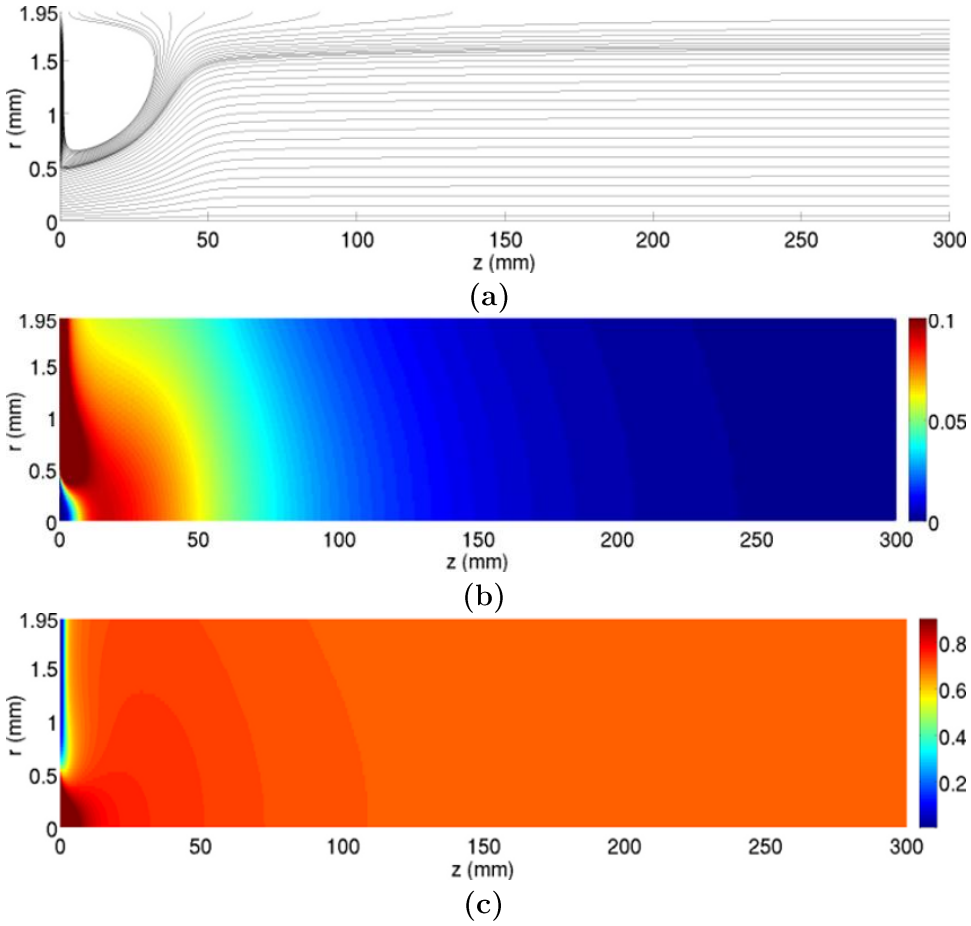

Figure 3.9 Streamlines (a), Zn(g) mass fraction contours (b), and CO_2 mass fraction contours (c) for the optimized simulation of experiment 7 (see Table 3.1).

3.3.1.2 H_2O System

Figure 3.10 shows the measured and predicted rates of the heterogeneous oxidation of Zn(g) by H_2O along the axis of the oxidation tube for temperatures between 800 K and 1100 K. Similar to the oxidation of Zn(g) by CO_2 over this temperature range, the rate of oxidation is on the order of 10^{-8}–10^{-5} mol cm^{-2} s^{-1}, faster than the characteristic rates of oxidation of solid Zn particles, which are less than ~10^{-8} mol cm^{-2} s^{-1} at 600–630 K [44]. The rate of oxidation increases to a maximum within 10 mm of the inlet as the Zn(g) and H_2O(g) species mix and then decays over ~50 mm as the reacting species are consumed. The model and the reaction rate data collapse using a second-order, reversible reaction rate expression with a linear dependence on both the Zn(g) and H_2O(g) concentrations:

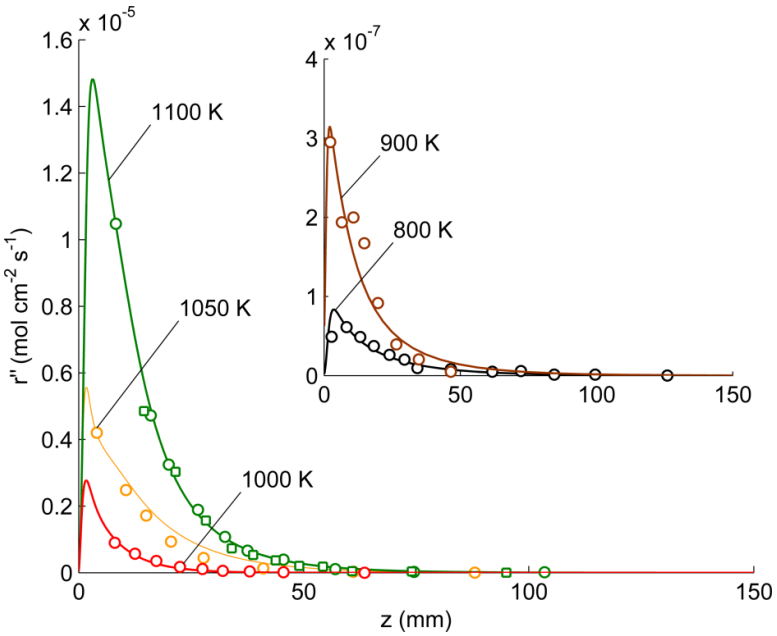

Figure 3.10 The rate of the heterogeneous oxidation of Zn(g) by H_2O as a function of axial position in the reactor for each set temperature. The points are the experimental data and the lines are the optimized model. At T = 1100 K, two sets of data are included to demonstrate repeatability. The circles correspond to experiment 6 in Table 3.2 and the squares correspond to experiment 7.

$$r'' = k_{\text{Zn-H}_2\text{O}}\left(p_{\text{Zn(g)}}p_{\text{H}_2\text{O}} - \frac{p_{\text{H}_2}}{K_{\text{eq}}}\right) \tag{3.27}$$

Temperature dependence of the reaction rate is captured in the parameter, $k_{\text{Zn-H}_2\text{O}}$, and the equilibrium constant, K_{eq}. The equilibrium constant corresponds to the overall $Zn(g)+H_2O(g)=ZnO(s)+H_2$ reaction, and is readily obtained from existing thermodynamic databases [76].

The values of the kinetic parameter determined from the optimized model are provided in Table 3.3 for each set temperature and are also shown in Arrhenius form in Figure 3.11. The kinetic parameter does not monotonically increase with temperature in the H_2O system as it does in the CO_2 system. Rather, the kinetic parameter decreases from 200 mol m^{-2} s^{-1} atm^{-2} at 800 K to 3.4 mol m^{-2} s^{-1} atm^{-2} at 1050 K, and then increases to 14 mol m^{-2} s^{-1} atm^{-2} at 1100 K. The unanticipated temperature dependence of the kinetic parameter is confirmed by the two experiments repeated at 900 K and 1100 K. The kinetic parameters of these two experiments are 59 and 60 mol m^{-2} s^{-1} atm^{-2} at 900 K and 15 and 17 mol m^{-2} s^{-1} atm^{-2} at 1100 K. The decrease of $k_{\text{Zn-H}_2\text{O}}$ over 800 to 1050 K implies that the reaction has a negative activation energy of -110±25 kJ/mol, a result that suggests that the reaction rate expression (3.27), while providing an acceptable fit to the data for the conditions in the present study, does not reflect the underlying chemical mechanism of the reaction, which consists of a series of more elementary chemical steps. While a negative apparent activation energy is uncommon, it has been reported in related metal oxide vapor deposition system [106, 107] and in other heterogeneous reaction system [108]. In addition, the increase in the kinetic parameter from 1050 K to 1100 K indicates that there is a change in the mechanism of the reaction, perhaps due to a transition from one elementary step limiting the rate of the reaction to another.

It is interesting to note that in the one other study of the heterogeneous oxidation of Zn(g) by $H_2O(g)$ (reviewed in Chapter 2), a similar trend of the kinetic parameters is

Table 3.3 The value of the kinetic parameter at each set temperature and for each experiment of Table 3.2 for reaction rate expression (3.27).

Experiment	T (K)	$k_{\text{Zn-H}_2\text{O}}$ (mol m^{-2} s^{-1} atm^{-2})
1	800	199
2	900	59
3	900	60
4	1000	6.8
5	1050	3.4
6	1100	14.5
7	1100	17.5

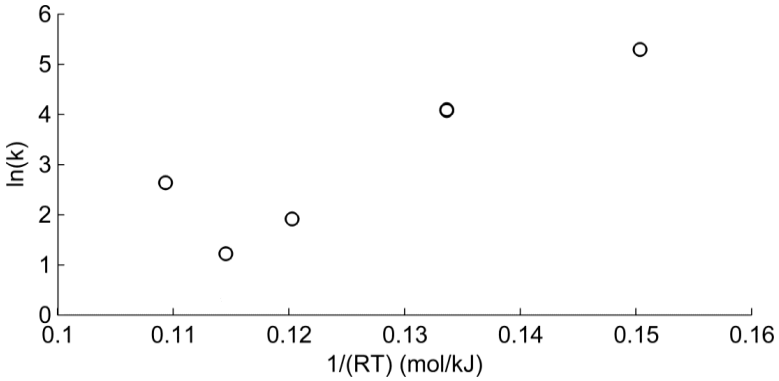

Figure 3.11 Arrhenius plot of the temperature dependent parameter (in units of mol m^{-2} s^{-1} atm^{-2}) determined for rate expression (3.27) via optimization of the mass transfer model for temperatures spanning 800 to 1100 K.

reported, albeit for a different kinetic expression. The kinetic parameters of the prior study are provided in Table 2.2. The parameter a decreases from 0.364 mol m^{-2} s^{-1} atm^{-2} at 781 K to 0.268 mol m^{-2} s^{-1} atm^{-2} at 1023 K, and then increases to 0.419 mol m^{-2} s^{-1} atm^{-2} at 1124 K. Both the present study and the prior study suggest that the underlying mechanism of the heterogeneous oxidation of Zn(g) by H_2O(g) is more complicated than is empirically captured by rate expressions (3.25) and (3.27). There are, however, important differences between the two studies, chiefly that the present study accounts for the radial transport of Zn(g) and H_2O on the measured heterogeneous oxidation rate, and the present data suggest that the influence of mass transfer is even more pronounced in the H_2O system than in the CO_2 system. The omission of the gas phase mass transfer in the prior study would lead to a bias error in the reported kinetic parameters such that they are underreported.

The effect of mass transfer on the heterogeneous oxidation of Zn(g) by H_2O(g) is elucidated when the measured reaction rate data are analyzed while neglecting its effects. Identical to the analysis completed in the CO_2 system, the product of the mixing cup partial pressure of Zn(g) and H_2O(g) along the tube axis are compared directly with the measured reaction rate at 1100 K. In so doing, it is assumed that the concentrations of the Zn(g) and H_2O(g) are uniform in the radial direction as would be the case if there were no resistance to mass transfer. At 1100 K, as shown in Figure 3.12, the apparent kinetic parameter is 3.4 mol m^{-2} s^{-1} atm^{-2}, and is 4 times below the value of 14 mol m^{-2} s^{-1} atm^{-2} obtained via application of the model for mass transfer. The factor of 4 difference shows that the mass transfer strongly influences the rate of oxidation in the present tube flow reactor. With more favorable conditions for mass transfer, i.e. a length scale shorter than

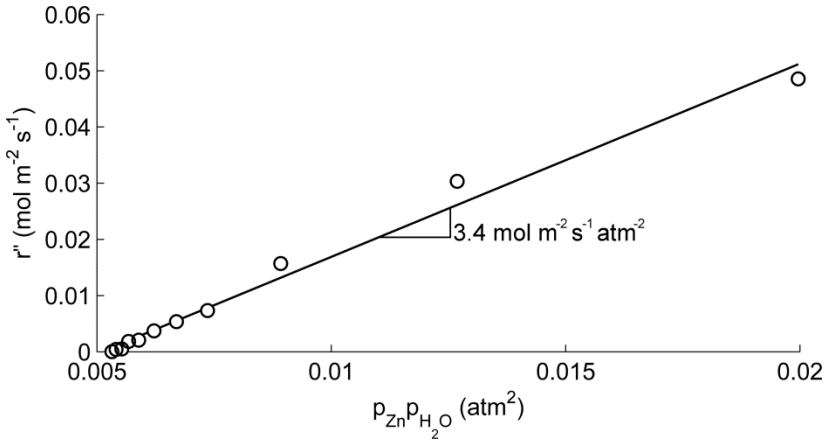

Figure 3.12 The rate of the heterogeneous oxidation of Zn(g) by H_2O for T=1100 K as a function of the product of the mixing cup partial pressures of Zn(g) and H_2O. The slope of the best fit line corresponds to the apparent rate constant of the reaction including the combined effects of mass transfer and surface kinetics.

the one present in the 3.9 mm i.d. oxidation tube, the rate of the heterogeneous oxidation would be faster than the rates shown in Figure 3.10, which are already on the order of 10^{-5} mol cm^{-2} s^{-1} at 1100 K.

Comparing reaction rate data measured in the 3.9 mm i.d. oxidation tube with the rate of reaction measured in a 15 mm i.d. tube provides additional evidence of the importance of mass transfer in the Zn(g)-H_2O(g) oxidation system. In the tubes with different inner diameters, the length scales for mass transfer differ, but the intrinsic surface reaction is unaltered. Thus, for similar reacting gas compositions, measured reaction rates should differ according to the different resistance to mass transfer in the two reacting systems. This difference is indeed observed at 1100 K, as shown in Figure 3.13, a plot of the gravimetrically measured oxidation rate along the tube axes. The rate of oxidation in the tube with a 3.9 mm i.d. is approximately 3 times larger than the rate of oxidation in the tube with a 15 mm i.d. This purely experimental result corroborates the results obtained from the coupling of the mass transfer model and data. Both the experimental result and

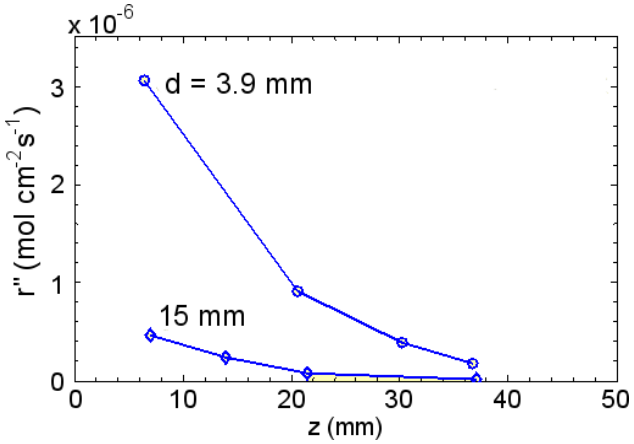

Figure 3.13 The rate of the heterogeneous oxidation of Zn(g) by H2O at 1100 K in a 3.9 mm i.d. tube and a 15 mm i.d. tube.

the numerical result point to the need to account for mass transfer when analyzing the measured reaction rates. The present study thus offers the first glimpse of kinetic parameter data that is free of mass transfer limitations.

A plausible alternative, and phenomenological based, reaction rate expression is now developed. Many surface reactions in which a solid product is deposited are known to follow the so-called precursor mechanism, which involves an elementary reaction between an adsorbed species and a gas species [109]. In the Zn(g) oxidation system, such a mechanism could be written as the sequence of:

$$H_2O+(*)\Leftrightarrow(H_2O) \tag{3.28}$$

$$Zn(g)+(H_20)\rightarrow(*)+H_2 \tag{3.29}$$

where (H_20) is an adsorbed water molecule, possibly appearing as hydroxyls on the ZnO surface, and $(*)$ is an available oxidation site. When the Zn(g) contacts the ZnO surface, it breaks the H-O bonds and incorporates itself in the ZnO lattice, releasing H_2 into the gas

flow. The overall reaction rate expression for this reaction sequence (derived in Appendix D) is:

$$r'' = \frac{k_2 K p_{\mathrm{Zn(g)}} p_{\mathrm{H_2O}}}{1 + K p_{\mathrm{H_2O}}} \tag{3.30}$$

Recasting equation (3.30) in a form similar to equation (3.27) gives

$$r'' = \left(\frac{k_2 K}{1 + K p_{\mathrm{H_2O}}} \right) p_{\mathrm{Zn(g)}} p_{\mathrm{H_2O}}, \tag{3.31}$$

where the term in the brackets is the equivalent second-order reaction rate parameter:

$$k_{\mathrm{Zn\text{-}H_2O}} = \left(\frac{k_2 K}{1 + K p_{\mathrm{H_2O}}} \right) \tag{3.32}$$

K is the equilibirium constant for the adsorption of H_2O on ZnO. Adsorption is an exothermic process ($\Delta \bar{H}_{\mathrm{ads}} < 0$), and from the Van't Hoff equation,

$$\frac{d(\ln K)}{dT} = \frac{\Delta \bar{H}_{\mathrm{ads}}}{RT^2}, \tag{3.33}$$

it is known that K decreases with increasing temperature. k_2 is the forward reaction rate constant for reaction (3.29) and monotonically increases with temperature with an activation energy, E_{A}, following the Arrhenius equation:

$$\frac{d(\ln k_2)}{dT} = \frac{E_{\mathrm{A}}}{RT^2} \tag{3.34}$$

The form of rate equation (3.31), and thus the precursor mechanism, could explain the decreasing trend of the second-order kinetic parameter with temperature, i.e., the apparent negative activation energy over the temperature range 800 to 1050 K. If $K p_{\mathrm{H_2O}} \ll 1$, then $k_{\mathrm{Zn\text{-}H_2O}} \cong k_2 K$. In this case, the apparent activation energy of the second-order kinetic parameter is equal to the sum of the activation energy of the rate-limiting elementary chemical step and the heat of adsorption of H_2O.

$$E^* = E_A + \Delta\bar{H}_{ads} \tag{3.35}$$

As noted, the heat of adsorption is negative, and if its magnitude is larger than the activation energy of the elementary rate-limiting chemical step, than the apparent activation energy will be negative, as is the case in the present and prior studies. Data available for the heat of adsorption of H_2O on polycrystalline ZnO show that it depends on the surface coverage of H_2O [110]. At low coverage, the heat of adsorption is -100 kJ/mol; it increases to a maximum of -160 kJ/mol when 80% of available adsorption sites are filled. The apparent activation energy of -110±25 kJ/mol falls on the low end of this reported range of heats of adsorption, consistent with the notion that the activation energy of the elementary chemical conversion step is low compared to the heat of adsorption of H_2O. If the precursor mechanism is the mechanism by which Zn(g) is oxidized by H_2O, combining the apparent activation energy from the present study and the reported heat of adsorption suggests that the activation energy of the elementary chemical conversion step is between 15 and 75 kJ/mol.

Unfortunately, the proposed precursor mechanism cannot be explored further in the present study because the data are limited to H_2O partial pressures from 0 to 0.4 atm. Optimization of the data using reaction rate expression (3.30) reveals that the measured reaction rate data are insensitive to the Kp_{H_2O} term over these concentrations. For example, the measured rate data at T = 800 K is compared to the rate predicted by the model with k_2 = 1990 mol m^{-2} s^{-1} atm^{-2} and K = 0.1 and k_2 = 19.9 mol m^{-2} s^{-1} atm^{-2} and K = 10 in Figure 3.14. The predicted rates from both sets of kinetic parameters match the measured reaction rate data because the k_2K product is 199 mol m^{-2} s^{-1} atm^{-2}, the value of the second-order reaction rate expression kinetic parameter determined for T = 800 K (Table 3.3). The maximum difference between the predicted reactions rates is 0.2×10^{-8}

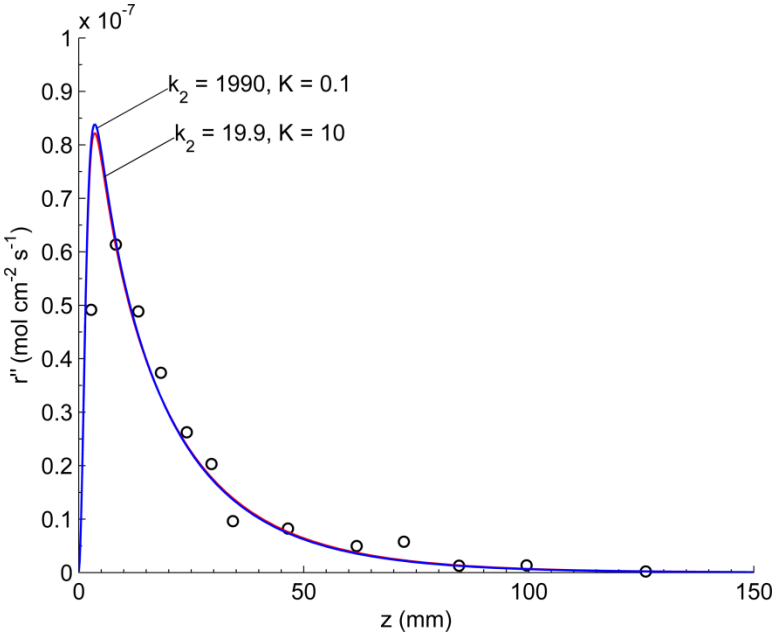

Figure 3.14 The measured rate of the heterogeneous oxidation of Zn(g) by H_2O(g), compared with the predicted rate of oxidation using the precursor mechanism kinetic expression with the two sets of kinetic parameters indicated.

mol cm^{-2} s^{-1} (~2%), which is on the order of the experimental uncertainty in the measured rate. Additional experiments are required to determine whether the precursor mechanism is the mechanism by which Zn(g) is oxidized by H_2O. For example, an experiment in which $Kp_{H_2O} \gg 1$ would allow k_2 to be measured directly since the precursor mechanism rate expression reduces to:

$$r'' = k_2 p_{Zn(g)} \tag{3.36}$$

Given the plausibility of the precursor mechanism for explaining the reaction data in the H_2O-splitting system, and bearing in mind the speculative nature of the discussion, it is reasonable to wonder why a negative activation energy was not measured for the CO_2-splitting system. If the oxidation of Zn(g) by CO_2 also follows the precursor mechanism, then the fact that the activation energy measured for the second-order rate expression kinetic parameter suggests that either the magnitude of the heat of adsorption

of CO_2 onto ZnO is lower than that of H_2O, the activation energy of the elementary chemical step is higher, or both. There is evidence for the first case. The heat of adsorption measured on polycrystalline ZnO is 20–80 kJ/mol lower in magnitude than the heat of adsorption of H_2O [111].

3.3.2 The Heterogeneous Oxidation of Zn(g) for Rapid H_2 and CO Production

With knowledge of the mass transfer and intrinsic surface kinetics, the reaction rate data are more easily interpreted. The rate of the heterogeneous oxidation of Zn(g) by both H_2O and CO_2 is rapid, but the rate of oxidation by H_2O is even faster than that for CO_2 at a given temperature and for a similar reacting flow. The difference is evident in the measured reaction rates. Compare the rate of the heterogeneous oxidation of Zn(g) at 1100 K in Figure 3.6 for the CO_2 system and in Figure 3.10 for the H_2O system. The maximum measured rate of oxidation near the inlet in the H_2O system is 1.05×10^{-5} mol cm^{-2} s^{-1}, triple that of the maximum rate of oxidation in the CO_2 system, 0.32×10^{-5} mol cm^{-2} s^{-1}. As a result of the rapid rate of Zn(g) oxidation in the H_2O system relative to the CO_2 system, the Zn(g) and H_2O are more rapidly consumed from the reacting flow, and the rate of oxidation decreases more rapidly along the tube axis, approaching zero near z = 50 mm (Figure 3.6). In the CO_2 system, additional reacting length, or, equivalently, residence time, is required for the reactants to be consumed and the rate of oxidation approachs zero closer to z = 200 mm (Figure 3.10).

The inherently different kinetics of H_2O- and CO_2-splitting are also apparent from the kinetic expressions developed. Using reaction rate expressions (3.25) and (3.27) and their associated temperature dependent kinetic parameters, the rates of the oxidation of Zn(g) by H_2O(g) and CO_2 are compared at 800, 1000, and 1100 K for reacting conditions where $p_{Zn(g)} = p_{H_2O}$ and $p_{Zn(g)} = p_{CO_2}$ and for partial pressures up to $p_{Zn,sat}$. The rates predicted are shown in Figure 3.15. The dependence of the rate of oxidation on the partial pressure

of Zn(g) is parabolic because the kinetics are, overall, second-order, proportional to both the Zn(g) and H_2O/CO_2 concentrations. The parabolic shape thus reflects the fact that the concentration of Zn(g) is taken to be equal to the that of H_2O and CO_2. At 1100 K, H_2O oxidizes Zn(g) 18 times faster than CO_2; at partial pressures of 0.1 atm, the rate of oxidation by H_2O is 1.42×10^{-5} mol cm^{-2} s^{-1} and the rate of oxidation by CO_2 is 7.57×10^{-7} mol cm^{-2} s^{-1}. The dramatic difference in kinetics holds across the temperature range from 800 K to 1100 K. The inset of Figure 3.15 compares the rates of oxidation at 800 K. At this temperature, the rate of the heterogeneous oxidation of Zn(g) by H_2O is up to three

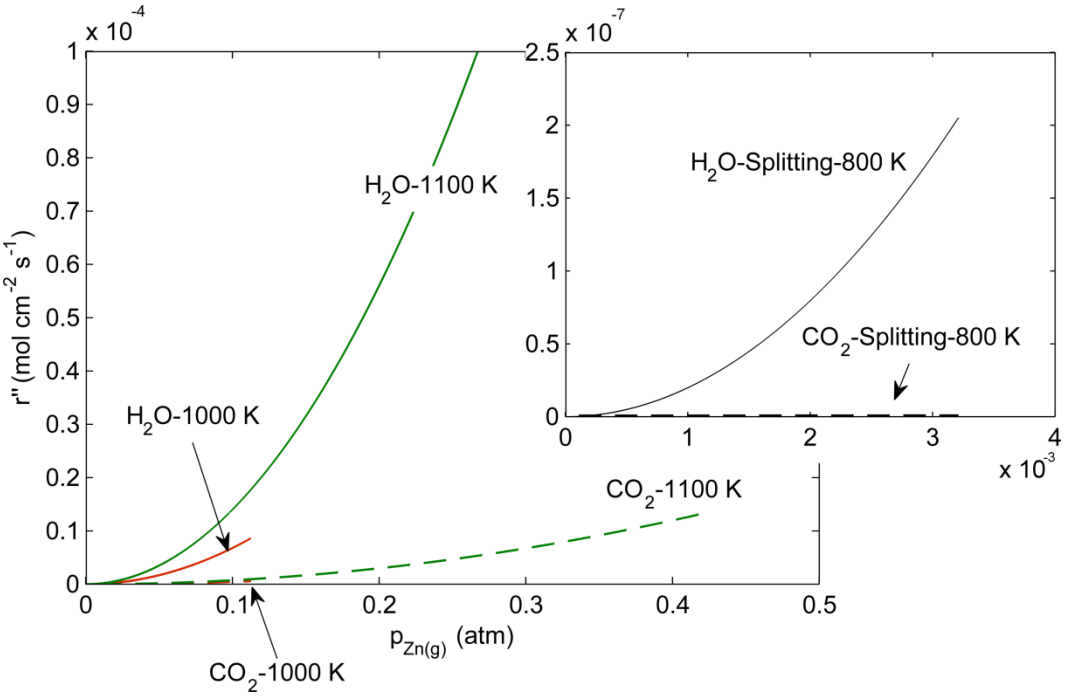

Figure 3.15 Comparison of the rate of H_2O-splitting (solid lines) and CO_2-splitting (dashed lines) via the heterogeneous oxidation of Zn(g) at 1000 K and 1100 K for Zn(g) partial pressures up to the saturation pressure at each temperatures. The partial pressures of CO_2 and H_2O are assumed to be equal to the Zn(g) partial pressure.

orders of magnitude faster than the oxidation rate by CO_2, e.g., at 0.003 atm, H_2O oxidizes Zn(g) at a rate of ~1×10^{-7} mol cm^{-2} s^{-1} while CO_2 oxidizes Zn(g) at a rate closer to ~1×10^{-10}. The rate of oxidation of Zn(g) by CO_2 can be increased by raising the CO_2 concentration. The rate of the heterogeneous oxidation of Zn(g) increases with temperature in both the CO_2 and the H_2O reaction systems, but the overall increase is a result of different effects in the two systems. Consider Zn(g) oxidation by CO_2. The oxidation rate increases dramatically with temperature because of the temperature-induced enhancement of kinetics via the monotonically increasing kinetic parameter (Figure 3.7) and because of the larger concentrations of Zn(g) achieved due to the elevated zinc saturation partial pressure (Figure 2.3). Both of these effects increase exponentially with temperature, as is evident in the measured rates of heterogeneous Zn(g) oxidation (Figure 3.6) and the total rate of CO production (Figure 3.3(a)). The rate of the heterogeneous oxidation of Zn(g) increases 2–3 orders of magnitude for a 350 K temperature increase from ~10^{-8} mol cm^{-2} s^{-1} at 800 K to ~10^{-5} mol cm^{-2} s^{-1} 1150 K. Similarly, the rate of CO production grows from 0.005 mmol/min at 800 K to 2.6 mmol/min at 1150 K.

In contrast, the increase in overall reaction rate with increasing temperature in the case of H_2O-splitting is due mostly to the higher Zn(g) concentrations achieved at higher temperatures, given the decrease of the kinetic parameter, $k_{\mathrm{Zn\text{-}H_2O}}$, with temperature from 800 to 1050 K (Figure 3.11). From a kinetic perspective, it is beneficial to heterogeneously oxidize Zn(g) at high temperatures. Conversely, from a thermodynamic perspective, lower temperatures where complete conversion of Zn(g) is favored are desired (Figure 2.4), as discussed in Chapter 2. These competing effects suggest that a reactor built for producing H_2 and CO from H_2O and CO_2 in the Zn/ZnO thermochemical cycle should operate with a temperature gradient. At the inlet of the reactor, the temperature should be higher to attain high Zn(g) concentrations and rapid kinetics. As the reaction proceeds and Zn(g) is

consumed, the temperature should be reduced to shift the chemical equilibrium towards complete conversion of Zn(g).

An additional consideration for H_2 and CO production in the solar thermochemical cycles is the carrier gas requirement, which is strongly linked to the Zn saturation pressure. It is advantageous to minimize the carrier gas requirement, and a reactor operated under a temperature gradient is also beneficial to achieve this goal. Table 3.1 and Table 3.2 show that at 800 K and 900 K, where the Zn saturation pressure is low, the concentration of Zn(g) at the reactor inlet is less than 3 mol%. As a result, the reacting flow is composed of mostly inert Ar. Heating the inert Ar will lower the thermal efficiency of fuel production unless the sensible energy is recuperated after oxidation. At higher oxidation temperatures, the Ar required is significantly reduced. For example, in the CO_2-splitting experiment at 1150 K, Ar represents just 30 mol% of the reaction flow, reducing the detrimental impact on thermal efficiency. For this reacting mixture, the fraction of the energy required to heat the reacting flow to the oxidation temperature that goes toward heating Ar is 6%. A heterogeneous Zn(g) oxidation reactor operated with a temperature gradient thus, in addition to achieving rapid and complete conversions, also reduces inert carrier gas requirements.

There are a number of benefits of the rapid kinetics of the heterogeneous oxidation of Zn(g) by H_2O and CO_2. First, and of utmost importance for the efficiency of H_2 and CO production as will be discussed further in Chapter 4, less than a second is required to oxidize more than 80% of the Zn(g) by CO_2 and more than 75% of the Zn(g) by H_2O over 800 to 1150 K (Table 3.1 and Table 3.2). More zinc is converted at lower temperatures in both the H_2O and CO_2 systems, and there are interesting differences in the trend of conversion with temperature. In the H_2O system, zinc conversion increases from ~80% at 1100 K to 100% at 800 K. In the CO_2 system, zinc conversion increases from 88% at 1150 K to 98% at 1100 K, but then decreases to 94% at 800 and 900 K. The different trends

can be traced to the inherent differences in the kinetics of H_2O- and CO_2-splitting via the oxidation of Zn(g). At 800–900 K, the rate of oxidation of Zn(g) by H_2O is ~100 times faster than the rate of oxidation by CO_2. Consequently, the 0.5–0.7 s residence time in the H_2O-splitting experiments is sufficient to reach thermodynamic equilibrium and completely convert the Zn. In contrast, the 0.8–1.0 s residence time in the CO_2 system is insufficient to approach the complete conversion thermodynamically predicted. The zinc conversion decreases at temperatures above 1000 K in both the H_2O and CO_2 systems as the reactions become slightly less favored thermodynamically, as predicted with Gibbs free energy minimization (Figure 2.5). Increasing the oxidation time is expected to increase the zinc conversion, pushing conversions closer to those predicted at chemical equilibrium. Note that the oxidation of zinc powders is practically limited to conversions of 80% over the course of minutes [43, 44, 46]. Higher conversions are demonstrated in this work over the course of seconds.

The second benefit of the rapid rate of the heterogeneous oxidation of Zn(g) by H_2O and CO_2 is rapid H_2 and CO production rates, as shown in Figure 3.3. The rate of fuel production grows exponentially with temperature from 0.005 mmol/min at 800 K to 2.6 mmol/min at 1150 K considering both H_2O- and CO_2-splitting. The increase in the rate of fuel production follows the increase in the zinc saturation pressure (compare Figure 2.3 and Figure 3.3), demonstrating the benefit of achieving large Zn(g) partial pressures at higher temperatures.

3.4 Summary

In this chapter, the study of the heterogeneous oxidation of Zn(g) was presented. This reaction pathway is a promising approach for producing H_2 and CO in the solar thermochemical Zn/ZnO cycle.

The rate of the heterogeneous oxidation of Zn(g) was measured gravimetrically in a quartz tubular flow reactor, and rate expressions for the intrinsic surface kinetics for Zn(g) oxidation by H_2O and CO_2 were developed using a finite volume model of the reacting flow. The kinetic expressions obtained are suitable for reacting environments that reflect those that may be used in the two-step Zn/ZnO solar thermochemical cycle. The numerical model decouples the influence of surface kinetics and gas phase reacting species transport from the measured rates of heterogeneous Zn(g) oxidation so that the kinetic expressions reflect the intrinsic surface reaction rates.

The rate of the heterogeneous oxidation of Zn(g) by H_2O and CO_2 is rapid, on the order of 10^{-8} to 10^{-5} mol cm^{-2} s^{-1} for temperatures between 800 and 1150 K. Furthermore, it is not subject to a kinetically limiting diffusion barrier. As a result, conversions of Zn greater than 80% are possible by both H_2O and CO_2 with oxidation times less than a second, representing a substantial improvement over the oxidation of solid and liquid Zn [47, 48, 112].

Gaseous zinc oxidation kinetics in the CO_2 system are, overall, second-order, proportional to both the Zn(g) and CO_2 concentrations for temperatures between 800 and 1150 K and for Zn(g) and CO_2 concentrations up to 69 and 80 wt%, respectively. Temperature dependence of the kinetic parameter in the rate expression is captured in an Arrhenius expression with an activation energy of 44±3 kJ/mol and a pre-exponential factor of 92±6 mol m^{-2} s^{-1} atm^{-2}.

A second-order, reversible rate equation describes the reaction rate data for H_2O-splitting. The kinetic parameter decreases with temperature from 800 K to 1050 K, with an apparent activation energy of -110±25 kJ/mol. This anomalous behavior suggests that the underlying mechanism for the conversion of Zn(g) and H_2O to ZnO and H_2 is not captured by the law of mass action based rate equation. A precursor mechanism is proposed to explain the kinetic behavior. Additionally, the kinetic parameter increases

from 3.4 mol m^{-2} s^{-1} atm^{-2} at 1050 K to 16 mol m^{-2} s^{-1} atm^{-2} at 1100 K indicating that there is a change in the reaction mechanism near 1050 K. Similar kinetic behavior is reported in a prior study on the heterogeneous oxidation of Zn(g) by H_2O [61]. The prior study omitted gas phase mass transfer, however, which was shown to significantly influence the measured reaction rates when the diffusion length scale is on the order of 1.4 mm.

The present work confirms that substantial improvements in the efficiency of the Zn/ZnO thermochemical cycle for producing H_2 and CO from H_2O and CO_2 are possible if the critical Zn oxidation step were to utilize the heterogeneous oxidation of Zn(g). In the following chapter, this thermodynamic benefit is quantified.

4 Energy and Entropy Analyses

A parametric thermodynamic analysis is completed to show the energetic benefit of the heterogeneous oxidation of Zn(g) for the production of H_2 and CO in the two-step Zn/ZnO thermochemical redox cycle. Mass, energy, and entropy flows are balanced to determine the fraction of the concentrated solar energy input stored in the H_2 and CO fuels and process irreversibility. The analysis reveals the critical importance of achieving high conversions of Zn in the H_2 and CO production step of the cycle. This chapter appears in Ref. [113], and has been used with permission (see Appendix H).

4.1 Model of the Zn/ZnO Solar Thermochemical Cycle

A mass, energy, and entropy balance is conducted on each process in the two-step Zn/ZnO solar thermochemical cycle. The efficiency of the cycle is calculated and the most irreversible process is identified. The oxidation temperature and the conversion of zinc are parameters in the analysis that allow for various zinc oxidation reaction paths to be compared. Thermochemical data were obtained from the HSC 7.0 database [76].

The process flow sheet for the two-step Zn/ZnO thermochemical cycle is shown in Figure 4.1. This figure reflects the mass and energy flows required for the steady-state production of one mol s^{-1} of H_2 or CO. All flows and processes in the cycle occur at a pressure of one atmosphere, and the work required for moving material is neglected. The cycle begins at the solar reactor, **I**, in the endothermic chemical step denoted by the dashed box **EN**. The solar reactor thermally dissociates A mol s^{-1} of ZnO to A mol s^{-1} of Zn(g) and $0.5A$ mol s^{-1} of O_2(g) at T_{solar}, assumed to be 2300 K. At this temperature,

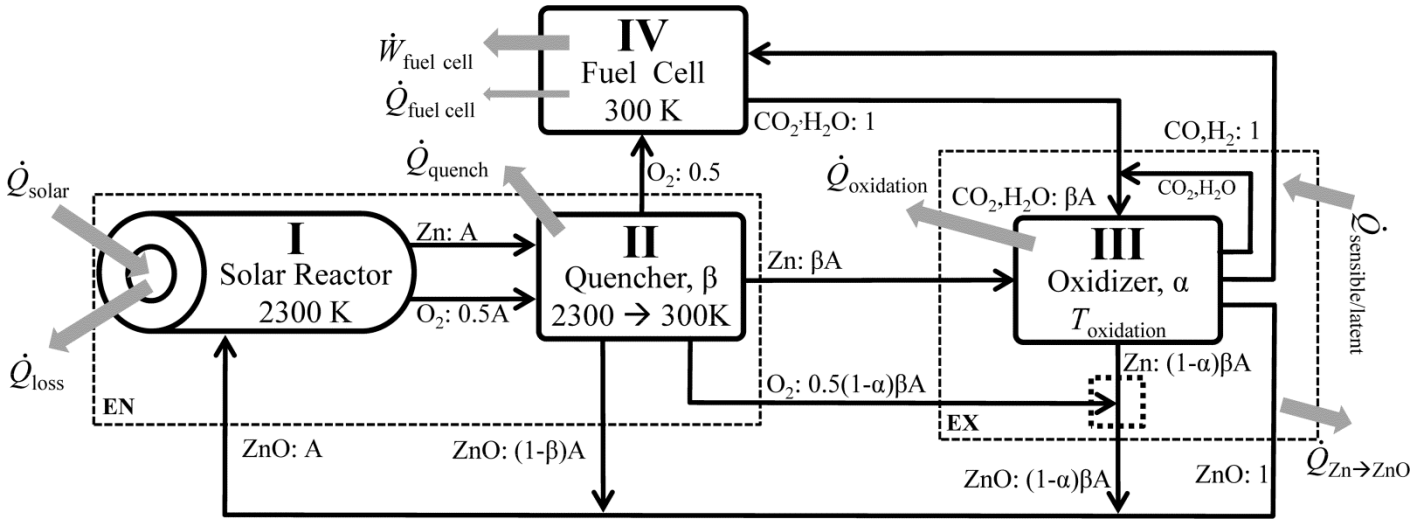

Figure 4.1 Material flow (black arrows) and energy flow (gray arrows) in the two-step Zn/ZnO solar thermochemical cycle for H_2O or CO_2 splitting. All material flows are assumed to be at 1 atm, and pumping work is neglected.

the change in the Gibbs free energy upon ZnO dissociation is approximately zero. The value of A depends on the chemical conversion achieved in the oxidizer, α, and on the yield of zinc in the quencher, β.

$$A = \frac{1}{\alpha\beta} \tag{4.1}$$

The quencher, **II**, reduces the temperature of the Zn(g) and $0.5O_2$ gas product streams to 300 K so that Zn(g) condenses. Some recombination of the Zn(g) and O_2 is unavoidable due to the rapid kinetics of the oxidation of Zn(g) by oxygen [33]. If there is a complete conversion of Zn to ZnO in the oxidizer and a 100% yield of zinc in the quencher, $A = 1$. For incomplete conversion or an incomplete yield of zinc, $A > 1$ to reflect the additional Zn/ZnO and H_2O or CO_2 needed to produce a unit of H_2 or CO. The concentrated solar radiation supplied to the solar reactor, $\dot{Q}_{\text{solar}}$, must heat and transform the ZnO into Zn(g) and O_2 and, in addition, overcome the radiative loss through the reactor's aperture. The radiative loss is quantified by the absorption efficiency, which is defined as the ratio of the net rate at which energy is absorbed to heat and dissociate the zinc oxide, $\dot{n}_{\text{ZnO}}\left(\int_{300\text{ K}}^{T_{\text{solar}}} \bar{c}_{\text{ZnO}}\, dT + \Delta\overline{H}_{\text{solar}}\right)$, to the rate of concentrated solar gain, $\dot{Q}_{\text{solar}}$. The change in the enthalpy upon ZnO dissociation is $\Delta\overline{H}_{\text{solar}} = 450$ kJ/mol at 2300 K. If the solar reactor is assumed to be a perfectly insulated and black cavity receiver, the solar input is given by

$$\begin{aligned}\dot{Q}_{\text{solar}} &= \frac{\dot{n}_{\text{ZnO}}\left(\int_{300\text{ K}}^{T_{\text{solar}}} \bar{c}_{\text{ZnO}}\, dT + \Delta\overline{H}_{\text{solar}}\right)}{\eta_{\text{absorption}}} \\ &= \dot{n}_{\text{ZnO}}\left(\int_{300\text{ K}}^{T_{\text{solar}}} \bar{c}_{\text{ZnO}}\, dT + \Delta\overline{H}_{\text{solar}}\right)\left(1 - \frac{\sigma T_{\text{solar}}^4}{IC}\right)^{-1}\end{aligned} \tag{4.2}$$

where I is taken to be 1000 W m^{-2}, and C is the solar concentration ratio. In the present analysis, the concentration ratio was taken to be 10,000. The combination of $T_{\text{solar}} =$ 2300 K and $C = 10{,}000$ yields near optimal efficiency where the efficiency is the product of $\eta_{\text{Carnot}}\eta_{\text{absorption}}$ [23].

The quench process is modeled as a heat loss at constant pressure. The rate of heat loss is given by an energy balance:

$$\dot{Q} = \left(\sum_{\mathrm{j}} \dot{n}_{\mathrm{j}} \bar{h}_{\mathrm{j}} \right)_{\mathrm{out}} - \left(\sum_{\mathrm{i}} \dot{n}_{\mathrm{i}} \bar{h}_{\mathrm{i}} \right)_{\mathrm{in}} \tag{4.3}$$

The energy balance is expressed generally and application to a particular process is denoted as shown in Figure 4.1. The enthalpy contribution of each species is additive over the species entering the process, i, and exiting the process, j, assuming ideal mixture behavior. In the particular case of the quencher, Zn(g) and O_2 are present in the inflow and Zn(s), O_2, and ZnO are present in the outflow due to the recombination of Zn and O_2. A fraction β of the dissociated zinc is recovered from the quencher, while the fraction $(1-\beta)$ that recombines to zinc oxide is recycled to the solar reactor. Of the oxygen exiting the quencher, 0.5 mol s^{-1} is sent to a fuel cell, **IV**, and the remaining oxygen is sent downstream where it is recombined with unreacted zinc from the oxidizer, **III**, at ambient temperature. During recombination, some energy is released, $\dot{Q}_{\mathrm{Zn \rightarrow ZnO}}$. In practice, unreacted zinc would not be recombined with oxygen to form zinc oxide. In the present analysis, this process is added to close the zinc oxide material loop in the cycle so that the cycle can be analyzed in the context of a heat engine. The irreversibility associated with converting the unreacted Zn to ZnO also provides a quantitative measure of the thermodynamic cost associated with incomplete conversion of the Zn in the oxidizer.

The oxidizer, **III**, combines zinc and water or carbon dioxide to produce zinc oxide and hydrogen or carbon monoxide, completing the exothermic step of the cycle denoted by the dashed box **EX**. Depending on the reaction path utilized in the oxidizer, temperatures can vary between 300 and 1200 K. The energy required for heating the reactants is $\dot{Q}_{\mathrm{sensible/latent}}$. A fraction α of the zinc is converted to hydrogen or carbon monoxide and zinc oxide. The unreacted water or carbon dioxide is immediately recycled, and is

maintained at the oxidation temperature. The energy released during the oxidation of zinc and subsequent cooling of the H_2/CO and zinc oxide products is $\dot{Q}_{\text{oxidation}}$, and if not recuperated, is rejected to the environment at 300 K.

The hydrogen or carbon monoxide produced in the oxidizer is sent to a fuel cell, **IV,** that reversibly combines it with the oxygen from the quencher to produce useful work (electricity) and regenerate water or carbon dioxide to be returned to the oxidizer. The fuel cell closes the hydrogen or carbon monoxide material loop, and assigns a value to the energy stored chemically. The amount of work generated is given by the change in the Gibbs free energy during the formation of water or carbon dioxide.

$$\dot{W}_{\text{fuel cell}} = \dot{n}_{\text{H}_2,\text{CO}} \Delta \bar{G}_{300\text{ K}} \tag{4.4}$$

In the formation of water, $\Delta \bar{G}_{300\text{ K}}$ =-237 kJ/mol, and in the formation of carbon dioxide, $\Delta \bar{G}_{300\text{ K}}$ =-257 kJ/mol. The energy not output as useful work in the fuel cell is released as heat.

$$\dot{Q}_{\text{fuel cell}} = \dot{n}_{\text{H}_2,\text{CO}} (300\text{ K} \times \Delta \bar{S}_{300\text{ K}}) \tag{4.5}$$

An entropy balance on each process determines the irreversibility:

$$\dot{S}_{\text{gen}} = \sum \frac{-\dot{Q}}{T_s} + \left(\sum_j \dot{n}_j \bar{s}_j \right)_{\text{out}} - \left(\sum_i \dot{n}_i \bar{s}_i \right)_{\text{in}} \tag{4.6}$$

T_s is the temperature of the thermal reservoir with which heat is being exchanged, 300 K for heat rejections and 2300 K for heat additions. It is assumed that all energy additions to the cycle originate from the same heat reservoir (the solar reactor).

The efficiency of the cycle is defined as the fraction of the heat input converted to chemical energy, quantified by the work output of the fuel cell:

$$\eta_{\text{cycle}} = \frac{\left|\dot{W}_{\text{fuel cell}}\right|}{\sum \dot{Q}_{\text{in}}} \tag{4.7}$$

Thermal energy is required in the solar reactor to heat and dissociate ZnO and overcome the radiative loss. Thermal energy is also required to heat and, if necessary, melt or vaporize the oxidation reactants (Zn, H_2O, CO_2). Because the work output represents the amount of hydrogen or carbon monoxide produced (the change in Gibbs free energy is a fixed quantity) and the H_2/CO production rate is one mol s^{-1}, the denominator of equation (4.7) is the amount of thermal energy required to produce a unit of H_2 or CO. Achieving high efficiency is thus important for minimizing the size and costs associated with the solar concentration equipment [17, 114, 115].

4.2 Results and Discussion

The influence of the oxidation temperature on the efficiency of the Zn/ZnO water and carbon dioxide splitting cycles is shown in Figure 4.2 for temperatures between 300 and 1200 K. Below ~1200 K, the oxidation of zinc by H_2O and CO_2 is thermodynamically favored, as shown in Figure 2.4. In Figure 4.2 it is assumed that complete conversion is achieved in both reaction steps of the cycle so that $\alpha = \beta = 1$. The two curves on each graph correspond to cycles with and without heat recuperation.

Consider the cycles without heat recuperation. The theoretical maximum cycle efficiency of 36% for water splitting or 39% for carbon dioxide splitting is achieved when the oxidation temperature is 300 K, in agreement with [17] and [114]. When it is necessary to heat and melt or vaporize the zinc, water, or carbon dioxide reactants, the theoretical maximum efficiency is reduced. Abrupt decreases in the efficiency occur at the vaporization temperatures of water and zinc, 373 and 1180 K, respectively, where the latent energies of vaporization must be supplied. In the water splitting cycle, the latent energies of vaporization of zinc and water represent 71% of the overall efficiency reduction

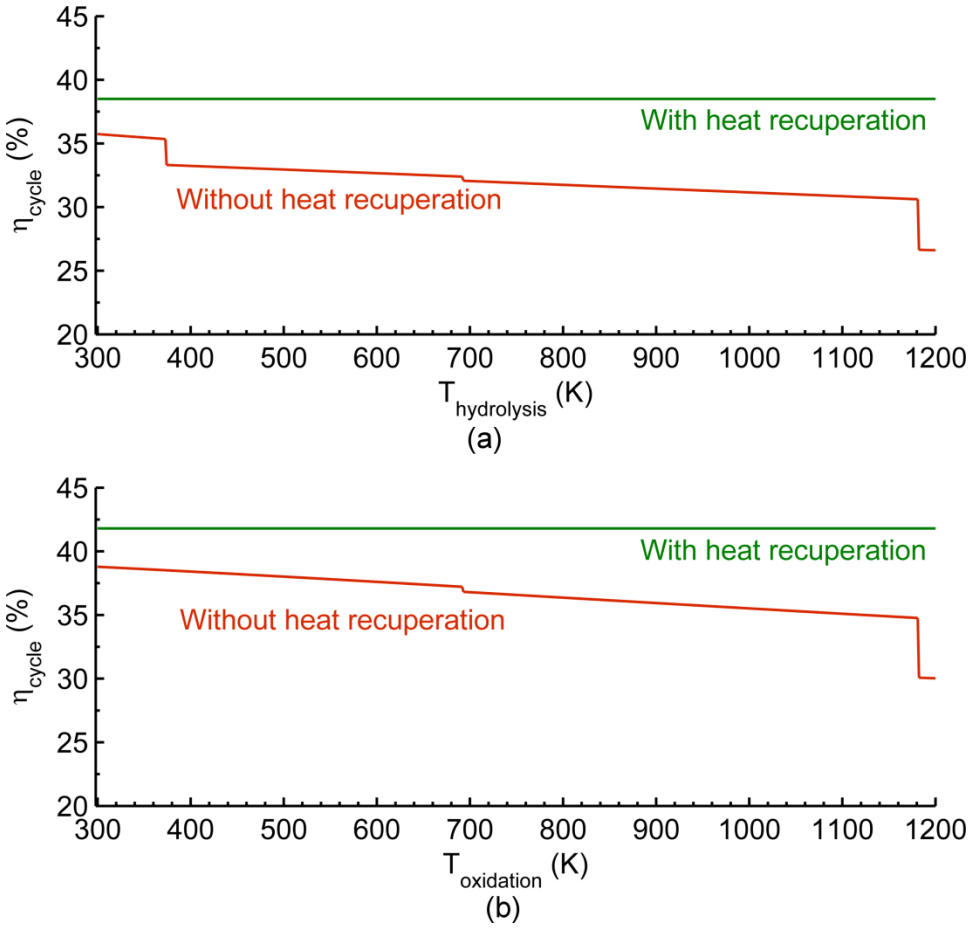

Figure 4.2 Impact of the oxidation temperature on cycle efficiency for (a) H_2O- and (b) CO_2-splitting. T_{solar}=2300 K, C=10,000, and α=β=1.

from 36% at 300 K to 27% at 1185 K. For carbon dioxide splitting, only zinc must be vaporized, and vaporization represents 50% of the cycle efficiency reduction from 39% at 300 K to 31% at 1185 K. For temperatures between the vaporization temperatures of water and zinc, efficiency is a weak function of temperature. For example, increasing the hydrolysis temperature from 800 to 1000 K reduces the water splitting cycle efficiency from 33% to 32%. Given that kinetics is a strong function of temperature, the efficiency reduction incurred from increasing the hydrolysis temperature from 800 to 1000 K is small compared to the improvement in reaction kinetics. Thus, in the case without heat recuperation and within the bands bounded by the vaporization points of water and zinc, the oxidation temperature should be selected to optimize kinetics.

It is possible to recuperate some of the thermal energy released in the cycle, i.e., between the energy released in the quencher and the ZnO entering the solar reactor and between the energy released in the oxidizer and the oxidation reactants. If complete recuperation (without heat transfer limitations) is considered, cycle efficiency is improved over all hydrolysis/oxidation temperatures (Figure 4.2). There is a thermodynamic limit, however, to the amount of heat that can be recuperated from the quencher. Figure 4.3 is a plot of the temperatures of the $Zn+0.5O_2$ streams and the ZnO as these materials exchange energy with one another. As energy from the $Zn+0.5O_2$ stream is passed to the ZnO, the temperatures of the two streams increase or decrease until they reach a pinch point at 1180 K. Additional energy cannot be exchanged without violating the second law of thermodynamics. The amount of energy that can be recuperated from the quencher to preheat ZnO is thus limited to 19% of the thermal energy available in the $Zn+0.5O_2$ streams exiting the solar reactor. In addition to this thermodynamic limit, there is also a practical limit to the amount of energy that can be recuperated in the quench step if the change in the temperature of an intermediate quenching fluid is small.

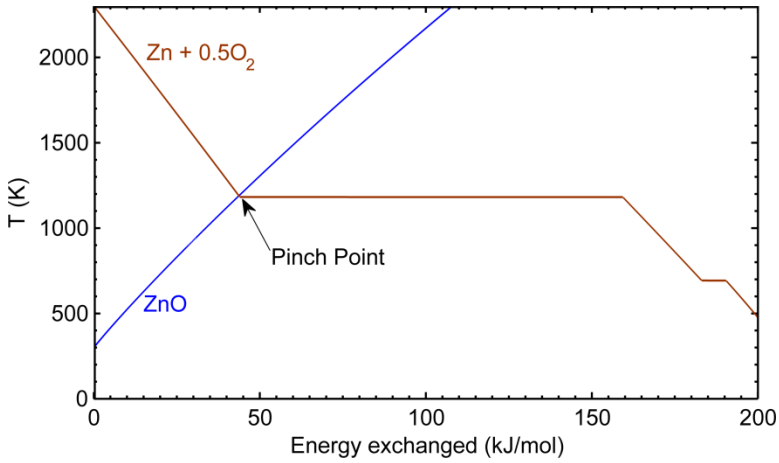

Figure 4.3 Temperature of the ZnO and Zn+0.5O_2 flows as they exchange energy with one another in the case where there is no recombination of Zn(g) and O_2 (β=1)

Energy exchange between the oxidizer and the Zn+H_2O or Zn+CO_2 is not limited by a pinch point. Enough energy is released during the oxidation to supply most of the energy required to raise the temperature and change the phase of the Zn/H_2O or Zn/CO_2 reactants. For example, at an oxidation temperature of 1185 K and when $\alpha = \beta = 1$, 221 kJ/mol of energy is released when one mole of H_2O is split and 188 kJ/mol of energy is released when one mole of CO_2 is split (Figure 2.4). As shown in Figure 4.4, this exothermic release can supply over 95% of the energy required to heat and vaporize the Zn and H_2O or CO_2 reactants. When this energy is recuperated, the cycle efficiency is independent of the oxidation temperature and is 38% for water splitting and 41% for carbon dioxide splitting. The kinetic advantage of the heterogeneous oxidation of Zn(g) can therefore be realized without reducing cycle efficiency. Perfect heat recuperation is, of course, not possible in practice, but if efficient energy exchange could be achieved, the thermodynamic penalty associated with supplying the sensible and latent energies of the Zn and H_2O or CO_2 reactants would be mitigated, and the efficiency would lie somewhere between the two curves in Figure 4.2.

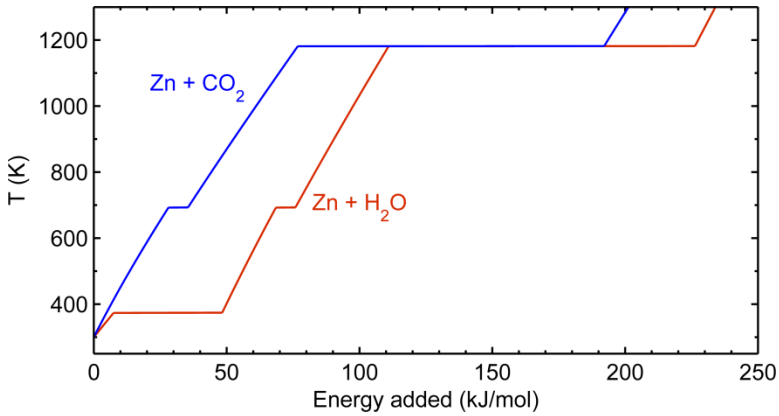

Figure 4.4 Temperature of the Zn/H_2O (red line) and Zn/CO_2 (blue line) reactant streams as energy is added to the streams in the case of complete conversion of zinc (α=1). At an oxidation temperature of 1185 K, 221 kJ/mol is released when H_2O is split and 188 kJ/mol is released when CO_2 is split.

Even without heat recuperation, there is a thermodynamic advantage associated with utilizing the heterogeneous oxidation of Zn(g) for H_2O- and CO_2- splitting since it permits complete zinc conversion in short reaction times (see Chapter 3). Consider the cycle efficiency as a function of the conversion achieved in the oxidizer, Figure 4.5, for oxidation temperatures of 300, 700, and 1185 K and for β = 0.2, 0.6, and 1. The temperature range encompasses the latent heat of water vaporization at 700 K and the latent heats of water and zinc vaporization at 1185 K. As zinc is less effectively recovered from the quencher ($\beta \to 0$), the thermodynamic advantage of utilizing low oxidation temperatures is lessened. For example, if only 20% of the zinc is yielded from the quencher ($\beta = 0.2$), the difference in the cycle efficiency for oxidation temperatures of 300 K and 1185 K is less than 1% for all values of α. Thus, if the water or carbon dioxide splitting cycles are constrained to incomplete zinc yields in the quencher upstream of the oxidizer, Figure 4.5 shows that the thermodynamic penalty of an elevated oxidation temperature is small relative to the thermodynamic gain of achieving larger conversions of zinc, which the heterogeneous oxidation of zinc vapor permits.

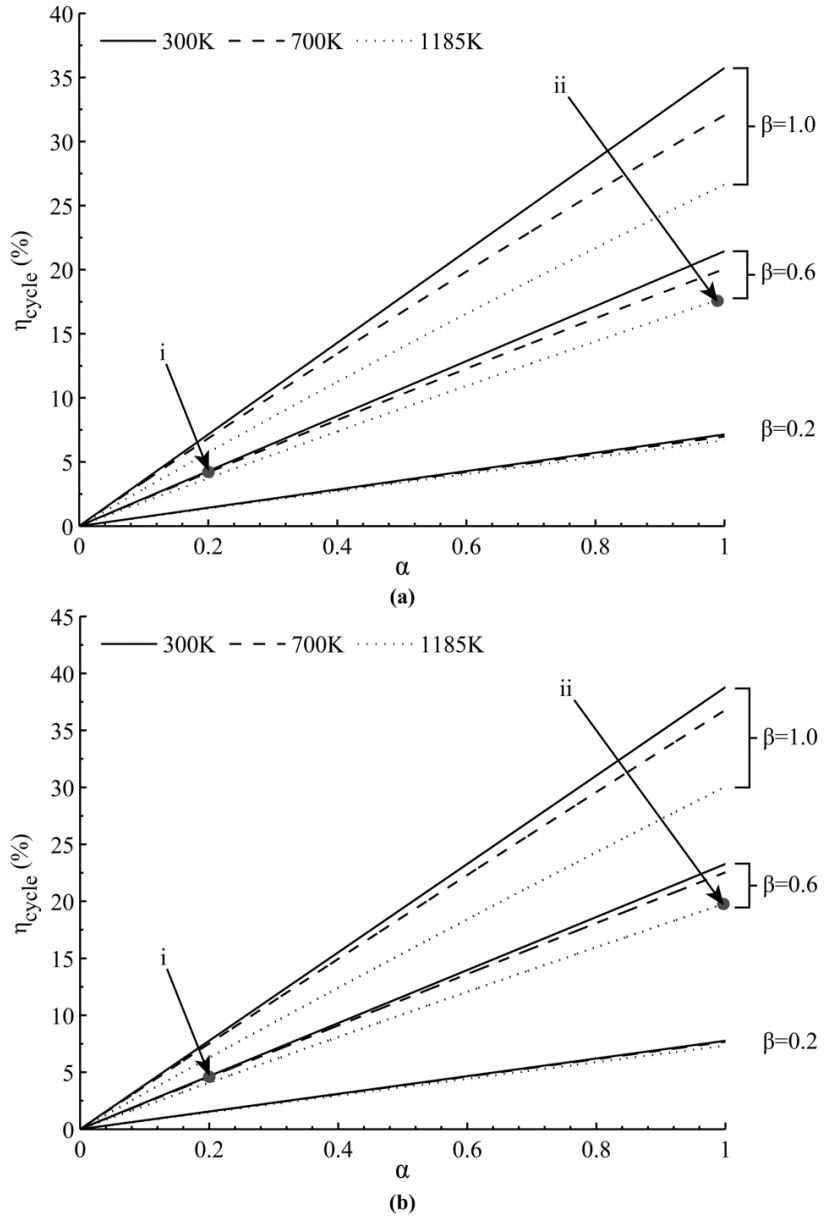

Figure 4.5 Impact of zinc conversion on cycle efficiency for three oxidation temperatures and three zinc yields from the solar reactor quench in the (a) H_2O- and (b) CO_2-splitting cycles. T_{solar}=2300 K, C=10,000, and no heat recuperation. Point (i) represents the efficiency achieved via the zinc aerosol oxidation path, and point (ii) represents the efficiency of the heterogeneous oxidation of Zn(g) path.

To demonstrate this thermodynamic advantage, consider the data available in the literature on the quencher and on the zinc aerosol reaction path in conjunction with the data on the heterogeneous oxidation of Zn(g) in Chapter 3. The quencher designed for a prototype scale ZnO thermal dissociation reactor achieved, on average, a 61% yield ($\beta = 0.61$) of Zn from the reduced ZnO [33]. Zinc aerosol reactors have achieved no more than 20% conversion of the zinc aerosol ($\alpha = 0.2$) with hydrolysis temperatures near 700 K [42, 54, 55]. The heterogeneous oxidation of Zn(g), however, was shown in Chapter 3 to achieve zinc conversions greater than 95% in short reaction times. The energy flows and process irreversibility for the water splitting cycle with $\beta = 0.6$, $\alpha = 1$, and $T_{\text{hydrolysis}} =$ 1185 K (case 1: heterogeneous oxidation of Zn(g) path) and $\beta = 0.6$, $\alpha = 0.2$, and $T_{\text{hydrolysis}} = 700$ K (case 2: zinc aerosol oxidation path) are shown in Table 4.1, and the resulting efficiency for both H_2O- and CO_2- splitting cycles are noted by the points (i) for the zinc aerosol path and by the points (ii) for the heterogeneous oxidation of Zn(g) path on Figure 4.5. Note that it is assumed that the aerosol is generated in a process that does not require the evaporation of Zn, e.g., via a fluidized bed feeder [42]. Even though Zn(g) must be generated to achieve near complete zinc conversion via the heterogeneous oxidation path, the cycle efficiency is improved to 16% for water splitting and 20% for carbon dioxide splitting over the ~4% cycle efficiency in the aerosol oxidation path. In the context of the constraints of the quencher upstream of the oxidizer, the kinetic advantages of the heterogeneous oxidation of Zn(g) thus outweigh the thermodynamic disadvantage associated with generating the zinc vapor. This conclusion can also be drawn by observation of the process irreversibility (Table 4.1). The irreversibility associated with heating the zinc/water reactants to the oxidation temperature is 0.2226 kW K^{-1} larger in case 1 when zinc vapor is generated than in case 2, but the total irreversibility of case 2 is 12.3771 kW K^{-1} larger than case 1. The irreversibility associated with incomplete conversion is thus larger than the irreversibility associated with generating zinc vapor.

Table 4.1 Energy flows and process irreversibility for the production of 1 mol s^{-1} of H_2 in the H_2O-splitting cycle with and the hydrolysis temperature and zinc conversion corresponding to the heterogeneous Zn(g) reaction path (case 1) and the Zn aerosol reaction path (case 2)

		Case 1: α=1, $T_{hydrolysis}$=1185 K		Case 2: α=0.2, $T_{hydrolysis}$=700 K	
Process	Energy flow	Rate of energy transfer (kW)	Irreversibility (kW/K)	Rate of energy transfer (kW)	Irreversibility (kW/K)
Solar reactor	$\dot{Q}_{solar}$	1087	0.5883	5434	2.9414
	$\dot{Q}_{loss}$	-173		-862	
Quencher	$\dot{Q}_{quencher}$	-564	1.4941	-2819	7.4703
Oxidizer	$\dot{Q}_{sensible/latent}$	227	0.9345	150	0.7119
	$\dot{Q}_{oxidation}$	-291		-214	
Unreacted Zn→ZnO	$\dot{Q}_{Zn\rightarrow ZnO}$	0	0	-1402	4.2704
Fuel Cell	$\dot{Q}_{fuel\ cell}$	-49	0	-49	0
	$\dot{W}_{fuel\ cell}$	-237		-237	
		$\sum = 0$	$\sum = 3.0169$	$\sum = 0$	$\sum = 15.3940$
Cycle efficiency		$\eta_{cycle} = 16\%$		$\eta_{cycle} = 4\%$	

Irreversibility increases in case 2 in the solar reactor and quencher because of the additional ZnO/Zn and H_2O/CO_2 required to produce a unit of H_2/CO, and the second largest irreversibility in the cycle is directly associated with the unreacted zinc. Table 4.1 also shows the importance of improving the zinc yield from the quencher. In both cycles, the quencher is the most irreversible process.

Finally, the data in Table 4.1 validate the energy and entropy balances on the processes in the water and carbon dioxide splitting cycles. When these balances are coupled, the first and second laws of thermodynamics applied to the cycle are satisfied. To satisfy the first law, all energy flows in and out of the cycle offset so that there is no storage of energy:

$$0 = \dot{E}_{\text{out}} - \dot{E}_{\text{in}} = \sum \dot{Q} + \dot{W}_{\text{fuel cell}} \tag{4.8}$$

To satisfy the second law, the sum of the work generated by the cycle and the potential for work lost due to the process irreversibility must equal the work generated by a Carnot heat engine operating between the same high and low temperature thermal reservoir.

$$\eta = \frac{\left|\dot{W}_{\text{fuel cell}}\right| + (300\ \text{K}) \sum \dot{S}_{\text{gen}}}{\sum \dot{Q}_{\text{in}}} = \eta_{\text{Carnot}} \tag{4.9}$$

4.3 Summary

A parametric thermodynamic analysis is presented that shows the benefit of utilizing the heterogeneous oxidation of Zn(g) in the two-step Zn/ZnO H_2O- and CO_2- splitting cycles. Even without heat recuperation to minimize the energy that must be supplied to generate zinc vapor, achieving complete conversion of zinc to zinc oxide via the heterogeneous oxidation of Zn(g) raises the water and carbon dioxide splitting efficiency from ~6% (achieved to date with reaction times on the order of a minute) to 27% and 31%, respectively. With heat recuperation, 95% of the energy needed to generate zinc

vapor can be supplied by the energy released from oxidation. In this case, the theoretical maximum cycle efficiency is 38% for water splitting and 41% for carbon dioxide splitting.

Part II: The Oxidation of Porous Ceria

5 Thermochemical Cycling of Ceria for Fuel Production

In this chapter, the thermochemical cycling of ceria is reviewed. The non-stoichiometric thermodynamics of ceria is presented to elucidate the roles that temperature and oxygen partial pressure play in determining oxygen vacancy formation (or, equivalently, non-stoichiometry). The parameter δ quantifies the ceria non-stoichiometry, indicating the moles of oxygen removed from the ceria per mole of the ceria. The thermodynamics of oxygen removal from ceria provides the foundation for the thermochemical production of H_2 and CO. The kinetics of ceria oxidation by H_2O and CO_2 is then discussed. Prior work suggests that specific surface area and porosity are critical for achieving rapid rates of H_2 and CO production, and also shed light on the challenge of maintaining porosity and surface area at the high temperatures required for solar thermochemical cycling.

5.1 The Thermodynamics of Non-stoichiometric CeO_2

The solid-state thermodynamics of ceria relates temperature and O_2 partial pressure to the ceria non-stoichiometry, δ, and bounds the amount of fuel that can be produced in a single thermochemical cycle. Direct measurements of the ceria non-stoichiometry have been completed using thermogravimetry, coulometric titration, and electrical conductivity techniques for temperatures between 823 and 1773 K and for oxygen partial pressures between 10^{-2} and 10^{-28} atm, corresponding to $10^{-4} \leq \delta \leq 0.3$. These studies are reviewed in Ref. [116]. The data of Panlener *et al.* [117] are shown in Figure 5.1 for temperatures between 1000 and 2000 K. Details of the extrapolation of the data to T > 1773 K are

provided in Appendix E. When ceria is partially reduced ($\delta > 0$), Ce^{4+} ions transition to Ce^{3+} defects, which have one negative charge relative to the normal lattice. To maintain electroneutrality, oxygen vacancies, with two positive charges relative to the normal lattice, are formed in a 1:2 ratio with Ce^{3+} defects [116]. Concurrent with the formation of an oxygen vacancy, gaseous O_2 is released from the solid.

The partial reduction of ceria is the first step of solar thermochemical H_2 and CO production from H_2O and CO_2:

$$CeO_2(s) \rightarrow CeO_{2-\delta}(s) + \frac{\delta}{2} O_2(g) \tag{5.1}$$

Typically this step is completed in a low oxygen partial pressure atmosphere ($p_{O_2} \leq 10^{-2}$ atm) by heating ceria to temperatures above 1500 K and flowing an inert sweep gas over the ceria to maintain a low oxygen partial pressure. In a solar cycle, the sole source of heat is provided by concentrated solar radiation. The reduction for $p_{O_2}=10^{-5}$ atm and T = 1800 K is indicated in Figure 5.1 by the solid arrow. At this temperature and partial pressure of oxygen, the non-stoichiometry at equilibrium is $\delta = 0.07$, with 0.035 moles of O_2 released per mole of CeO_2 (8 mL O_2/gram CeO_2). To produce H_2 (or CO), the ceria is quickly cooled (horizontal dashed line in Figure 5.1), perturbing its equilibrium, and then exposed to the H_2O (or CO_2) feedstock:

$$\delta H_2O + CeO_{2-\delta} \rightarrow CeO_2 + \delta H_2 \tag{5.2}$$

To restore equilibrium at constant temperature, the ceria strips oxygen atoms from the H_2O to fill its oxygen vacancies and revert Ce^{3+} defects to Ce^{4+}, indicated by the curved, dashed arrow in Figure 5.1. The net effect of reactions (5.1) and (5.2) is the desired splitting of H_2O (or CO_2). The maximum fuel production is given by the non-stoichiometry change in the ceria between the reduction and oxidation steps. By adding excess H_2O or CO_2, e.g., continuously flowing H_2O or CO_2 over ceria, complete reoxidation is

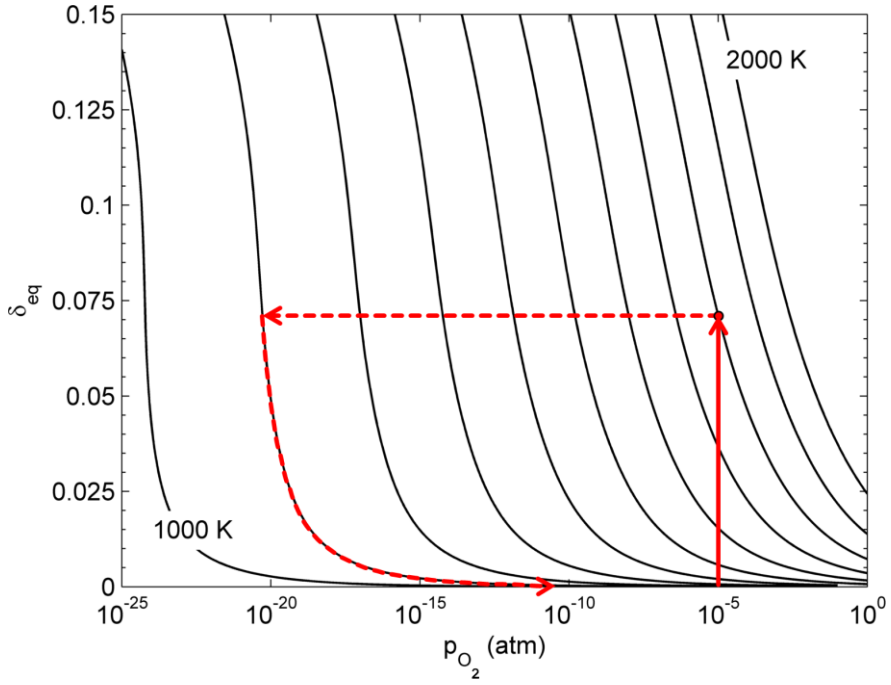

Figure 5.1 Ceria non-stoichiometry as a function oxygen partial pressure for temperatures between 1000 and 2000 K in 100 K increments [117]. The arrows overlaid on the graph demonstrate a single thermochemical cycle. O_2 is released as oxygen vacancies are formed in the ceria upon heating to 1800 K with an oxygen partial pressure of 10^{-5} atm (solid arrow). Cooling the reduced ceria (horizontal arrow) perturbs the equilibrium. To reestablish equilibrium, the ceria strips the O molecules from H_2O or CO_2 to refill its oxygen vacancies at 1100 K (curved arrow), thus producing H_2 or CO.

thermodynamically predicted for T < 1500 K, even for low concentrations of H_2O/CO_2. In this case, the maximum fuel production is equal to the non-stoichiometry achieved during reduction. Continuing with the example shown in Figure 5.1, $\delta = 0.07$, yielding 0.07 moles of H_2 or CO per mol of CeO_2 (16 mL per gram of CeO_2).

Using the non-stoichiometric thermodynamics of ceria, it is possible to calculate the thermal efficiency of the production of H_2 or CO in the solar thermochemical cycle. This analysis has been completed by Lapp *et al.* [37]. Thermal efficiency is defined as the energy in the H_2 or CO relative to the solar energy required for its production. In the case of H_2 production,

$$\eta_{\text{th}} = \frac{\dot{n}_{\text{H}_2}(\overline{\text{HHV}})}{\dot{Q}_{\text{solar}}} \tag{5.3}$$

where $\overline{\text{HHV}}$ is the higher heating value of H_2. The amount of H_2 and CO produced, neglecting chemical kinetics, is determined by the partial pressure of oxygen and the temperature during the reduction of ceria[5]. Concentrated solar radiation supplies the sensible energy to heat the ceria and the low oxygen partial pressure sweeping gas, and also supplies the process heat to form non-stoichiometry at the high reduction temperature. For the partial reduction of ceria, the energy required to form oxygen vacancies is small compared to the sensible energy required for solid and gas heating. Consequently, if not recuperated, the large fraction of sensible energy input is lost, and the thermal efficiency of fuel production is limited to 6% regardless of the extent of reduction of the ceria. The lack of recuperation led, in part, to the low 0.4% thermal efficiency of a ceria-based prototype reactor [72, 73]. Recuperation is thus a key ingredient for increasing the thermal efficiency in ceria or other non-stoichiometric oxide based thermochemical

[5] It is anticipated that conditions for oxidation ensure that the non-stoichiometry formed during reduction is fully utilized.

cycles. When ~50% of thermal energy is recovered from the reduced solid ceria and from hot product gases, thermal efficiencies in excess of 10% are possible [37].

The thermal efficiency can also be increased if the non-stoichiometric thermodynamics of the reactive oxide favors greater fuel production at lower temperatures and higher oxygen partial pressures [37]. Ongoing work seeks to alter the non-stoichiometric behavior of ceria by adding cationic dopants [35, 118-125]. For example, the addition of Zr^{4+}, an undersized cation that distorts the cubic fluorite lattice of ceria and induces defect formation, is known to increase the degree of reduction by up to $\Delta\delta$~0.1 at 973 K in strongly reducing environments ($p_{O_2} < 10^{-10}$ atm) [126-128]. It also increases the degree of reduction in nominally pure Ar at 1773 K [121]. Even though the Zr^{4+} cations are chemically inactive, the increase in the reducibility of the cerium ions can compensate for the addition of inactive mass [124, 129]. Some dopants, such as Gd, Y, Sm, Ca, and Sr, lower the amount of H_2 and CO produced at chemical equilibrium [125].

A second benefit of doping ceria is that it typically improves the resistance of the solid to sintering [130, 131]. Sintering is a high temperature solid-state diffusion process that reduces overall surface area and increases solid features sizes, hindering the kinetics of reduction and oxidation [132]. Thus, despite slight reductions in equilibrium fuel production, doping could ultimately lead to more stable solid morphologies and faster, more efficient fuel production.

5.2 The Kinetics of H_2 and CO Production from Reduced Ceria

We now turn from the thermodynamics of fuel production to kinetics. Both the oxidation and reduction of ceria are heterogeneous, proceeding through gas-phase transport (including pore-scale diffusion), surface reaction, and diffusion of oxygen through the solid. Prior work on the oxidation of ceria suggests any of these steps could limit the overall

reaction rate depending on the characteristics of the reacting system. In porous ceria, the surface step is the primary limiter of the overall reaction [35], as both the gas-phase transport and bulk diffusion processes are relatively rapid. Estimates of the characteristic rates of gas-phase diffusion and solid diffusion of oxygen support this observation, but also highlight the importance of mitigating sintering at the high temperatures required for thermochemical cycling. Sintering can lead to the collapse of porosity and unfavorable solid length scales where transport, rather than intrinsic surface chemistry, limits the overall oxidation kinetics [122, 123, 133].

5.2.1 Surface Reaction

Oxidation of ceria by H_2O or CO_2 involves the adsorption, conversion, and desorption of gaseous species from active sites on the ceria surface, presumably via a mechanism involving multiple chemisorbed reaction intermediates. The mechanistic details by which the H_2O and CO_2 are converted to H_2 and CO are unknown. What is known is that the sum of the surface reaction steps. The importance of the surface step is reported in studies that isolate the surface step for direct study [35, 36, 122] and imply its importance through steep drops in the rate of H_2 or CO production associated with losses in surface area [122].

Chueh and Haile [35] oxidized porous ceria cylindrical monoliths at 1000 to 1100 K in flows of both low (~2 mol%) and high concentration (~25 mol%) mixtures of H_2O and CO_2. The cylindrical monoliths measured 7 mm in diameter and 2–4 mm in thickness, weighed ~0.25 g, and were reported to be more than 65% porous. H_2 and CO production over the monoliths was complete in ~2 min at 1073 K in a 25 mol% H_2O environment. Furthermore, the ceria non-stoichiometry, which was initially $0.056 \leq \delta \leq 0.066$, was completely utilized for fuel production, yielding 9–12 mL g^{-1} of H_2. To elucidate the role of the surface reaction step on the overall kinetics, the oxidation of porous 15% samarium-doped ceria ($Ce_{0.85}Sm_{0.15}O_{1.925}$) impregnated with Rhodium was compared to the oxidation

of neat $Ce_{0.85}Sm_{0.15}O_{1.925}$. Rhodium is a noble metal known to catalyze surface reactions. At 1023 K in a flow with p_{H_2O}=0.023 atm, the Rh-impregnated material increased the rate of H_2 production threefold, indicating the rate-limiting nature of the surface step. It is important to note that while the Rh-impregnated material increased the rate of fuel production, the oxidation of porous ceria without a nobel metal catalyst is also facile (complete oxidation in 2–10 min).

Further evidence of the importance of the surface reaction step for ceria oxidation is garnered from kinetic analyses of H_2O- and CO_2-splitting over $Ce_{0.85}Sm_{0.15}O_{1.925}$ with a relatively low specific surface area of 0.2 m^2 g^{-1} [36]. $Ce_{0.85}Sm_{0.15}O_{1.925}$ was reduced to δ=0.05, and subsequently oxidized at 773–973 K in flows with H_2O and CO_2 partial pressures between 0.01 and 0.08 atm. By comparing the initial (i.e., when δ=0.05) rate of oxidation at T=673 K in flows with different concentrations of H_2O and CO_2, the apparent order of the oxidation with respect to H_2O and CO_2 was determined. For oxidation by H_2O, the order is 0.54, and for oxidation by CO_2, the order is 0.77. That the order of the reaction with respect to H_2O and CO_2 is not zero suggests that the oxidation is limited by surface processes. If the oxidation had been limited by the diffusion of oxygen in the solid, the kinetics would be relatively independent of the concentration of H_2O and CO_2 over the narrow range of the kinetic study.

In a thermogravimetric study of the reduction and oxidation of ceria-based oxides, surface kinetics best described the oxidation data prior to significant sample sintering [122, 123]. $Ce_{0.75}Zr_{0.25}O_2$ was prepared via wet chemistry methods yielding nanocrystalline solid powder with textural porosity. The ceria-zirconia mixed oxide powders were reduced by ramping to and dwelling at 1673 K for one hour (the gas atmosphere during reduction was not specified), and then were oxidized by CO_2 (50 vol%) for 35 minutes. Regression of the oxidation data to a solid-state surface kinetic model provided the best fit of the oxidation data. After the loss of surface area and associated grain growth (the cycled materials have

crystallites on the order of tens of µm), solid diffusion kinetic models provided a better fit to the oxidation data.

The strong influence that the surface reaction has on the overall kinetics of ceria oxidation suggests that solid morphology will play an important role in the solar thermochemical production of H_2 and CO. One of the goals of the present study is to explore the role of ceria morphology on the kinetics of oxidation, considering engineered macroporous architectures. Further details can be found in Chapter 6.

5.2.2 Diffusion of Atomic Oxygen in Solid Ceria

The rate at which oxygen diffuses in (oxidation) or out (reduction) of ceria depends on the magnitude of the chemical potential gradient of oxygen within the ceria and the chemical diffusion coefficient, describing the coupled migration of oxygen vacancies and electrons that ultimately lead to the net flux of oxygen atoms. If the chemical potential of defects in ceria follows that of an ideal solution,

$$\mu_i = \mu_i^o + k_B T \ln(c_i)\,, \tag{5.4}$$

then the chemical diffusion coefficient can be estimated from the diffusivities of the oxygen vacancies and electrons [134]:

$$\widetilde{D} \cong \frac{3\mathfrak{D}_{\text{vacancy}}\mathfrak{D}_{\text{electron}}}{2\mathfrak{D}_{\text{vacancy}} + \mathfrak{D}_{\text{electron}}} \tag{5.5}$$

The vacancy and electron diffusivities are related, in turn, to their mobilities, $\tilde{\mu}_i$, through the Nernst-Einstein relation,

$$\mathfrak{D}_i = \frac{(k_B T)\tilde{\mu}_i}{e z_i} \tag{5.6}$$

where z_i denotes the number of charges (1 for an electron and 2 for a vacancy), e is the fundamental unit of charge (1.60218×10^{-19} C), and k_B is the Boltzmann constant. The

electron mobility has been measured for nominally pure ceria for temperatures between 473 and 1373 K and for non-stoichiometry between 0.008 and 0.25 [135]. The vacancy, or ion, mobility of ceria is not directly available, but for a wide number of ceria-based mixed oxides, ion mobility is generally an order of magnitude less than electron mobility. For example, in $Ce_{0.85}Sm_{0.15}O_{1.925}$ at 773 to 973 K, the ion mobility is 40 to 10 times less than the electron mobility [134], and in $Ce_{0.9}Gd_{0.1}O_{1.95}$ at 873 to 1273 K, the ion mobility is 4 to 10 times less than the electron mobility [136]. For the purposes of estimating the relative importance of atomic oxygen diffusion during the oxidation or reduction of ceria, the ion mobility is thus assumed to be 10 times less than the electron mobility.

Accounting for the temperature and non-stoichiometry dependencies of the electron mobility as measured by Tuller and Nowick [135], the chemical diffusion coefficient for ceria was estimated from equations (5.5) and (5.6). The results are summarized in Table 5.1. The chemical diffusion coefficient decreases as ceria is reduced for all temperatures, consistent with measurements for doped ceria [35, 134]. At 1273 K, the chemical diffusion coefficient decreases by a factor for 2 from 1.2×10^{-4} to 6.1×10^{-5} cm^2 s^{-1} when the ceria non-stoichiometry increases from 0.008 to 0.09. For a fixed non-stoichiometry, the chemical diffusion coefficient monotonically increases with temperature, from, for example, 2.27×10^{-5} cm^2 s^{-1} at 873 K to 1.21×10^{-4} cm^2 s^{-1} at 1273 K at δ=0.008. Consequently, it is safe to conclude that if solid diffusion of oxygen is rapid during the oxidation of ceria at 1100–1300 K, it will also be rapid for reduction at higher temperatures.

Using the chemical diffusion coefficient, the time required to oxidize ceria assuming that diffusion of atomic oxygen is rate-limiting can be estimated. For a one-dimensional

Table 5.1 The electron mobility reported in Ref. [135] and the chemical diffusion coefficient estimated for reduced ceria for temperatures between 873 and 1273 K and for non-stoichiometry between 0.008 and 0.09.

	δ=0.008		δ=0.090	
T (K)	$\tilde{\mu}_{\text{electron}}$ ($cm^2\ V^{-1}\ s^{-1}$)	$\widetilde{D}$ ($cm^2\ s^{-1}$)	$\tilde{\mu}_{\text{electron}}$ ($cm^2\ V^{-1}\ s^{-1}$)	$\widetilde{D}$ ($cm^2\ s^{-1}$)
873	2.21×10^{-3}	2.27×10^{-5}	1.02×10^{-3}	1.05×10^{-5}
973	3.43×10^{-3}	3.92×10^{-5}	1.63×10^{-3}	1.87×10^{-5}
1073	4.85×10^{-3}	6.11×10^{-5}	2.36×10^{-3}	2.98×10^{-5}
1173	6.41×10^{-3}	8.84×10^{-5}	3.18×10^{-3}	4.38×10^{-5}
1273	8.06×10^{-3}	1.21×10^{-4}	4.06×10^{-3}	6.07×10^{-5}

Cartesian geometry (i.e., a plane wall), the continuity of oxygen atoms is:

$$\frac{\partial c_0}{\partial t} = \widetilde{D}\frac{\partial^2 c_0}{\partial x^2}, \tag{5.7}$$

where the chemical diffusion coefficient is taken to be spatially and temporally constant for simplification. The analytical solution to equation (5.7) is known, and is developed in standard heat and mass transfer textbooks, e.g. Ref. [137]. The analytical solution is also available for cylindrical and spherical coordinate systems. Using the analytical solution, the time required to oxidize ceria to a desired extent can be calculated for rectangular, cylindrical, and spherical shaped ceria particles. The extent of oxidation is defined as the ratio of the total atomic oxygen transferred into or out of the ceria to the maximum amount of oxygen that could be transferred at chemical equilibrium.

$$X(t) = \frac{-\int (c_0(x,t) - c_0^o)dV}{V\left(c_0^o - c_{0,\text{eq}}\right)} \tag{5.8}$$

where the integration is performed over the volume of the particle. In equation (5.8), c_0^o is the initial concentration and $c_{0,\text{eq}}$ is the concentration at chemical equilibrium at the surface of the particle. Using the lowest value for $\widetilde{D}$ at 1073 K as representative of the behavior for all temperatures and non-stoichiometries, the time required to reach an

oxidation extent of 95% was calculated over ceria length scales from 1 nm to 1 mm in the three coordinate systems. The results are shown in Figure 5.2. Oxygen diffusion in ceria is remarkably fast for nm- and µm-length scales. For ceria geometries on the order of hundreds of nanometers, oxidation is over 95% complete in less than 1 ms; at ~100 µm, oxidation is over 95% complete in less than 10 s.

The key feature of the characteristic diffusion time is that it increases exponentially as the length scale increases. At the mm-length scale, the time predicted to reach 95% extent of reaction increases from seconds to minutes and at 1 cm, the characteristic diffusion time scales on quarters of hours. The dramatic increase in diffusion time with mm- to cm-length scales, which are still small relative to the length scales anticipated for prototype ceria thermochemical reactors, point to the need for porosity in the reactive ceria substrate. Porosity permits small solid diffusion lengths in a ceria material with much larger

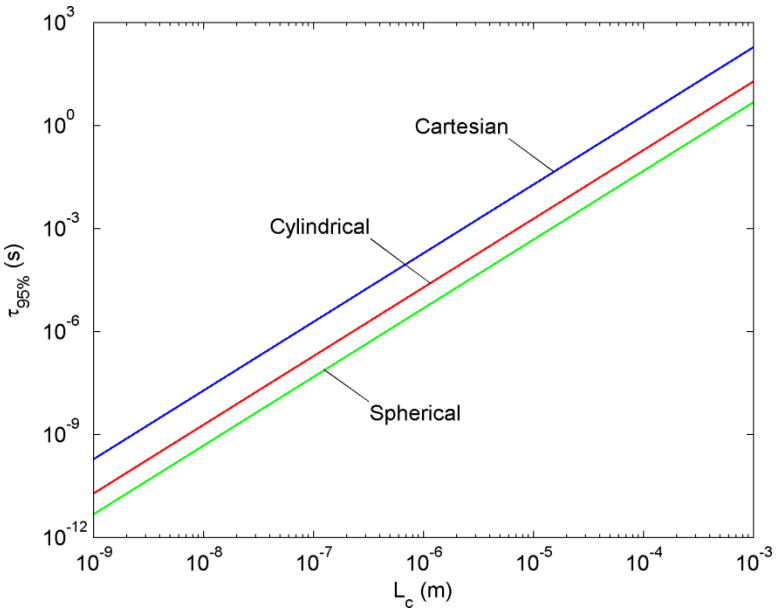

Figure 5.2 The time required to oxidize 95% of ceria with characteristic length L_c assuming that the diffusion of oxygen in the lattice is rate-limiting at 1073 K in a rectangular, cylindrical, and spherical particle assuming a fixed chemical diffusion coefficient.

macroscopic dimensions, allowing for rapid solid diffusion of oxygen in a reactive substrate with sufficient volume (and hence mass) to produce industrially relevant amounts of fuel. The estimates of the diffusion-limited kinetics of H_2 and CO production presented here suggest that for kinetics faster than minutes, diffusion lengths should be less than ~500 µm.

The estimates of the solid diffusion of oxygen lend further credence to the hypothesis that the surface reaction step is the primary rate-limiter for the production of H_2 and CO in porous ceria. Recall that in prior work, H_2 and CO production occurred over the course of minutes in the porous ceria structures [35, 36]. Given that the solid features sizes in porous structures were likely on the order of tens of µm, for which the characteristic diffusion time is on the order of ms, it is unlikely that the diffusion of oxygen in the solid impeded the oxidation. Other estimates of the rates of oxygen diffusion corroborate this conclusion [35, 132].

5.2.3 Gas-phase Transport

A discussion of gas-phase transport, including diffusion through the pores of ceria (intraparticle diffusion), is missing from the literature. Gas-phase transport is, however, an important consideration to ensure that the non-stoichiometry formed during reduction is effectively utilized for fuel production throughout the porous volume. Analysis of data available in the literature and the data in the present study (presented in Chapter 6) shows that conditions exist in which gas-phase transport slows the overall rate of H_2 or CO production. Care must be taken when synthesizing the reactive ceria substrate to ensure that gas-phase transport effects are minimized, especially when it is desired to measure the rate of the intrinsic surface reaction.

Intraparticle diffusion, in the absence of a kinetic expression, is evaluated from experimental data using a dimensionless parameter called the Wagner modulus. The

Wagner modulus provides a measure of the effectiveness with which the porous particle volume is utilized for the heterogeneous reaction. It can be thought of as the ratio of the time scale for intraparticle diffusion to that of the chemical reaction. Details of its development can be found in Ref. [70]. When the Wagner modulus is small (<0.15), diffusion is fast relative to the chemical reaction and the reactants fully penetrate the volume of the particle. When the Wagner modulus is large (>4), the intraparticle diffusion is slower than the chemical reaction and the innermost surfaces of the porous particle are starved for reactant. The Wagner modulus is calculated based on an appropriate length scale for the particle, the effective diffusion coefficient for gas through the pores, and the measured reaction rate:

$$M_W = \left(\frac{L^2}{\mathcal{D}_e c_i}\right)(r''') = \frac{\tau_{\text{diffusion}}}{\tau_{\text{reaction}}} \tag{5.9}$$

where i refers to either H_2O or CO_2 depending on the reaction under consideration. The effective diffusion coefficient, $\mathcal{D}_e$, accounts for the porosity of the particle and the tortuosity of its pores.

$$\mathcal{D}_e = \frac{\phi}{\bar{\tau}}\mathcal{D}_{\text{pore}} \tag{5.10}$$

Tortuosity effectively increases the length over which a gas molecule must travel to reach the inner surfaces of a particle, and porosity accounts for the fluid area available for molecular flux across the particle. The nature of gas diffusion in a pore is highly dependent on the pore diameter. For small pores (less than 100 nm at atmospheric pressure), molecule-wall interactions occur more frequently than molecule-molecule interactions, and the diffusivity of the gas is governed by Knudsen theory. In larger pores, the molecular diffusivity applies. Advection of reacting gas through the pores is not anticipated. All of the transport is assumed to be by the diffusion mechanism.

Using the data from Ref. [35] reviewed in section 5.2.1, and the data for 3DOM CeO_2 of the present study (see section 6.3.2), the relative importance of intraparticle diffusion to the oxidation of porous ceria is evaluated. Table 5.2 lists the length scale for intraparticle transport, the effective diffusion coefficient, and the corresponding values of the Wagner modulus for the two studies. In the present study, particles of various shapes with a porosity of 72% are sieved to diameters between 180 and 840 μm, and oxidized at 1150 K in a 25% CO_2 gas flow. The diameters of the pores are on the order of a few 100 nanometers. For both the prior and present study, the tortuosity is unknown, and thus assumed to take on a value of 4 per the recommendation in Ref. [70]. Quasi-steady oxidation of ceria is assumed, and the maximum reaction rate observed in the transient oxidation of the ceria systems is considered as a limiting case.

In the porous cylindrical monolith of the previous study [35], the Wagner modulus is larger than 0.15, but less than 4, indicating that the overall reaction is influenced by both intraparticle diffusion and the intrinsic surface reaction. Had the conditions for pore diffusion been more favorable, the overall rate of the reaction would have increased due to the more effective utilization of the inner porosity of the particle. This result shows that intraparticle diffusion can slow the rate of the oxidation of ceria if the porous ceria particle or monolith is too large.

The present study shows that the most effective way to eliminate intraparticle diffusion effects is to reduce the dimensions of the particle, i.e., by mechanical crushing. In smaller particles, the Wagner modulus decreases well-below 0.15, and all of the inner surfaces in the particles are bathed with reactant. In this case, the overall reaction rate is limited by the intrinsic surface kinetics. Reactive porous substrates for fuel production should be designed to avoid intraparticle diffusion effects so that the facile kinetics of the surface step can be taken advantage of.

Table 5.2 Table of values for analyzing the importance of intraparticle diffusion in the oxidation of ceria

	Chueh and Haile [35]	**This work (section 6.3.2)**
Particle geometry	Cylindrical CeO_2 monolith	3DOM CeO_2
Particle dimensions	R = 3.5 mm, 2-4 mm long	$r_p \leq 420$ μm
Effective length scale, L	$L = R/2$	$L = r_p/3$
Porosity	65%	72%
Pore diameter	1–20 μm	300–500 nm
Initial non-stoichiometry	0.091	0.007
Oxidizer Concentration, c_i	2.95 mol m^{-3}	2.73 mol m^{-3}
Temperature	1073 K	1150 K
Effective diffusion coefficient, $\mathcal{D}_e$	4.7×10^{-5} m^2 s^{-1}	$1.0–3.2\times10^{-5}$ m^2 s^{-1}
Measured reaction rate, r'''	22.2 mol solid-m^{-3} s^{-1}	10.3 mol solid-m^{-3} s^{-1}
Wagner modulus, M_W	0.49	7.4×10^{-3}

5.2.4 The Adverse Kinetic Effects of Sintering

Numerous studies cite sintering as the cause of observed drops in the rate of H_2 and CO production over ceria and ceria-based mixed oxides [35, 121-123, 133]. Ceria-zirconia mixed oxides cast into 2.2 g, 50% porosity disks were reduced at 1673 K in inert gas for several hours, and subsequently oxidized by both H_2O and CO_2 at 1373 K [133]. For $Ce_{0.25}Zr_{0.75}O_2$, H_2 and CO was produced over the course of 200 to 300 min, significantly slower than the rate of H_2 and CO production of the ceria and ceria-samaria mixed oxide in Refs. [35, 36, 72] (presumably due to the unfavorably high concentration of Zr^{4+}). The authors report that higher ceria content improved the initial rate of fuel production, but also increased the extent sintering, which collapsed the porosity and significantly reduced the oxidation kinetics (although data was not provided) [133]. In nanocrystalline ceria-zirconia mixed oxide powders, sintering correlated to drops in CO_2-splitting reactivity. Prior to loss of surface area, the oxidation rate was primarily limited by surface processes, but with sintering and grain growth, length scales for solid diffusion became unfavorably large such that diffusion of oxygen limited the rate of H_2 and CO production.

5.3 Summary

The thermodynamics of non-stoichiometric ceria are such that it releases oxygen when heated to high temperature in a low oxygen partial pressure environment, and rapidly takes up oxygen at a lower temperature from H_2O or CO_2 to refill its vacancies and produce H_2 or CO. It has a high melting point of ~2800 K and is capable of changes in non-stoichiometry (δ~0.25) without loss of activity due to restructuring of the solid lattice [138]. Product gases are separated intrinsically from ceria because it remains solid during thermochemical cycling. An energy balance that incorporates the non-stoichiometric thermodynamics of ceria shows that heat recuperation from the high temperature reduced ceria and hot product gases is mandatory for achieving a thermal efficiency of fuel production greater than 10%[37]. At the same time, thermal efficiency can be increased if the ceria produces more fuel at lower temperatures and higher oxygen partial pressures.

The global kinetics of ceria reduction and oxidation involve serial steps by which reactants (H_2O/CO_2) are transported through porosity, if present, in the ceria to an active oxidation site on the gas-solid interface. There the reactant is adsorbed and converted to products (H_2/CO), which desorb and are transported away from the ceria. Concurrently, atomic oxygen must diffuse into the ceria to occupy an available oxygen vacancy.

Prior work has only just begun to explore the relative importance of the individual reaction steps. The preliminary evidence suggests that for porous ceria, the surface reaction step is rate-limiting. For example, when porous ceria-samaria mixed oxide was decorated with Rh, a nobel metal catalyst, it produced H_2 three times faster than neat oxide. There are conditions, however, for which solid diffusion of oxygen or intraparticle diffusion of H_2O/CO_2 limit the overall rate of ceria oxidation. The former becomes rate-limiting when atomic oxygen diffusion lengths are greater than ~0.5 mm. The latter becomes rate-limiting if the porous ceria particle has length scales larger than ~1 cm. Both

diffusion limitations can be avoided with the careful design of the porous ceria reactive substrate. The challenge becomes maintaining favorable solid feature sizes and surface area at the high temperatures required for thermochemical cycling which can lead to extensive sintering. Loss of reactivity correlates with loss of surface area and grain growth [122, 133].

In summary, the literature points to the importance of porosity and morphology for achieving rapid H_2 and CO production rates. Yet, only a limited number of ceria morphologies have been considered in the literature: the monoliths of Refs. [35, 36, 72, 133], nanocrystalline powders [120-123], and ceria felt [73]. And only the porous monoliths of Refs. [35, 36] have retained an open porous network during thermochemical cycling. An in-depth study that considers ceria architectures engineered to possess and retain high specific surface area with an open and interconnected porosity is not only warranted, but critical for ensuring that reactions are fast enough to produce the maximum fuel thermodynamically possible.

6 The Effects of Morphology on the Oxidation of Ceria

Ceria offers a distinct advantage for solar thermochemical fuel production. It is able to release and absorb lattice-bound oxygen while retaining a solid and chemically active cubic crystalline phase. Remaining in a solid phase during thermochemical cycling avoids the complications that can arise from solid-to-liquid and solid-to-gas phase transitions, such as recrystalization and extensive grain growth upon melting or recombination of gas products.

An important pathway for increasing the efficiency of thermochemical fuel production in the $CeO_2/CeO_{2-\delta}$ cycle is enhancement of the kinetics of the gas-solid reactions. As discussed in Chapter 5, prior research has shown that the chemical processes that occur at the surface of ceria, where oxygen is stripped from H_2O or CO_2 and incorporated into the solid, strongly influence the overall kinetics. Utilizing ceria with high specific surface area that is readily accessible to the gaseous reactants thus promises to increase overall fuel production rates.

Accessible surface area may be increased by introducing an interconnected pore network in the ceria that contains nm- or µm-scale pores (see Refs. [74, 75] and the literature cited therein). To investigate this concept, the oxidation of ceria with templated porosity is compared with the oxidation of alternative porous ceria materials and ceria with limited porosity. Templated porosity can be generated in ceria (or other oxides) by infiltrating a liquid-phase ceria precursor into the void spaces of a sacrificial polymeric template. Of particular interest are colloidal crystal templates, which contain monodisperse polymeric spheres arranged in a face-centered cubic (fcc) orientation. This template can be used to synthesize three dimensionally ordered macroporous (3DOM) CeO_2 [75, 139]. The

3DOM CeO_2 is the inverse replica of the polymeric array of spheres, containing an fcc lattice of interconnected pores. 3DOM CeO_2 provides moderate specific surface area, sub-μm oxygen diffusion solid phase path lengths, and facilitates intraparticle gas phase mass transfer via the aforementioned interconnected pore network [140].

The 3DOM architecture is known to provide catalytic benefits in heterogeneous reaction systems [141-144]. For example, 3DOM CeO_2-ZrO_2 mixed oxides catalyze the combustion of diesel soot, lowering the requisite combustion ignition temperature by up to 50 K [142]. The enhanced catalytic activity is attributed to the interconnected pores of the 3DOM structure, which allows the soot particles and O_2 access to combustion sites throughout the volume of the catalyst particle. The improved catalysis of soot combustion, characterized by a 30 K decrease in the ignition temperature, is confirmed in a more recent study [143]. In another catalytic system, 3DOM $Ce_{0.6}Zr_{0.4}O_2$ increases the rate of the heterogeneous oxidation of propane by a factor of seven in a reactor with low space velocity, where intraparticle diffusion effects are pronounced [141]. These compelling observations provide impetus to extend the application of the 3DOM structure to H_2O and CO_2 splitting over reduced ceria.

In this chapter, I present experiments that show the importance of material architecture for rapidly producing H_2 and CO from ceria in the oxidation step of the two-step ceria thermochemical cycle. The ceria materials tested are described, including a brief description of how they were synthesized and the nature of their initial morphology. Two investigations to study the oxidation of ceria by H_2O and CO_2, in which the oxidation of 3DOM CeO_2 is compared with the oxidation of non-ordered macroporous ceria, aggregates of ceria nanoparticles, mesoporous ceria, and sintered ceria, are presented. In the first investigation, ceria is oxidized isothermally after chemical reduction with H_2. In the second investigation, ceria is thermochemically cycled, featuring reduction at high temperature in a low oxygen activity atmosphere and subsequent oxidation by CO_2 at a lower

temperature. The results of both investigations show that macroporous ceria with sub µm-scale feature sizes and moderate specific surface areas significantly increase the rate of H_2 and CO production over alternative ceria architectures. Portions of this chapter appear in Ref. [140]. The material has been reused with permission (see Appendix H).

6.1 Synthesis and Characterization of Ceria Materials

The porous materials studied to elucidate the effects of morphology on the oxidation of ceria were synthesized and characterized by Nicholas D. Petkovich, Stephen G. Rudisill, Daniel Boman, and Nicholas Hein, members of the research group of Professor Andreas Stein (Department of Chemistry, University of Minnesota). The details of their synthesis techniques are available in the literature [74, 139, 140], and they are summarized briefly in the following text.

Samples were characterized by the Stein research group before and after experiments with a combination of X-ray diffraction, scanning and transmission electron microscopy, and N_2 sorption. The full details regarding sample characterization can be found in Refs. [124, 140]. To summarize, powder X-ray diffraction (XRD) was performed on a Panalytical X'Pert powder diffractometer equipped with an X'Celerator detector; a JEOL 6500F scanning electron microscope was used to obtain scanning electron micrographs; and nitrogen sorption studies were conducted using a Quantachrome Autosorb iQ_2. Average grain sizes were determined from line broadening in the XRD patterns with the Scherrer equation. Specific surface areas were calculated by the Brunauer-Emmett-Teller (BET) method using the adsorption branches of the isotherms, and pore volumes were calculated by the Barrett−Joyner−Halenda (BJH) method. Knowledge of the morphological and textural characteristics of the samples, such as porosity, solid feature size, and specific surface area, is crucial for interpreting the measured fuel production kinetics.

Four porous ceria materials were synthesized: three-dimensionally ordered macroporous ceria (3DOM CeO_2), non-ordered macroporous ceria (NOM CeO_2), ceria featuring mesoporosity (DS CeO_2), and aggregates of nanoparticles obtained from the mechanical disassembly of 3DOM CeO_2 (D-3DOM CeO_2). The fifth material, a limited porosity, sintered granular ceria, was purchased from Alfa Aesar (99.9% purity). The meanings of the acronyms are related to the method of material synthesis, which are now explained, and are listed in the nomenclature for reference.

Three-dimensionally ordered macroporous ceria (3DOM CeO_2) was produced through a colloidal crystal templating route. A template was created from poly(methyl methacrylate) (PMMA) spheres with average diameters of ~500 nm via the gravity sedimentation of the spheres from an aqueous suspension [74, 124, 140]. During sedimentation, the spheres self-assembled into face-centered cubic close-packed arrays, forming the template. A precursor solution for ceria was wicked into the void spaces of the template by capillary action. The resulting composites (polymer sphere template and solidified precursor) were calcined in a tube furnace under static air by ramping to and dwelling at 583 and 723 K (additional details provided in Ref. [140]). Calcination removed the polymer spheres and crystallized the precursor, producing 3DOM CeO_2. A computer rendering and SEM image of freshly synthesized 3DOM CeO_2 is shown in Figure 6.1. The highly ordered network of macropores can be described as a series of solid "nodes" and "walls," formed where the ceria precursor infiltrated the void spaces between the spheres in the fcc template. The nodes are bimodal, with average sizes of 90 and 190 nm, and the walls, which connect the vertices of the nodes, have an average thickness of 50 nm at their narrowest point. The macropores are spherical voids with diameters of ~500 nm that connect to one another through circular "windows" with diameters of ~50 nm.

The 3DOM CeO_2 has a moderate BET specific surface area of 30–50 $m^2\ g^{-1}$, with slight differences attributed to the use of different ceria precursors in the templating process

[124]. Additionally, it is nanocrystalline, with an average grain size of 10 nm. Exposure to high temperature causes the 3DOM CeO_2 (and the other porous materials studied in the present work) to sinter, with the extent of the thermally-induced changes dependent on temperature. Held at 1100 K for 9 h, the specific surface area of 3DOM CeO_2 is reduced to 10 m^2 g^{-1}, but it remains nanocrystalline with an average grain size of 80 nm [140]. When exposed to temperatures above 1500 K during thermochemical cycling, the loss of specific surface area is more severe, and the specific surface area of the 3DOM CeO_2 drops to 4 m^2 g^{-1}. Grain growth is also more severe, growing to sizes above 100 nm. Furthermore, above 1500 K, the ordered pore network in 3DOM ceria is lost throughout most of the sample. However, the distinguishing feature of the 3DOM CeO_2 after thermochemical cycling is that it retains a disordered network of interconnected macropores. The walls between the pores are 150 nm thick, on average, with a standard deviation of 70 nm, and the sizes of the pores are on the same order as the walls.

Non-ordered macroporous ceria (NOM CeO_2) was also synthesized using a polymeric template. For NOM CeO_2, however, the template contained a disordered array of the PMMA spheres used to synthesize 3DOM CeO_2. This template morphology was obtained by continuously stirring the PMMA sphere suspension on a hot plate at 343 K. Water was rapidly evaporated, which prevented the PMMA spheres from self-assembling into an ordered lattice. The template of randomly positioned spheres was then infiltrated with the ceria precursor solution, thermally treated, and calcined following the same procedure as for 3DOM CeO_2. The NOM CeO_2 features a disordered network of macropores that contrasts the ordered nature of the macropores in 3DOM CeO_2 (Figure 6.1). The average thickness of the walls in NOM CeO_2 is 170 nm, and varies considerably due to the disordered nature of the PMMA template, with a standard deviation of 120 nm. The size of the pores is on the same order as the wall thickness.

Initially the NOM CeO_2 has a specific surface area of 47 m^2 g^{-1}. After exposure to

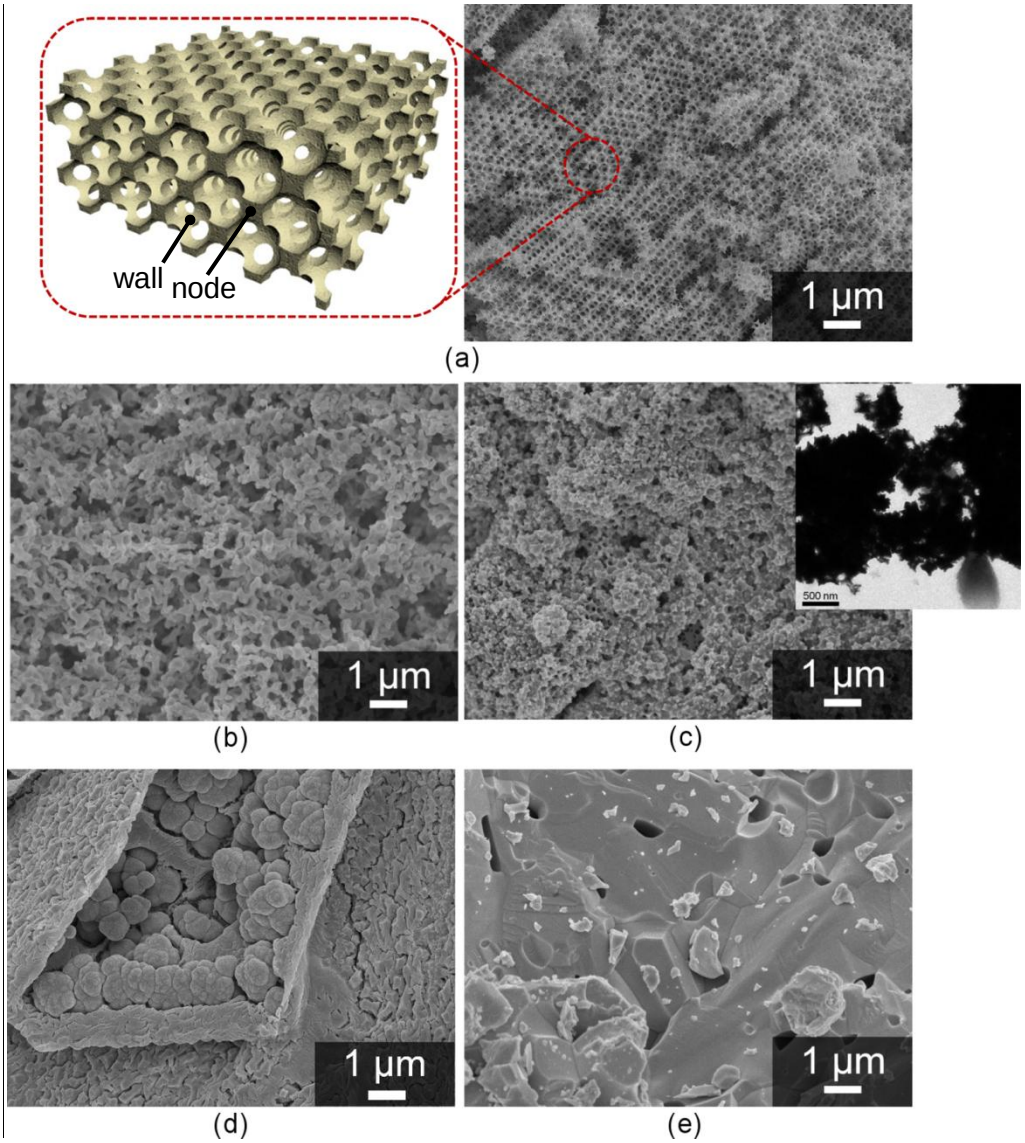

Figure 6.1 (a) Computer rendering and SEM image of 3DOM CeO_2 that both show the ordered network of macropores present in the 3DOM structure; (b) SEM image of NOM CeO_2 that shows that its pores are of similar size to 3DOM CeO_2, but lack order; (c) SEM image of D-3DOM CeO_2 showing that it is comprised of aggregates of nanoparticles that coat any remaining sub-3 μm 3DOM pieces; (d) SEM image of DS CeO_2 showing its foam-like structure, and (e) SEM image of the commercial CeO_2 showing its dense, polycrystalline, and sintered structure. Images courtesy of Nicholas Petkovich and Stephen Rudisill, Dept. of Chemistry, University of Minnesota.

temperatures above 1500 K, the specific surface area of NOM CeO_2 is 4 m^2 g^{-1}. The NOM sample does not undergo a drastic change in its pore structure during thermochemical cycling, however, retaining a random, interconnected network of macropores. Sintering caused the thickness of the NOM CeO_2 to increase from 150 nm to 340 nm, on average, with a large standard deviation of 160 nm. After exposure to temperatures above 1500 K, the walls of NOM CeO_2 were larger than the walls of the 3DOM CeO_2.

Some of the 3DOM CeO_2 was further processed to produce a mixture of ceria nanoparticles and sub-3 μm particles of 3DOM CeO_2 via disassembly of larger 3DOM CeO_2 particles, producing D-3DOM CeO_2. An aqueous slurry of 3DOM CeO_2 was placed in a sonicating bath for ~8 h to break 3DOM CeO_2 apart at the relatively thin walls between the nodes of the structure (Figure 6.1(a)). When the slurry stabilized, it was dried and crushed into a powder. Approximately 90% of the D-3DOM CeO_2 exists as closely-packed nanoparticles that are the remnants of the original 3DOM structure, as shown in Figure 6.1. The nanoparticles, shown close up in the inset of Figure 6.1(c), are the original nodes of the 3DOM structure, with protrusions that formed the walls of the original 3DOM structure. The nanoparticles have the same size as the nodes of the original 3DOM structure, 90 nm and 190 nm. The few remaining intact 3DOM CeO_2 particles in the D-3DOM CeO_2 sample are coated with the smaller disassembled fragments.

The D-3DOM CeO_2 sample initially contains more specific surface area than both the 3DOM and NOM CeO_2, 96 m^2 g^{-1}, a consequence of exposing additional solid surfaces when fracturing the 3DOM structure. Exposure to temperature above 1500 K causes the D-3DOM structure to sinter to a much greater extent than 3DOM and NOM CeO_2. After cycling, the D-3DOM sample is comprised of scattered particles with dimensions of several hundred nm sitting on top of a highly sintered solid. Most of the material consists of the sintered solid, which has micrometer sized grains, and little porosity. The D-3DOM CeO_2 has a specific surface area of 4 m^2 g^{-1} after exposure to temperatures above 1500 K.

Ceria that contains untemplated mesoporosity was produced by thermal decomposition of $Ce(NO_3)_3 \cdot 6\ H_2O$ (Sigma-Aldrich, 99%) in air, and is thus referred to as decomposition synthesized ceria, or DS CeO_2, for short. $Ce(NO_3)_3 \cdot 6\ H_2O$ was calcined in static air in an identical fashion to the calcination of the 3DOM and NOM CeO_2. The thermal decomposition process produced brittle, foam-like ceria powder with particles that contain mesopores between crystallites of ceria.

The DS ceria has the highest specific surface area at 110 $m^2\ g^{-1}$, and also has the smallest average grain size of 8 nm. The high specific surface area is a result of the broad mesopore radii distribution between 2 and 12 nm (Figure 6.2) [140]. The smaller scale pores and small crystallites expose more surface area than the macropores of the 3DOM and NOM CeO_2. The DS ceria loses 99% of its surface area when exposed to 1100 K for one hour (the time corresponding to the first chemical reduction in the isothermal investigation) [140]. Concurrent with the reduction in specific surface area, the crystallites grow to several hundred nanometers and the pore volume shrinks from 0.280 to 0.009 mL g^{-1}, suggesting that the mesopores collapse at 1100 K.

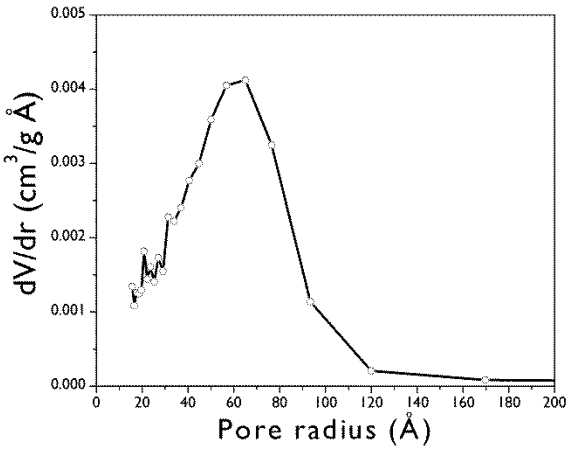

Figure 6.2 Pore sizes in DS CeO_2, showing its broad distribution of mesopores (2-50 nm). Image from Ref. [140].

The commercial ceria has the lowest specific surface area, below the detectable limit of the N_2 sorption instrument ($\leq$1.0 m^2 g^{-1}), and its grains are between 1 and 10 µm, as shown in the SEM images (Figure 6.1(e)). It features smooth surfaces and limited porosity, which is confirmed by the low 0.002 mL g^{-1} pore volume of the material [140]. The commercial ceria experiences little change in morphology and surface area during both isothermal chemical cycling at 1100 K [140] and during thermochemical cycling when exposed to higher temperatures.

6.2 Experimental Methodology

Two experimental platforms were developed to elucidate the impact of the morphology of ceria on the rate of H_2 and CO production. In the first platform, the goal is to isolate the influence of morphology on the kinetics of oxidation, while avoiding the complications associated with thermochemical cycling such as thermally induced changes to the pore network and rapid changes in temperature. For this platform, the temperature of the ceria samples is held constant at 1100 K, avoiding non-isothermal effects on oxidation kinetics, and where sintering and grain growth are less pronounced. Limiting the extent of sintering and grain growth improves the odds of retaining the morphologies of the ceria materials during cycling, allowing them to be differentiated. The ceria samples are reduced at 1100 K using a 5 mol% H_2 mixture (which lowers the oxygen activity of the gas phase), and are subsequently oxidized by mixtures of ~3 mol% H_2O and CO_2 in Ar.

With the understanding of the role of morphology garnered from the first experimental platform, the ceria samples are subjected to rapid thermochemical cycling in the second experimental platform. The samples are reduced in a 10 ppm O_2/N_2 flow over 78 s by rapid heating to a high temperature using an infrared (IR) imaging furnace. Subsequently, samples are cooled and oxidized by a flow of 25 mol% CO_2 over 120 s. Over 50 cycles are completed to test the stability of fuel production. The reduction and oxidation

temperatures and gaseous environments reflect conditions that might be anticipated in the two-step CeO_2-based solar thermochemical cycle.

6.2.1 Isothermal Experimental Platform for the Oxidation of Ceria

The rate of H_2 and CO production over the 3DOM, DS, and commercial ceria powders are investigated in the fixed bed, vertical tubular flow reactor depicted in Figure 6.3. The powders are held in a cylindrical quartz column with a quartz frit (150–200 µm pores). The quartz column has a 10 mm inner diameter (i.d.) upstream of the frit, a 4 mm i.d. downstream of the frit, and 1 mm thick walls. The reactor temperature is maintained at 1100±2 K in an electric furnace (OMEGA CRFC-1512/120-C-A), and controlled using a

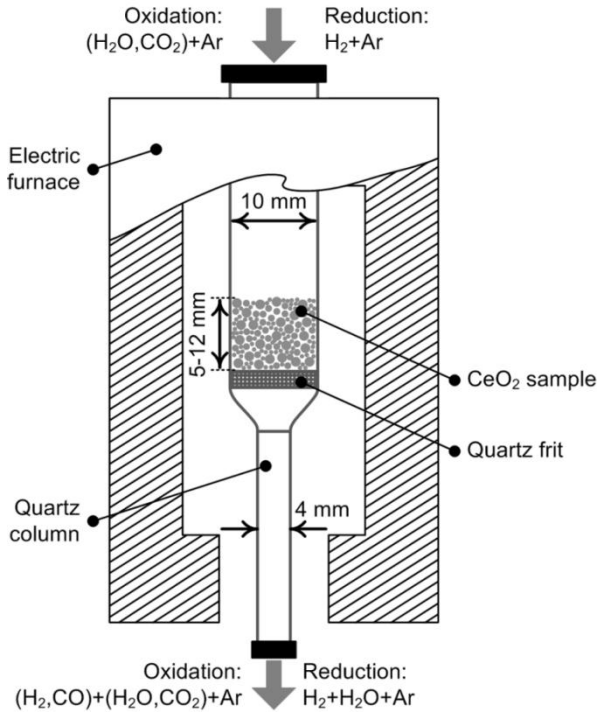

Figure 6.3 Vertical fixed bed reactor for studying the oxidation of ceria at 1100 K. The terms "oxidation" and "reduction" are in reference to the ceria.

type-K thermocouple probe and a custom designed LabVIEW program. The quartz column is sealed at its ends with stainless steel flanges using Viton o-rings. The flanges allow for gas mixtures to be delivered to the reactor via mass flow controllers. The mass flow controllers are calibrated using a Gilibrator volumetric flow meter (Sensidyne Gilibrator-2) to an accuracy of 1% of the flow rate. The composition of the effluent gas is monitored with a quadrupole mass spectrometer (Inficon Transpector CPM) during H_2O splitting and a Raman laser gas analyzer (Atmosphere Recovery, Inc. RLGA-129a) during CO_2 splitting. The gas analyzers are calibrated using standard mixtures of a single solute (H_2, CO, CO_2) in Ar to an accuracy of $\pm$0.02 mol%. For the mass spectrometer, argon is used as an internal reference. The calibration procedure is described in Appendix A.

Prior to each experiment, the quartz column is washed thoroughly with water and then rinsed with acetone to remove residual powder from the walls and frit. The ceria sample is sieved to between 180 and 840 µm, weighed with a digital balance (Sartorious GD-503-NTEP), and loaded into the column. The height of the bed resulting from the gravity feeding of the powder varies between 5 mm and 12 mm. The column is then placed in the furnace, sealed, and purged of air under a flow of pure Ar (99.999% purity).

Subsequently, the sample is cyclically reduced and oxidized. Chemical reduction is performed using a mixture of H_2 in Ar (4.97$\pm$0.05 mol% H_2) at a flow rate of 100–300 mL[6] min^{-1}. The O_2 activity in the mixture, assuming that the manufacturer reported oxygen and water vapor impurities in the gas blend equilibrates with the H_2, is estimated to be $p_{O_2} \approx 10^{-22}$ atm. Using the estimated O_2 activity and the thermodynamics of ceria (see section 5.1), the equilibrium non-stoichiometry at 1100 K is fixed at δ=0.18, limiting the total H_2/CO production to 24 mL g^{-1}. In the first reduction of the samples, the H_2-Ar flow is started with the electric furnace turned off. The furnace is then switched on, and

[6] Gas volumes are reported at 298K and 1 bar throughout this chapter.

ramped at ~80 K/min to 1100 K to initiate the reduction of ceria. During the chemical reduction, H_2O is produced. In subsequent reduction steps, the electric furnace is already at temperature and the H_2-Ar flow is switched on to initiate reduction. In all cycles, the sample is allowed to reduce for 60 min under isothermal conditions, a sufficient amount of time to reach an equilibrium state of reduction. Furthermore, a fixed reduction time ensures that each sample is chemically cycled in an identical manner.

Upon completion of reduction, the reactor is purged of H_2 under a flow of pure Ar. Oxidation is initiated by the delivery of a mixture of H_2O or CO_2 in Ar. The CO_2 mixtures are created by mixing CO_2 (99.99% purity) with Ar so that the CO_2 concentration is nominally 4.0 mol% and the total gas flow rate is 550 mL min^{-1}. The H_2O mixture is created by saturating a 200–1000 mL min^{-1} flow of Ar in a water bubbler maintained at room temperature (298±2 K) so that the H_2O concentration was nominally 2.7 mol%. The flow of reactants in the fixed bed is maintained until no H_2 or CO is detected in the effluent gas. Finally, the reactor is again purged under a flow of Ar to remove all traces of the reactive H_2O and CO_2. This reduction-purge-oxidation-purge procedure, which constitutes a single chemical cycle, lasts approximately 90 min.

To demonstrate the isothermal chemical cycling procedure, the concentration of product gases measured during the first three cycles of the commercial CeO_2 sample are shown in Figure 6.4. At t=0 min, the H_2-Ar mixture is flowing over the sample, and the electric furnace is turned on to initiate reduction. During heating, the concentration of H_2O rises as H_2 removes oxygen from the ceria. H_2O production continues after the furnace reaches 1100 K. After ~60 min the H_2O concentration decreases to zero, indicating the completion of reduction, and the H_2-Ar mixture is purged from the reactor to ready the sample for oxidation. To initiate oxidation, the CO_2 gas mixture is injected to the reactor, and CO is produced immediately. The CO_2 flow is left on until CO production ceases, and then purged from the reactor. When purged, the H_2-Ar flow is started to commence the

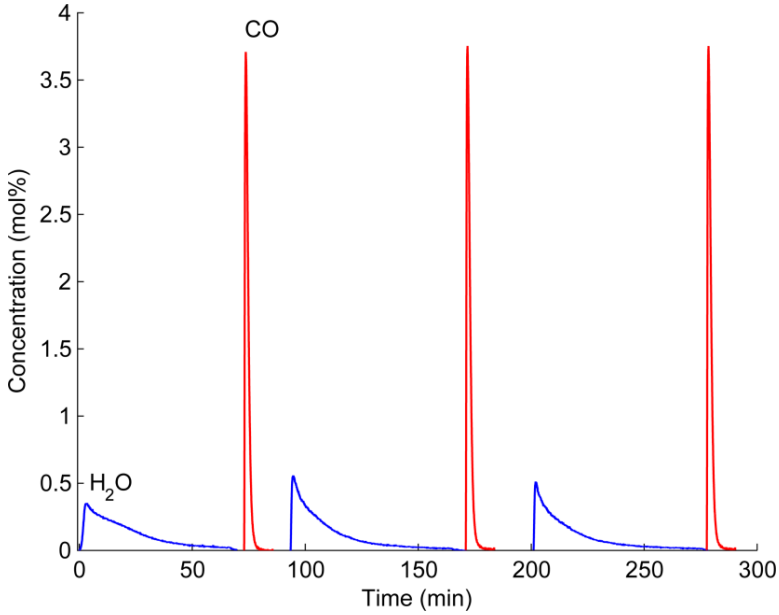

Figure 6.4 The concentration of H_2O and CO during the first three chemical cycles of commercial CeO_2 at 1100 K. During chemical reduction of the ceria in a H_2-Ar mixture, H_2O is produced. Upon delivery of a 4 mol% CO_2 mixture to the ceria, CO is produced.

second cycle. Note that in the second and subsequent cycles, the H_2O concentration rapidly increases to a maximum during reduction since the reactor is already at 1100 K.

6.2.2 Thermochemical Cycling Experimental Platform

The 3DOM, NOM, D-3DOM, and commercial ceria powders are thermochemically cycled in a reactor heated by an Ulvac-Riko VHT-E44 infrared (IR) imaging furnace (Figure 6.5). The ceria powders are sieved to between 180 and 840 µm and packed into a bed in an alumina process tube with an i.d. of 9.5 mm and 1.5 mm thick walls. The length of the bed is 10–30 mm, containing between 0.5 and 2.3 grams of sample. The sample masses differ because of the differences in their porosity. The IR imaging furnace irradiates the process tube to rapidly heat the ceria sample up to 1000 K/min. Rapid heating is made possible by concentration of radiation emitted by tungsten elements using gold-plated, water-cooled elliptical reflectors. Rapid cooling is also possible when the radiation is turned off since the tube exchanges energy with the cold reflector surfaces and ambient air. The furnace is controlled using a platinum-platinum/rhodium thermocouple protected in an alumina sheath located 6 mm downstream of the sample. Using a thermocouple

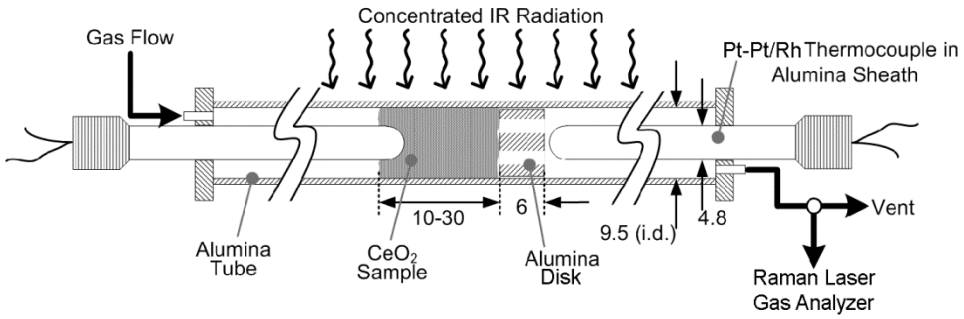

Figure 6.5 Horizontal fixed bed reactor using an infrared imaging furnace for rapid thermochemical cycling of ceria. Dimensions are in mm.

isolated from the samples for furnace control ensures that every sample is identically irradiated. An alumina disk with gas flow channels shields the control thermocouple from the ceria samples and holds the samples in a fixed axial position. A second platinum/platinum-rhodium thermocouple probe is embedded 2–3 mm in the sample on its upstream face.

Reduction of the samples is achieved in a 100 mL min^{-1} flow of N_2 containing 10.5±0.1 ppm O_2 (p_{O_2} = 1.01×10^{-5} atm) by rapid heating at rates of up to 800 K/min to temperatures between 1420 and 1520 K. The samples are reduced for 78 seconds, and then cooled to between 1125 and 1200 K in ~40 s for oxidation. Oxidation is initiated by switching on a 100 mL min^{-1} flow of 25 mol% CO_2 (balance N_2). The flow of CO_2 is automatically started when the thermocouple probe in contact with sample reached the desired temperature. The oxidation flow is terminated after 120 s and the 10 ppm O_2/N_2 flow is reintroduced in the reactor to purge residual CO_2 and reestablish the controlled oxygen activity environment for subsequent reduction. The cycle is repeated up to 55 times.

The first-order time constant of the thermocouple probes is 38 s in the IR furnace system, as determined experimentally, and the probes respond slower than the fast heating and cooling rates achieved in the system. The bias error incurred from the slow response is estimated using a lumped capacitance heat transfer model described in Appendix F. The results reveal that the ceria samples could reach a temperature higher than the maximum temperature reported by the probe during reduction or lower than the minimum temperature reported by the probe during cooling. The maximum overshoot and undershoot bias errors are estimated to be 200–300 K. The errors dissipate over ~1 min. An overshoot error in temperature during the reduction half cycle leads to increased amounts of O_2 evolution than what would be expected based on the uncorrected thermocouple probe response, and an undershoot error during the oxidation half cycle

leads to an underprediction of the kinetics of CO production, as the ceria sample is cooler than the thermocouple probe response.

The O_2 and CO produced from the ceria samples are measured with the Raman Laser Gas Analyzer. Similar to the isothermal experimental platform, the RLGA is calibrated prior to each experiment using gas mixtures of known O_2 and CO concentration to an accuracy of ±0.02 mol%. See Appendix A for additional details regarding the calibration.

6.2.3 Data Analysis

The total mass flow rate of fluid through the fixed beds in the two experimental platforms is sufficiently high in all experiments to ensure that the bed behaved in a quasi-steady state fashion, which is a key feature of the experiments. Gas flow rates vary between 200 and 1000 mL min^{-1}, and with the reactor at temperatures between 1100 and 1500 K, these flow rates correspond to residence times in the fluid volume of the fixed bed on the order of 1–100 ms. As will be shown, the oxidation of the samples in the isothermal and thermochemical cycling experimental platforms occurs over the course of minutes. The storage of reacting species in the fluid volume of the fixed bed can thus be neglected, and the instantaneous fuel flow rate measured at the outlet of the fixed bed is equivalent to the instantaneous, spatially averaged fuel production rate within the bed.

The total volume of O_2, H_2, or CO produced, V_i, is calculated by integrating the instantaneous gas production rate in time,

$$V_i = \int_0^{t_d} r_i \, dt \tag{6.1}$$

The instantaneous gas production rate, r_i, where i corresponds to either O_2, H_2, or CO, is equivalent to the molar flow rate of species i at the outlet of the fixed bed. The flow rate of species i is the product of the known total flow rate (Q_{total}) and the measured O_2, H_2 or CO concentration (y_{O_2}, y_{H_2}, y_{CO}).

$$r_i = Q_{\text{total}} \times y_i \tag{6.2}$$

Sample productivity is defined as the total amount of O_2, H_2, or CO produced normalized by the mass of ceria that produced the gas, m_s.

$$V_i' = \frac{V_i}{m_s} \tag{6.3}$$

A reaction extent is defined as the amount of O_2, H_2, or CO produced from the start of production to time, t, relative to the total produced over the duration of production, t_d.

$$X_i = \frac{\int_0^t r_i \, dt}{V_i} \tag{6.4}$$

Process and systematic uncertainties in the measurands are propagated to the fuel production rates and productivity using the sequential perturbation method, and are reported at 95% confidence. Measurement uncertainty and the application of the sequential perturbation method are described in more detail in Appendix A.

6.3 Results and Discussion

6.3.1 Isothermal Cycling at 1100 K Featuring Chemical Reduction

Table 6.1 summarizes the reaction data measured in the isothermal chemical cycling test platform (Figure 6.3), including the maximum fuel production rate and the total gas volume evolved from the samples. The rate of H_2 production during H_2O splitting over the 3DOM CeO_2 is shown in Figure 6.6 for six cycles as representative of the behavior observed for all of the samples. With the introduction of H_2O at $t = 0$, H_2 production commences immediately, and the rate of H_2 production increases to a maximum as H_2O reaches the sample. After reaching a maximum, the rate of H_2 production decays as the remaining oxygen vacancies in the ceria lattice are filled. The maximum production rate

Table 6.1 CeO_2 **sample productivity and maximum fuel production rate for the sixth cycle in the vertical, fixed bed test platform.**

Material	m_s (g)	V'_{fuel} (mL g^{-1})	$r'_{fuel.max}$ (mL min^{-1} g^{-1})
		H_2O Splitting	
Commercial CeO_2	1.36	21 ± 1	6.0 ± 0.2
DS CeO_2	0.78	20 ± 1	7.8 ± 0.2
3DOM CeO_2	0.25	20 ± 1	13.6 ± 0.4
		CO_2 Splitting	
Commercial CeO_2	1.36	23 ± 1	10.3 ± 0.2
DS CeO_2	0.70	23 ± 2	13.0 ± 0.2
3DOM CeO_2	0.24	22 ± 2	36.7 ± 0.5

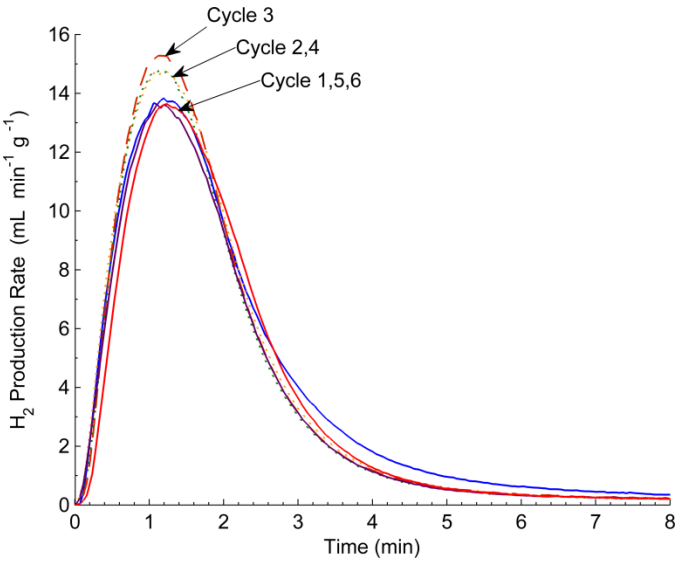

Figure 6.6 The rate of production of H_2 during the oxidation of 3DOM CeO_2 at 1100 K over 6 isothermal chemical redox cycles.

increases by 10% over the first 3 cycles for 3DOM CeO_2, but this increase disappears by the fifth cycle, and there is no change in the rate of H_2 production from cycle 5 to cycle 6. The relative stability of H_2 production shown in Figure 6.6 is also observed for the DS and commercial CeO_2 samples. There is not a statistically significant difference between the rate of fuel production during ceria oxidation in the first and sixth cycle for any sample.

Given the stability of the oxidation chemistry during isothermal cycling, the oxidation of the ceria samples are compared in cycle 6 only. Figure 6.7 shows the H_2 and CO production rates of the samples as functions of time and reaction extent during oxidation. There are considerable differences in the maximum rates of fuel production and fuel production curves for the three ceria morphologies. The DS CeO_2 oxidizes faster than the commercial CeO_2, given the higher peak fuel production rate and the shorter time required to reach completion. The maximum H_2 and CO production rates of the DS CeO_2 are 7.8 mL g^{-1} min^{-1} and 13.0 mL g^{-1} min^{-1}, respectively, compared to 6.0 mL g^{-1} min^{-1} and 10.3 mL g^{-1} min^{-1} for the commercial CeO_2. The improved reactivity of the DS CeO_2 over the commercial CeO_2 demonstrates the importance of porosity for the heterogeneous kinetics. While the specific surface areas of the DS and commercial CeO_2 are dramatically different prior to cycling (110 m^2 g^{-1} and $\leq$ 1 m^2 g^{-1}, respectively), they are both low during oxidation, on the order or below the detectable limit of the N_2 sorption instrument ($\leq$ 1.0 m^2 g^{-1}). It was determined in a separate experiment that the DS CeO_2 loses most of its 110 m^2 g^{-1} surface area during the first chemical reduction at 1100 K over $\sim$ 1 h. The DS and commercial CeO_2 thus differ mostly in porosity during oxidation. The DS ceria retains a pore volume of 0.009 mL g^{-1}, while the commercial ceria has the lowest pore volume of 0.002 mL g^{-1}.

The data for DS CeO_2 shows the importance of porosity for the kinetics of fuel production, while the data for 3DOM CeO_2 demonstrates the importance of maintaining specific surface area. 3DOM CeO_2 oxidizes significantly faster than both the DS and

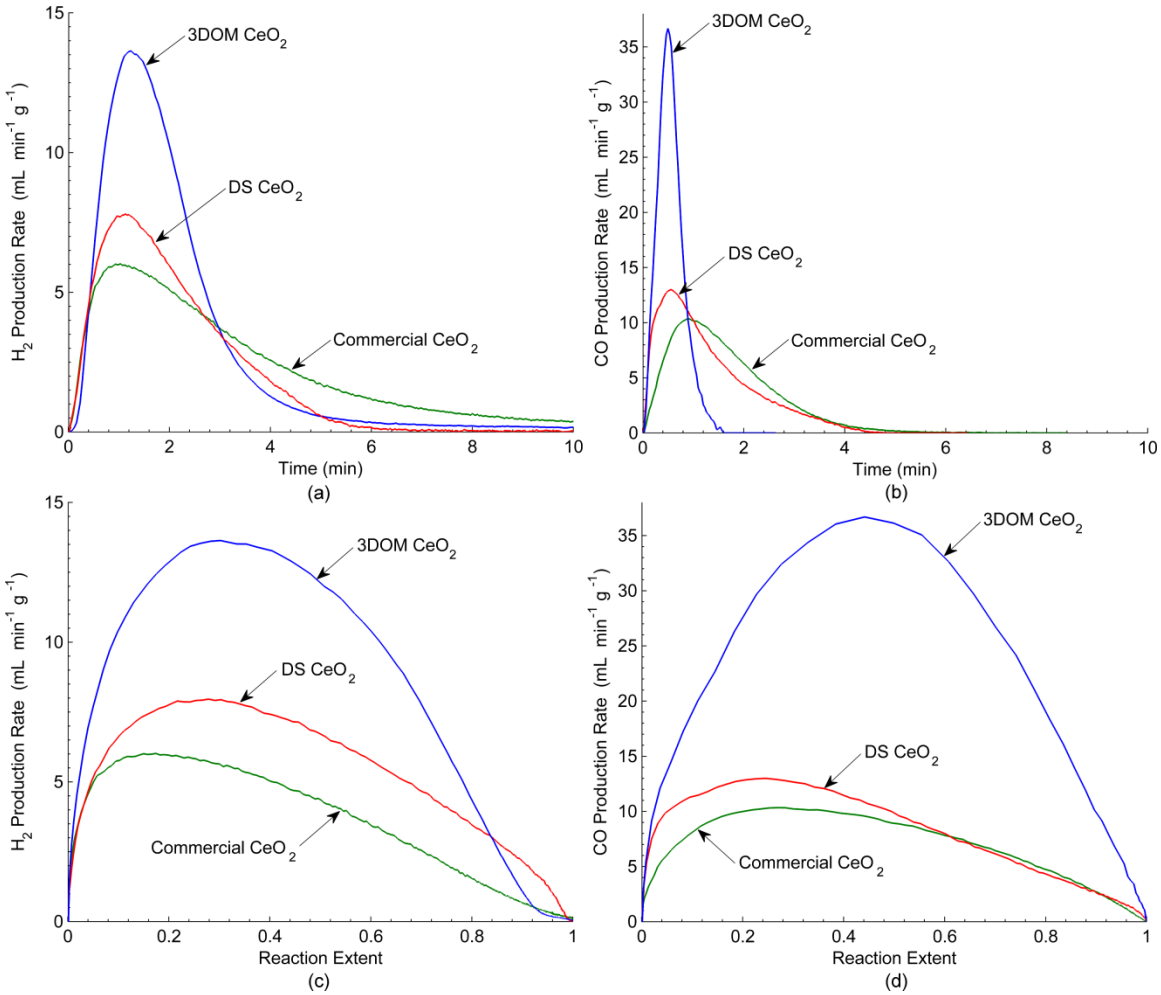

Figure 6.7 The rate of production of fuel as a function of time at 1100 K for the 3DOM, DS, and commercial CeO_2 samples for (a) H_2O- and (b) CO_2-splitting and the rate of production of fuel as a function of the reaction extent for (c) H_2O- and (d) CO_2-splitting. The conditions for (a) and (c) are y_{H2O} = 2.7±0.1 mol% and Q_{total} = 200–1000 mL min^{-1}. The conditions for (b) and (d) are y_{CO2} = 4.0±0.2 mol% and Q_{total} = 550 mL min^{-1}.

commercial CeO_2 (Figure 6.7), with maximum H_2 and CO production rates of 13.6 mL g^{-1} min^{-1} and 37.4 mL g^{-1} min^{-1}, corresponding to increases of 75%–260%. The 3DOM CeO_2retains a specific surface area of 10 m^2 g^{-1}, an order of magnitude larger than the DS and commercial CeO_2, and thus offers an increased number of active sites for H_2O- and CO_2-splitting. An additional differentiating feature of 3DOM CeO_2 is that it retains small solid features during isothermal chemical cycling, on the order of hundreds of nm (Figure 6.8(a and b)), which facilitate the diffusion of atomic oxygen to the ceria surface. However, time scales for atomic oxygen diffusion estimated in section 5.2.2 are on the order of ms for diffusion lengths up to hundreds of µm. Since oxidation occurs over the course of minutes for 3DOM CeO_2, diffusion of oxygen through the solid is unlikely to significantly impact the global kinetics. In contrast, for the dense commercial CeO_2, comprised of granules with average dimensions on the order of 0.5 mm, unfavorably long diffusion lengths could contribute to its slow oxidation.

The kinetic advantage of 3DOM CeO_2 stems from its ordered macroporous morphology. Held at 1100 K, 3DOM CeO_2 sinters, but retains the interconnected and ordered pore network (Figure 6.8(a)). Additionally, it remains nanocrystalline. The XRD pattern of the 3DOM CeO_2 after cycling exhibits broad peaks, and the average crystallite size is 80 nm, as confirmed in TEM images (Figure 6.8(b)). As a result, 3DOM CeO_2 maintains its moderate specific surface area, and provides rapidly accessible surface sites for oxidation throughout the volume of the ceria particles. The DS ceria, in contrast to 3DOM ceria, undergoes extensive sintering and grain growth during its first reduction. Grains significantly larger than 100 nm are observed in SEM and TEM images of the sintered DS CeO_2 (Figure 6.8(c and d)), and the dramatic loss of specific surface area drastically reduces the number of reaction sites. These adverse changes lead to the slow rates of fuel production relative to the 3DOM CeO_2.

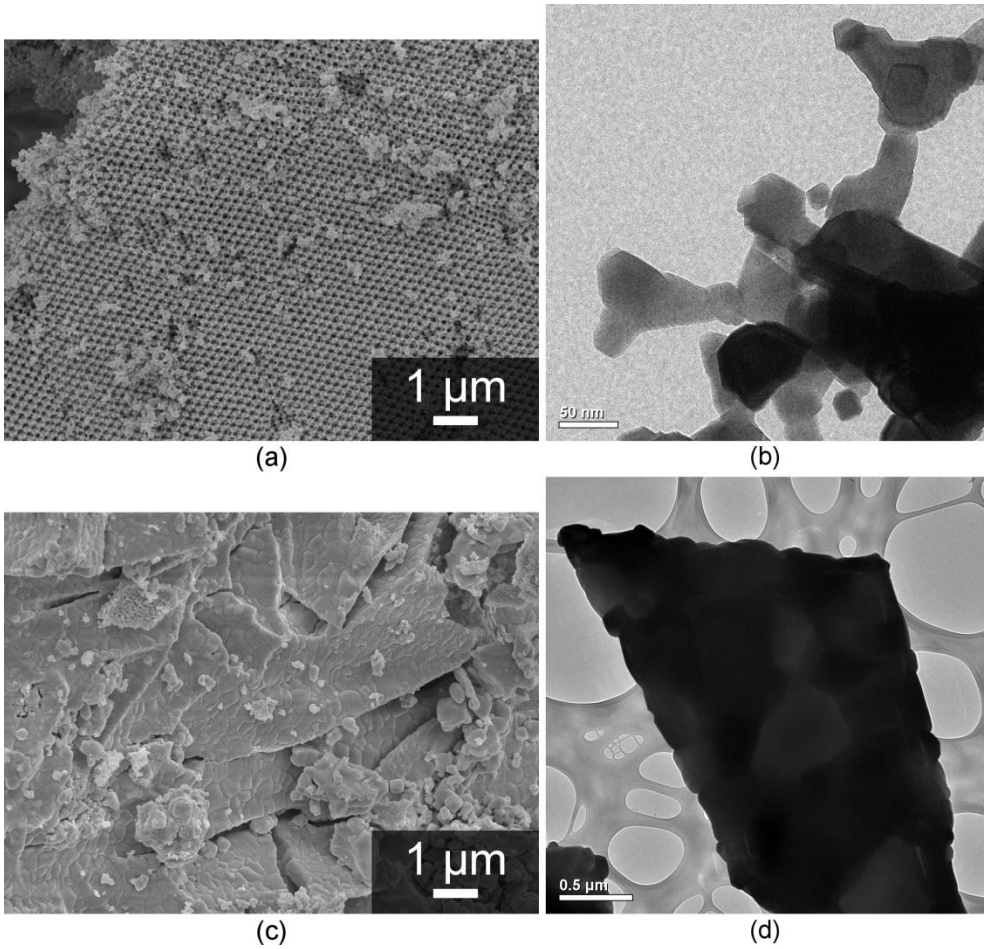

Figure 6.8 SEM (a) and TEM (b) images of 3DOM CeO_2 and SEM (c) and TEM (d) images of DS CeO_2 after isothermal chemical cycling at 1100 K. Images appear in Ref. [140].

Ceria morphology strongly influences the kinetics of H_2 and CO production, but morphology has no influence on the chemical equilibrium of the system. Thus, all three samples, regardless of their structure, produce the same amount of fuel when H_2O and CO_2 are split: 20±1 mL g^{-1} of H_2 and 23±2 mL g^{-1} of CO, respectively. The productivity achieved in the isothermal platform reflects the use of H_2 to chemically reduce the ceria, which creates a very low effective oxygen partial pressure of p_{O_2}~10^{-22} atm. As a result, the ceria is reduced to δ=0.16±0.02, in agreement with the δ=0.18 non-stoichiometry predicted from ceria thermodynamics [117]. This deep reduction highlights an important advantage of ceria as a solid-state reaction substrate for thermochemical fuel production: it can undergo large changes in its non-stoichiometry without undergoing an irreversible phase change. An XRD analysis confirms that the phase of the ceria in all samples was unchanged after isothermal chemical cycling [140].

The results obtained in the isothermal experimental platform show the benefit of porous materials for solar thermochemical cycling of non-stoichiometric oxides for fuel production. It is extremely beneficial to engineer a network of interconnected pores in the oxides, including ceria, to improve fuel production kinetics, provided adequate resistance to sintering can be achieved. The resistance to sintering is studied in the second, full thermochemical cycling investigation.

6.3.2 Thermochemical Cycling of Porous Ceria

Having identified the benefit of an engineered network of interconnected macropores in ceria for the kinetics of fuel production at 1100K, the study of the macroporous ceria is extended to full thermochemical cycling, i.e., utilizing thermal, rather than chemical, reduction. The high temperature, O_2 producing step requires temperatures in excess of 1300 K, and more severe structural changes in porous ceria were anticipated. Thermally-activated sintering and associated grain growth can greatly reduce the available surface

area of the 3DOM CeO_2, and, eliminate the interconnected macroporosity through extensive densification. Given the major structural changes of the mesoporous DS CeO_2 that leads to a significant loss of surface area at 1100 K and presumably its slow rate of fuel production, it is not included in the thermochemical cycling experiments. Rather, the NOM and D-3DOM CeO_2 are introduced for comparison to 3DOM CeO_2, the former to evaluate the importance of the order in the 3DOM macropore array, and the latter to examine the effect of ceria particle packing density on materials with similar initial feature sizes.

The first step of thermochemical cycling is the partial reduction of ceria in a low oxygen activity atmosphere (p_{O_2}=1.01×10^{-5} atm) under rapid heating to a high temperature, with a typical temperature profile shown in Figure 6.9 for the case of 3DOM CeO_2. Data for all cycles and for all samples are archived in Appendix G. When heated at rates up to 800 K/min (as might be expected when directly irradiated by concentrated solar energy), 3DOM CeO_2 rapidly releases oxygen with a peak release rate of 2.4 mL min^{-1} g^{-1}. Oxygen evolution is complete in less than 60 s, before the end of the reduction step. Similar to other porous materials [35], the rate of oxygen release from 3DOM and NOM CeO_2 correlates with the rate of temperature rise measured by the thermocouple embedded in the sample, indicating that the O_2 release rate is limited by the rate of temperature rise, and not the intrinsic chemical kinetics of reduction. Indeed, when the temperature ramp rate is decreased, the rate of O_2 release also decreases. In Figure 6.10, the rate of O_2 release is compared for 3DOM ceria rapidly heated at 800 K/min and moderately heated at 50 K/min. For the slower heating rate, the rate of O_2 release is barely detected by the Raman laser gas analyzer, remaining below 0.08 mL min^{-1} g^{-1}, while for the fast heating rate, a well-defined peak is observed with a maximum O_2 production rate of 2.4 mL min^{-1} g^{-1}. The release of O_2 is confirmed during the slow heating by subsequently oxidizing the 3DOM CeO_2 with CO_2 and measuring the CO produced.

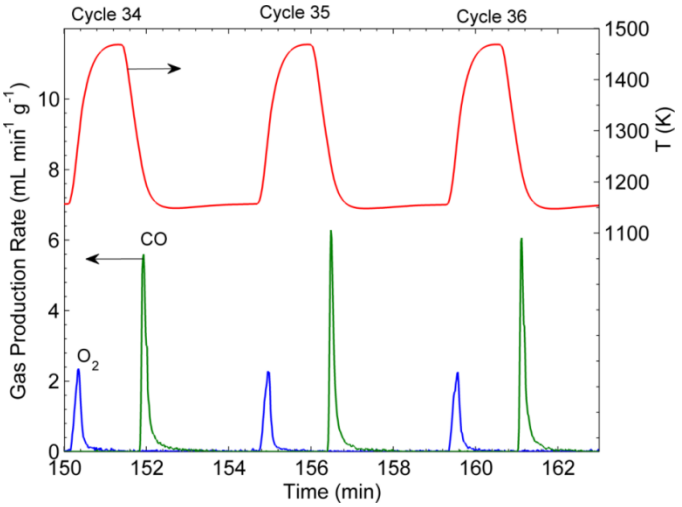

Figure 6.9 The rate of O_2 and CO production during thermochemical cycling of 3DOM CeO_2 in cycles 34-36 (representative of stable cycling) and the corresponding temperature recorded by the temperature probe embedded in the sample.

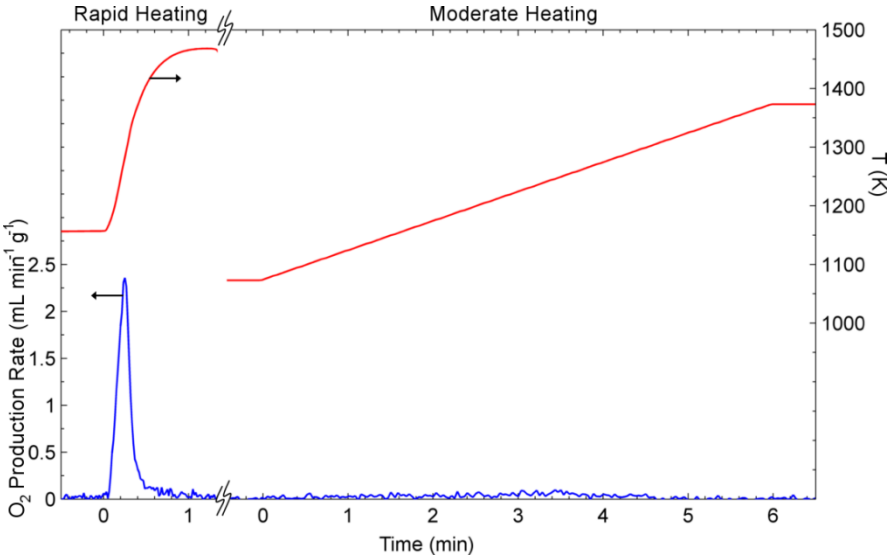

Figure 6.10 The rate of O_2 release from 3DOM CeO_2 heated at up to 800 K/min and at 50 K/min and corresponding temperature recorded by the thermocouple probe embedded in the sample.

In the second step of the cycle, the material is quickly cooled to ~1130 K and CO_2 is injected in the reactor. During this process, CO is rapidly produced, and the 3DOM CeO_2reoxidizes in less than 90 seconds, reaching a maximum rate of CO production of ~6 mL min^{-1} g^{-1} (5.6, 6.1, and 6.0 mL min^{-1} g^{-1} in cycles 34, 35, and 36, respectively). The rates of O_2 and CO production over 3DOM CeO_2, respectively, are stable for 55 cycles. In cycle 55, the maximum rates of O_2 and CO production are 2.3 and 6.1 mL min^{-1} g^{-1}, identical to cycles 34–36 within experimental error. The rapid rates of 3DOM CeO_2 reduction and oxidation allow for the rapid thermochemical cycling frequency in the present work: one cycle is completed every four minutes. This cycling frequency is, to my knowledge, the fastest to have been demonstrated for temperatures between 1100 and 1500 K. Rapid cycling rates are critical for increasing the throughput of fuel over a given period of time. Alternately, one can raise the temperature at which ceria is reduced; however, this approach increases reradiation losses and the extent of ceria sintering and grain growth, which can ultimately reduce fuel throughput and cycle efficiency.

The differences in the morphologies of the various samples gives rise to important differences in the total CO produced. Figure 6.11 shows the productivity of the 3DOM, NOM, D-3DOM, and commercial CeO_2 over multiple thermochemical cycles (productivity is defined in equation (6.3)). 3DOM and NOM CeO_2 are both capable of thermochemical cycling with fast reaction kinetics and stable cycle-to-cycle fuel production. The rise in cycle-to-cycle O_2 and CO productivity from the 3DOM and NOM CeO_2 samples over the first 20 cycles tracks the maximum temperature attained by the temperature probe embedded in the sample (Figure 6.11(b)). Once stable cycle-to-cycle production is achieved, the representative CO productivity for the materials in a given cycle are 0.9±0.1 mL g^{-1} for 3DOM CeO_2 and 1.0±0.2 mL g^{-1} for NOM CeO_2. The non-stoichiometric thermodynamics of CeO_2 predicts that for an atmosphere with an oxygen partial pressure of 1.01×10^{-5} atm, ceria is reduced to a greater extent at higher temperatures. Therefore,

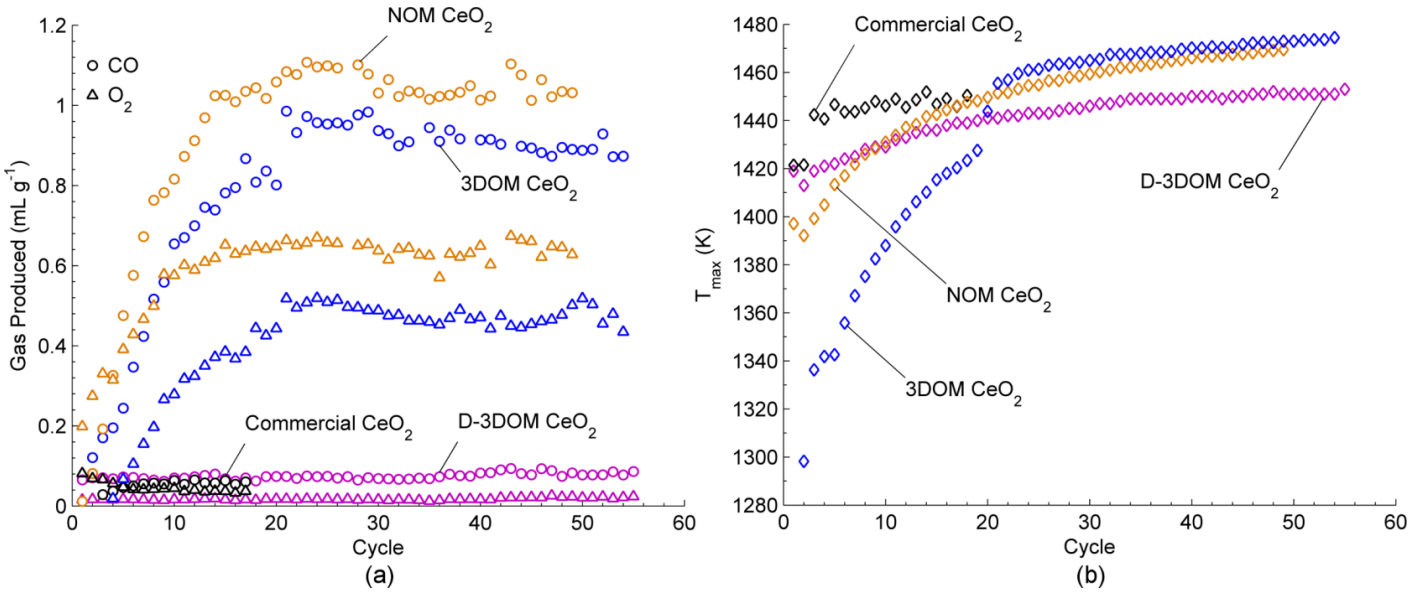

Figure 6.11 (a) The total O_2 and CO produced in each thermochemical cycle over 3DOM, NOM, D-3DOM, and commercial CeO_2. (b) The maximum temperature recorded by the temperature probe embedded in the sample during reduction in each cycle.

the rise from ~0 to 0.95 and 1.1 mL g^{-1}, in the 3DOM and NOM CeO_2 productivities over the first 20 cycles shows that the system is behaving as expected thermodynamically. Within experimental error, twice as much CO is produced from the 3DOM and NOM CeO_2 than O_2. The 2:1 ratio is consistent with the stoichiometry of CO_2-splitting, and indicates that the oxygen vacancies formed during reduction are fully utilized during oxidation. Based on the maximum temperature of 1480 K attained by the probe embedded in the 3DOM and NOM CeO_2 samples (Figure 6.11(b)), the thermodynamically predicted limit for fuel production is 0.6 mL g^{-1} of CO and 0.3 mL g^{-1} of O_2, assuming complete utilization of the non-stoichiometry formed with $p_{O_2}=1.01\times10^{-5}$ atm. The 3DOM and NOM CeO_2 produces more CO and O_2 than this limit. At equilibrium, 3DOM and NOM CeO_2 would need to have an average temperature of 1520 K to produce the measured amount of CO/O_2, which suggests that the sample is, on average, 50 K hotter than the thermocouple reading. It is thus most interesting to note that compensating for the time response of the thermocouple probes indicates that the probes underreport the sample temperature by 40–60 K.

Both the commercial CeO_2 and the D-3DOM CeO_2 materials produce an order of magnitude less CO than the macroporous ceria materials (for stable cycle-to-cycle production). The specific CO productivity values in a given cycle are 0.06 ± 0.03 mL g^{-1} for commercial CeO_2 and 0.08 ± 0.06 mL g^{-1} for D-3DOM CeO_2. Given that all samples are chemically identical and reach similar reduction and oxidation temperatures, the contrast between the productivities of the commercial CeO_2, the D-3DOM CeO_2, and the 3DOM and NOM CeO_2 must be related to the differences in fuel production kinetics stemming from differences in morphology.

Figure 6.12 shows the rate of O_2 and CO production for two representative cycles for each of the ceria morphologies thermochemically cycled. The peak O_2 production rates are

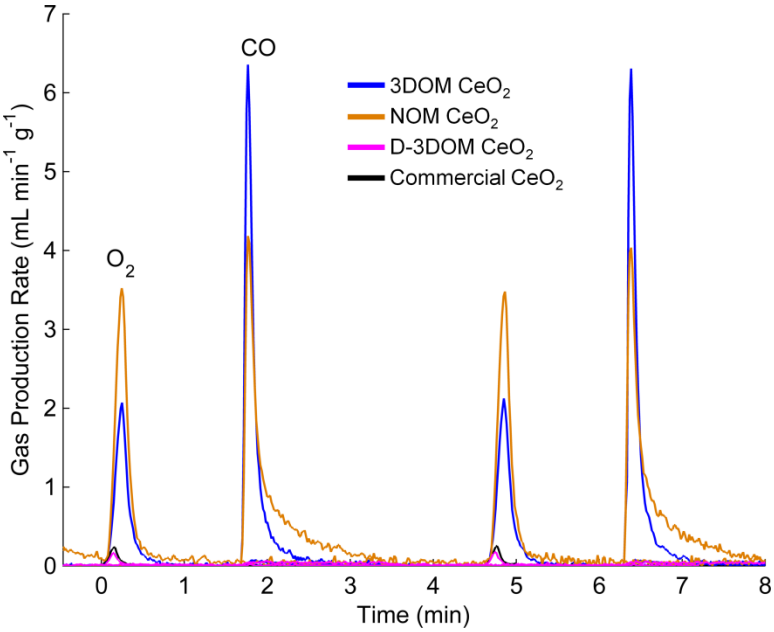

Figure 6.12 The rate of O_2 and CO production for 3DOM, NOM, D-3DOM, and commercial CeO_2 for representative cycles.

greatest for NOM and 3DOM CeO_2, and significantly slower for the more dense D-3DOM and commercial CeO_2. Most interesting is that O_2 production is complete after 15 s for the D-3DOM and commercial CeO_2, while O_2 production for the 3DOM and NOM CeO_2 proceeds over 45 s. Because the rate of reduction is tied to the rate at which the ceria temperature is raised, as demonstrated in Figure 6.10, the 30 s difference in reduction time between the macroporous samples and the more dense samples is most likely attributed to the different productivities of the samples, that is, the total amount of O_2 that is produced. The commercial and D-3DOM CeO_2 samples reduce faster because they produce less O_2, and experience a smaller change in non-stoichiometry.

For oxidation, CO at different rates for all samples, and there are importance kinetic differences among the samples. The maximum rate of CO production is 6.4 mL min^{-1} g^{-1} for 3DOM CeO_2, greater than NOM CeO_2, for which the maximum rate of CO production is 4 mL min^{-1} g^{-1}. Additionally, after reaching the maximum rate of CO production, the

production rate drops quickly in 3DOM CeO_2, and CO production is complete in 45 s. For NOM CeO_2, the CO production decays over a longer period of time, reaching completion in 60 s. The slight kinetic difference between the 3DOM and NOM CeO_2 may be a consequence of their different initial morphologies. After cycling, both of the macroporous ceria samples possess a disordered network of pores (Figure 6.13), but there are differences in the pore structures. The thickness of the walls separating the pores in the NOM CeO_2 is 340 nm on average, thicker than the 150 nm walls separating the pores in the 3DOM CeO_2. The thicker walls of the NOM CeO_2 after cycling suggest that it was more susceptible to adverse morphological changes during thermochemical cycling that could lead to less interconnectivity in its pore network than was retained in the 3DOM CeO_2. The reduction in interconnectivity relative to 3DOM CeO_2 might lead to the slower kinetics shown in Figure 6.12.

The commercial and D-3DOM CeO_2 sample produced CO far more slowly than the other ceria samples (illustrated in Figure 6.12), and the slow kinetics are responsible for the reduced CO productivity shown in Figure 6.9. The rate of oxidation of the denser samples is less than 0.1 mL min^{-1} g^{-1}, and the 2 minutes allotted for oxidation of these samples is insufficient to fully utilize the non-stoichiometry developed during reduction. To illustrate the incomplete utilization of oxygen vacancies, consider the commercial CeO_2. In the first cycle, the commercial CeO_2 produces 0.08 mL g^{-1} (Figure 6.11). In subsequent cycles, the O_2 productivity decreases and by cycle 5 is 0.04 mL g^{-1}. While the O_2 productivity decreases over the first 5 cycles, the CO productivity increases from zero (any CO produced is undetected by the Raman laser gas analyzer in cycle 1) to 0.06 mL g^{-1}. The decreasing O_2 productivity with increasing CO productivity indicates that vacancies are formed in the commercial CeO_2 during reduction and left unfilled during oxidation. Eventually the cyclic O_2 and CO productivity stabilizes, and the commercial CeO_2 cycles between two partially reduced states.

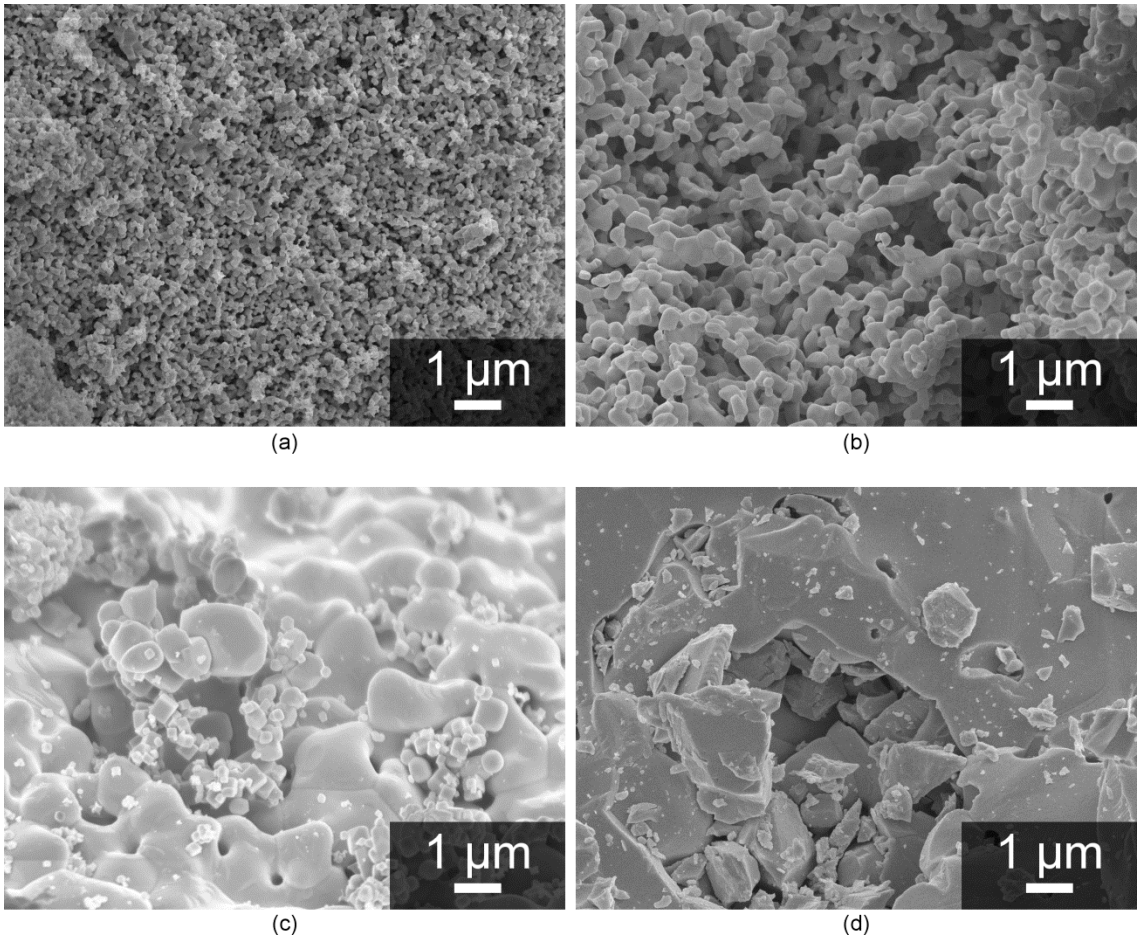

Figure 6.13 SEM images of the (a) 3DOM CeO_2, (b) NOM CeO_2, (c) D-3DOM CeO_2, and (d) commercial CeO_2 after thermochemical cycling during which the samples are exposed to temperatures above 1500 K. Images courtesy of Nick Petkovich and Stephen Rudisill, Department of Chemistry, University of Minnesota.

Evidence for incomplete utilization of the non-stoichiometry can also be seen in the rate of CO production in time. At the end of the 2-minute oxidation when the CO_2 flow is turned off, the CO production curve drops abruptly (Figure 6.14, inset). When the same material is left to oxidize over a longer period of time (after a long period of reduction), CO production decreases gradually over the course of 15 minutes, before dropping below the detection limit of the Raman laser gas analyzer (100 ppm). Incomplete utilization of the non-stoichiometry is a kinetic effect; thermodynamics indicates that the ceria should, given enough time, be completely reoxidized for the present conditions.

The slow rate of oxidation of commercial CeO_2 is a consequence of its unfavorable morphology for gas-solid chemistry. The commercial CeO_2 lacks porosity, contains 1–10 µm grains (Figure 6.1(e)), and oxidation sites are restricted to the very limited surface area of the 200–800 µm commercial CeO_2 particles. The specific surface area of the

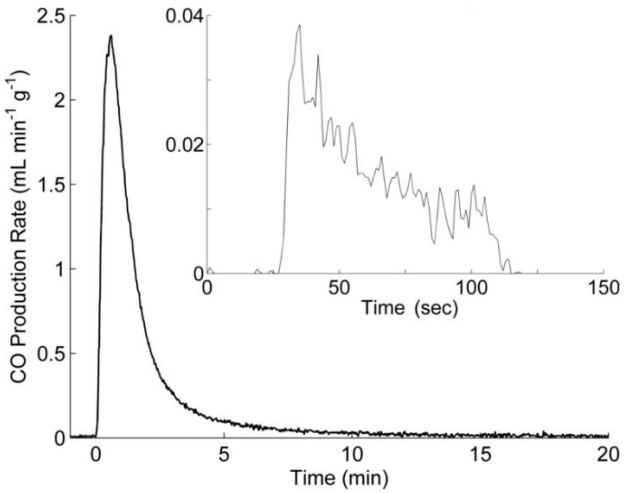

Figure 6.14 Characteristic CO production from nonporous CeO_2 when sufficient time is given for the material to completely reduce and oxidize. The inset shows the abrupt drop in CO production at the end of an oxidation step during rapid cycling, showing that oxidation was incomplete when the CO_2 flow was shut off.

commercial ceria is below the detectable limit of the N_2 sorption instrument ($\leq$ 1.0 m^2 g^{-1}). Also, the lack of a pore network that extends through the particles makes for longer oxygen diffusion lengths compared to a more porous material. These unfavorable lengths, which are on the order of the ~0.5 mm granule size, may lead to atomic oxygen diffusion limitations for the 1100 to 1200 K oxidation temperatures in the commercial CeO_2 sample.

In the case of D-3DOM CeO_2, even though initial feature sizes resemble those of the parent 3DOM CeO_2 material, the reduced open space and more extensive sintering is responsible for the lower productivity. After cycling, the D-3DOM sample consists mostly of sintered micrometer-sized grains with little porosity (Figure 6.13(c)). While the D-3DOM ceria has a surface area comparable to that of the macroporous samples after cycling, the surfaces are likely not accessible during the thermochemical cycling experiments, as they are confined to particles at the interior of the fixed bed, below more heavily sintered material at the exterior.

The CO_2-splitting data for the porous ceria samples in the present study illuminate the desirable characteristics of reactive non-stoichiometric oxides for use in solar thermochemical cycles. Accessible surface area, interconnected pores, and small feature sizes are important parameters for controlling the reaction kinetics and related productivity of ceria. The interconnected porosity, with pore sizes on the order of hundreds of nm, in the 3DOM and NOM CeO_2 materials provides easy access for H_2O or CO_2 to the moderate surface area throughout the volume of the ceria particles. As a result, the rate of oxidation in NOM and 3DOM CeO_2 is enhanced, leading to the stark differences in the rate of CO production between the macroporous and dense, sintered ceria samples. The maximum rate of CO production for the 3DOM and NOM CeO_2 is 6.4 and 4 mL min^{-1} g^{-1}, respectively, an order of magnitude faster than the maximum rate of CO production over the D-3DOM and commercial CeO_2: 0.04–0.06 mL min^{-1} g^{-1}. The data for thermal reduction of the ceria samples suggests that it is primarily limited by heat transfer (Figure

6.10, but also see Appendix F). It is thus the fuel production step that is most sensitive to morphology, presumably due to a rate-limiting chemical step at the ceria surface where atomic oxygen is exchanged and incorporated into the solid. The enhanced reactivity of the 3DOM and NOM CeO_2 samples is a consequence of their templated, engineered macroporosity.

6.4 Summary

The productivity and H_2O and CO_2 splitting kinetics of 3DOM CeO_2 powder is compared with non-ordered macroporous (NOM CeO_2), mesoporous (DS CeO_2), fragmented 3DOM (D-3DOM CeO_2), and low porosity, sintered (commercial CeO_2) ceria. Two experimental platforms are employed. In the first, ceria samples are cycled chemically in a fixed bed held at 1100 K to mitigate sintering and preserve the porous morphologies. In the second, the ceria samples are thermochemically cycled, exposing them to the high temperatures required for thermal reduction. Chemical cycling consists of sample reduction via a mixture of 5 mol% H_2, and subsequent oxidation in a gas flow of 3–4% H_2O and CO_2, allowing both the reduction and oxidation to reach completion at 1100 K. Thermochemical cycling consists of a 78 s reduction with rapid heating at rates up to 800 K/min to ~1500 K in a gas flow with $p_{O_2}=1.01\times10^{-5}$ atm and a 120 s oxidation at 1100–1200 K in a gas flow composed of 25 mol% CO_2. The rapid cycling frequency prevents samples with slow kinetics from completely reducing and oxidizing to the extent permitted by thermodynamics.

3DOM CeO_2, with a moderate specific surface area (10 $m^2\ g^{-1}$ after chemical cycling and 4 $m^2\ g^{-1}$ after thermochemical cycling), augments the reactivity of the non-stoichiometric solid. After chemical reduction at 1100 K, 3DOM CeO_2 produces H_2 and CO 2–3 times faster than DS CeO_2 and the commercial CeO_2. For example, the maximum rate of H_2 production over 3DOM CeO_2 is 14 mL $min^{-1}\ g^{-1}$, over DS CeO_2 is 8 mL $min^{-1}\ g^{-1}$, and

over commercial CeO_2 is 6 mL min^{-1} g^{-1}. The data for CO production ranks the materials similarly. The increased kinetics of the 3DOM CeO_2 is attributed to the retention of specific surface area and morphology over the course of 9 h at 1100 K and to the accessibility of the surface area to reacting species via the interconnected pores arranged in a face-centered cubic array.

The porous materials are exposed to higher temperatures during the thermal reduction step in full thermochemical cycling that lead to more extensive morphological changes. At temperatures in excess of 1500 K, the 3DOM CeO_2 loses its ordered pore structure, but it retains a disordered network of macropores similar to the NOM CeO_2. The maximum rates of CO production over the 3DOM and NOM CeO_2 are 6.4 and 4.0 mL min^{-1} g^{-1}, respectively, an order of magnitude larger than for nonporous and D-3DOM CeO_2, which are below 0.1 mL min^{-1} g^{-1}. Consequently, the total CO produced over the fixed oxidation time, are, for the macroporous morphologies with features sizes between 100 and 500 nm, larger than for the commercial and D-3DOM CeO_2.

The rapid H_2O and CO_2 splitting kinetics achieved with the template, macroporous ceria demonstrate that materials with moderate specific surface area and porosity improve the fuel production step of the two-step CeO_2 thermochemical cycle.

7 Conclusions

This dissertation presented two studies. Part I considered the heterogeneous oxidation of Zn(g) for H_2 and CO production in the Zn/ZnO solar thermochemical cycle. Part II considered the influence of solid morphology on the kinetics of H_2 and CO production in the $CeO_2/CeO_{2-\delta}$ cycle.

7.1 Summary

7.1.1 The Heterogeneous Oxidation of Zn(g)

A new approach to achieve rapid oxidation of Zn was proposed: the heterogeneous oxidation of Zn(g). This reaction pathway circumvents the solid-state diffusion limitation to Zn(ℓ,s) oxidation. To demonstrate the promise of the heterogeneous oxidation of Zn(g), the thermodynamics of the Zn/ZnO cycle was modeled and the kinetics of Zn(g) oxidation by H_2O and CO_2 were measured. The objectives were to measure the rate of the surface oxidation of Zn(g), to develop kinetic expressions suitable for use in designing a heterogeneous Zn(g) oxidation reactor, and to show the potential efficiency gains for H_2 and CO production when Zn is rapidly converted via the heterogeneous oxidation of Zn(g). Gaseous Zn was oxidized in a tubular quartz reactor at temperatures between 800 and 1150 K, for Zn(g) concentrations up to 57 mol%, for H_2O concentrations up to 60 mol%, and for CO_2 concentrations up to 80 mol%. For both H_2O- and CO_2-splitting, the rate of Zn(g) oxidation is rapid—on the order of 10^{-8}–10^{-5} mol cm^{-2} s^{-1}, representing at least an order of magnitude increase in the rate of oxidation over the rates characteristic of Zn(ℓ,s) oxidation [43, 44, 46, 84]. Conversions of zinc greater than 80% are possible in seconds. At 1100 K, H_2O oxidized 80% of Zn(g) in 0.2 s. At lower temperatures, H_2O oxidized more

zinc, reaching 100% conversion at 800 K in 1 s. Similarly, at 1150 K, CO_2 oxidized 84% of Zn(g) in 0.4 s, and higher conversions were experimentally demonstrated at lower temperatures.

A 2D, axisymmetric numerical finite-volume CFD model was developed to decouple the influence of mass transfer and intrinsic surface chemistry from the measured rates of oxidation. Using this model, kinetic expressions for the oxidation of Zn(g) by CO_2 and H_2O were developed. For CO_2, the oxidation is second-order, with a first order dependence on both Zn(g) and CO_2, as predicted from the law of mass action. Temperature dependence of the kinetic parameter is described in an Arrhenius expression with an activation energy of 44±3 kJ/mol and a pre-exponential factor of 92±6 mol cm^{-2} s^{-1} atm^{-2}. For H_2O splitting, the reaction rate data fit a second-order, law of mass action based kinetic expression. The temperature dependence of the kinetic parameter indicates, however, that the second-order model may not accurately represent the mechanistic details of Zn(g) oxidation by H_2O. The value of the kinetic parameter decreases from 199 mol cm^{-2} s^{-1} atm^{-2} at 800 K to 3.4 mol cm^{-2} s^{-1} atm^{-2} at 1050 K and increases to ~15 mol cm^{-2} s^{-1} atm^{-2} at 1100 K. This result is also reported in a prior study [61]. A precursor-type mechanism [109] was postulated to explain the nature of the temperature dependence of the kinetic parameter in the second-order model. Preliminary exploration of the model reveals the need for additional data to confirm or refute its deterministic capabilities.

The oxidation of Zn(g) by both H_2O and CO_2 is rapid, but the H_2O-splitting kinetics are more rapid than the CO_2-splitting kinetics. Comparing the measured rates of oxidation at 1100 K shows that the maximum measured rate of Zn(g) oxidation by H_2O is 10^{-5} mol cm^{-2} s^{-1}, three times that of the maximum measured rate of Zn(g) oxidation by CO_2, 0.32×10^{-5} mol cm^{-2} s^{-1}. Comparing the kinetic expressions is even more revealing. For identical gas compositions at 1100 K (Zn(g), H_2O, and CO_2 all at the Zn saturation pressure), H_2O oxidizes Zn(g) eighteen times faster than CO_2. The difference grows to a

factor of 100 at 800 K. The more rapid kinetics of H_2O-splitting might explain the so called "synergistic" effect reported in studies of the *simultaneous* splitting of H_2O and CO_2, where the rate of CO production is increased in the presence of water [45, 46].

The present study demonstrates that the heterogeneous oxidation of Zn(g) is a potentially revolutionary approach for H_2 and CO production in the Zn/ZnO solar thermochemical cycle, overcoming the kinetic constraint of Zn(ℓ,s) oxidation, and promising more efficient fuel production even when the latent energy of Zn vaporization is an additional energy requirement. Conventional approaches using polydisperse Zn(ℓ,s) aerosol reactors or packed beds of Zn(s) particles have been limited to converting 20% of Zn to ZnO for reaction times on the order of a minute [55, 56], and 80% of Zn to ZnO for reaction times on the order of tens of minutes [47, 48], respectively. The parametric thermodynamic analysis of Chapter 4 shows that the benefit of completely converting zinc via the heterogeneous oxidation of Zn(g) with reaction times on the order of seconds is an increase in cycle efficiency from 6–15% for Zn(ℓ,s) approaches to ~30% for the Zn(g) approach. The cycle efficiency could be as high as ~40% if heat recuperation is implemented.

7.1.2 The Oxidation of Ceria

High concentrations of accessible surface reaction sites are expected to increase the rate at which ceria oxidizes and reduces. In the present study, the oxidation of various porous ceria materials was compared with the oxidation of low porosity ceria. The objective was to demonstrate the benefit of templated porosity for achieving rapid ceria oxidation kinetics.

Two comparative experimental studies were completed. The model ceria material, to which the others were compared, was three-dimensionally ordered macroporous ceria (3DOM CeO_2), which contains an fcc lattice of interconnected pores, sub-μm solid feature

sizes, and a moderate specific surface area of 30–50 m^2 g^{-1}. In the first study, the oxidation of 3DOM CeO_2 was compared to the oxidation of non-ordered mesoporous and low porosity ceria. The ceria samples were oxidized at 1100 K with 3–4 mol% H_2O and CO_2, following a reduction with H_2. Three-dimensionally ordered macroporous CeO_2 produces H_2 and CO 2–3 times faster than the mesoporous and low porosity CeO_2. The maximum rate of H_2 and CO production over CeO_2 was 14 and 37 mL min^{-1} g^{-1}, and the maximum rate of H_2 and CO production over the alternative materials was 8 and 13 mL min^{-1} g^{-1}, and 6 and 10 mL min^{-1} g^{-1}, respectively. The alternative materials oxidized slower because of their low specific surface area, $\leq$ 1 m^2 g^{-1}, brought on by, in the case of the mesoporous ceria, thermally-induced sintering and associated grain growth. Sintering is a challenge for all porous materials subjected to high temperatures, e.g. [26, 122, 123, 133], and its effects are more severe at the temperatures at which ceria is thermally reduced.

Three-dimensionally ordered macroporous CeO_2 was subjected to higher temperatures in the second study, which compared the oxidation of 3DOM CeO_2 to non-ordered macroporous ceria (NOM CeO_2) and aggregates of ceria nanoparticles during thermochemical cycling. The ceria samples were thermally reduced over 78 s at ~1500 K under p_{O_2}=10^{-5} atm and oxidized over 120 s at ~1100 K by 25 mol% CO_2. 3DOM and NOM CeO_2 retained a disordered network of interconnected macropores over 50 cycles, and produced CO with a maximum rate of 6.4 mL min^{-1} g^{-1} for 3DOM CeO_2 and 4.0 mL min^{-1} g^{-1} for NOM CeO_2. Both the 3DOM and NOM CeO_2, produced CO an order of magnitude faster than the densely packed ceria nanoparticles and the limited porosity ceria, which produced CO at a rate less than 0.1 mL min^{-1} g^{-1}. The densely packed nanoparticles sinter significantly during thermochemical cycling, leading to inaccessible surface area that slows the rate of ceria oxidation. As a result of the rapid oxidation of 3DOM and NOM CeO_2 and the relatively slow oxidation of the alternative materials, the

3DOM and NOM CeO_2 produced ~1 mL g^{-1} of CO in a given cycle and the less porous ceria produced less than 0.1 mL g^{-1} of CO in a given cycle.

The present study reveals that, despite the effects of thermally-induced sintering which cause porous material to lose surface area (~50 to ~4 m^2 g^{-1} in the present study), ceria materials with templated porosity retain a morphology that allows for rapid rates of oxidation, ten times those of low porosity ceria materials. It is extremely advantageous to utilize such materials for solar thermochemical fuel production.

7.2 Future Direction

There are a number of interesting avenues for further research elucidated in the present study. First, the promise of the heterogeneous oxidation of Zn(g) for H_2 and CO production in the Zn/ZnO cycle warrants the design of a scaled-up reactor with the goal of rapid H_2 and CO production. The present study highlights the challenge of minimizing gas phase transfer in the reactor and provides the kinetic models to predict intrinsic surface reaction rates. The length scale for mass transfer in the Zn(g) oxidation experiments of Chapter 3 is 1.95 mm. To further mitigate mass transfer, the scaled-up Zn(g) oxidation reactor must feature shorter paths for diffusion. An intriguing approach is to use a fluidized bed of small ZnO particles. In addition to enhancing mass transfer, this approach would also address the practical challenges of recovering the ZnO product and achieving continuous oxidation. The ZnO particles in the fluidized bed would be removed for regeneration of Zn, and re-circulated for further fuel production.

In the present study of Zn(g) oxidation, it is hypothesized that oxidation proceeds via a precursor-type mechanism, in which adsorbed H_2O and Zn(g) react to form H_2. This mechanism provides a plausible physical explanation for the apparent negative activation energy of Zn(g) oxidation by H_2O between 800 and 1050 K. The proposed mechanism could be neither confirmed nor refuted in the present study conducted with H_2O partial

pressures less than 0.3 atm. As noted in Chapter 3, if the precursor mechanism models the kinetics of Zn(g) oxidation, the rate of oxidation becomes proportional to the partial pressure of Zn(g) with H_2O partial pressures closer to 1 atm. The constant of proportionality is the kinetic parameter associated with the rate-limiting step in the heterogeneous oxidation sequence. Experiments conducted over the 800 to 1050 K range with high concentrations of H_2O would test the precursor mechanism hypothesis, and permit the measurement of the rate-limiting kinetic parameter.

In the ceria-based solar thermochemical cycle, templated porosity is shown to make an order of magnitude difference in the rate of oxidation of ceria by H_2O and CO_2 (Chapter 6), with the enhanced kinetics attributed to the specific surface area and interconnected pore network of the templated architecture. The specific surface areas of the templated materials after thermochemical cycling are a factor of 10 less than prior to cycling (e.g, the specific surface area of 3DOM CeO_2 is ~50 m^2 g^{-1} before and 4 m^2 g^{-1} after cycling). It would be interesting to investigate the potential benefit of retaining more of the specific surface initially present in the templated materials. One approach to improve thermal stability, as noted in Chapter 5, is doping. Adding cations to ceria is known to enhance its thermal stability at temperatures of 1100 K [124]. With greater retention of specific surface area, even faster oxidation rates may be possible.

Bibliography

[1] Solomon, S., 2007, "Climate Change 2007 : the physical science basis : contribution of Working Group I to the Fourth Assessment Report of the Intergovernmental Panel on Climate Change," Cambridge University Press, Cambridge, New York, 996 pgs.

[2] Lewis, N. S., 2006, "Powering the Planet: Chemical Challenges in Solar Energy Utilization," Proceedings of the National Academy of Sciences of the United States of America, **103.43**, pp. 15729-15735.

[3] Noring, J. E., Diver, R. B., and Fletcher, E. A., 1981, "Hydrogen and Oxygen from Water. V. the ROC System," Energy, **6**, pp. 109-121.

[4] Diver, R. B., Pederson, S., Kappauf, T., 1983, "Hydrogen and Oxygen from Water. IV. Quenching the Effluent from a Solar Furnace," Energy, **8**, pp. 947-955.

[5] Lédé, J., Lapicque, F., and Villermaux, J., 1983, "Production of Hydrogen by Direct Thermal Decomposition of Water," Int. J. Hydrogen Energy, **8**, pp. 675-679.

[6] Scholl, K. L., and Fletcher, E. A., 1993, "Y_2O_3-Doped ZrO_2 Membranes for Solar Electrothermal and Solar Thermal Separations. II. Electron Hole Conductivity of Yttria-Stabilized Zirconia," Energy, **18**, pp. 69-74.

[7] Itoh, N., Sanchez, M. A., Xu, W., 1993, "Application of a Membrane Reactor System to Thermal Decomposition of CO_2," J. Membrane Sci., **77**, pp. 245-253.

[8] Kogan, A., 1997, "Direct Solar Thermal Splitting of Water and on Site Separation of the Products I. Theoretical Evaluation of Hydrogen Yield," Int. J. Hydrogen Energy, **22**, pp. 481-486.

[9] Kogan, A., 1998, "Direct Solar Thermal Splitting of Water and on-Site Separation of the Products II. Experimental Feasibility Study," Int. J. Hydrogen Energy, **23**, pp. 89-98.

[10] Kogan, A., Spiegler, E., and Wolfshtein, M., 2000, "Direct Solar Thermal Splitting of Water and on-Site Seperation of the Productions. III. Improvement of Reactor Efficiency by Steam Entrainment," Int. J. Hydrogen Energy, **25**, pp. 739-745.

[11] Jin, W., Zhang, C., Zhang, P., 2006, "Thermal Decomposition of Carbon Dioxide with POM in a Membrane Reactor," AIChE J., **52**, pp. 2545-2550.

[12] Ohta, T., 1979, "Solar-Hydrogen Energy Systems," Pergamon Press, Elmsford, New York.

[13] Funk, J. E., 2001, "Thermochemical Hydrogen Production: Past and Present," Int. J. Hydrogen Energy, **26**, pp. 185-190.

[14] Nakamura, T., 1977, "Hydrogen Production from Water Utilizing Solar Heat at High Temperatures," Sol. Energy, **19**, pp. 467-477.

[15] Tamaura, T., Steinfeld, A., Kuhn, P., 1995, "Production of Solar Hydrogen by a Novel, 2-Step Water-Splitting Thermochemical Cycle," Energy, **20**, pp. 325-330.

[16] Sturzenegger, M., and Nuesch, P., 1999, "Efficiency Analysis for a Manganese-Oxide-Based Thermochemical Cycle," Energy, **24**, pp. 959-970.

[17] Steinfeld, A., 2002, "Solar Hydrogen Production Via a Two-Step Water-Splitting Thermochemical Cycle Based on Zn=ZnO Redox Reactions," Int. J. Hydrogen Energy, **27**, pp. 611-619.

[18] Abanades, S., and Flamant, G., 2006, "Thermochemical Hydrogen Production from a Two-Step Solar-Driven Water-Splitting Cycle Based on Cerium Oxide," Sol. Energy, **80**, pp. 1611-1623.

[19] Allendorf, M., Diver, R. S.,N., and Miller, J., 2008, "Two-Step Water-Splitting using Mixed-Metal Ferrites: Thermodynamic Analysis and Characterization of Synthesized Materials," Energy Fuels, **22**, pp. 4115-4124.

[20] Roeb, M., Gathmann, N., Neises, M., 2009, "Thermodynamic Analysis of Two-Step Solar Water Splitting with Mixed Iron Oxides," Int. J. Energy Res., **33**(10), pp. 893-902.

[21] Abraham, B. M., and Schreiner, F., 1974, "General Principles Underlying Chemical Cycles which Thermally Decompose Water into the Elements," Ind. Eng. Chem. Fund., **13**, pp. 305-310.

[22] Steinfeld, A., Kuhn, P., Reller, A., 1998, "Solar-Processed Metals as Clean Energy Carriers and Water-Splitters," Int. J. Hydrogen Energy, **23**(9), pp. 767-774.

[23] Fletcher, E. A., 2001, "Solar Thermal Processing: A Review," J. Sol. Energy Eng., **123**, pp. 63-74.

[24] Steinfeld, A., 2005, "Solar Thermochemical Production of Hydrogen: A Review," Sol. Energy, **78**, pp. 603-615.

[25] Abanades, S., Charvin, P., Flamant, G., 2006, "Screening of Water-Splitting Thermochemical Cycles Potentially Attractive for Hydrogen Production Concentrated Solar Energy," Energy, **31**, pp. 2805-2822.

[26] Kodama, T., and Gokon, N., 2007, "Thermochemical Cycles for High-Temperature Solar Hydrogen Production," Chem. Rev., **107**(10), pp. 4048-4077.

[27] Perkins, C., and Weimer, A., 2009, "Solar-Thermal Production of Renewable Hydrogen," AIChE J., **55**, pp. 286-293.

[28] Meredig, B., and Wolverton, C., 2009, "First-Principles Thermodynamic Framework for the Evaluation of Thermochemical H_2O- Or CO_2-Splitting Materials," Phys. Rev. B, **80**, pp. 245119.

[29] Loutzenhiser, P. G., Stamatiou, A., Villasmil, W., 2011, "Concentrated Solar Energy for Thermochemically Producing Liquid Fuels from CO_2 and H_2O," JOM, **63**(1), pp. 32-4.

[30] Venstrom, L., Krueger, K., Leonard, N., 2009, "Solar Thermal Electrolytic Process for the Production of Zn from ZnO: An Ionic Conductivity Study," J. Sol. Energy Eng., **131**(3), pp. 031005 (9 pp.).

[31] Wieckert, C., Frommherz, U., Kraupl, S., 2007, "A 300 kW Solar Chemical Pilot Plant for the Carbothermic Production of Zinc," J. Sol. Energy Eng., **129**(2), pp. 190-196.

[32] Gstoehl, D., Brambilla, A., Schunk, L. O., 2008, "A Quenching Apparatus for the Gaseous Products of the Solar Thermal Dissociation of ZnO," J. Mat. Sci., **43**(14), pp. 4729-4736.

[33] Müller, R., and Steinfeld, A., 2008, "H_2O-Splitting Thermochemical Cycle Based on ZnO/Zn-Redox: Quenching the Effluents from the ZnO Dissociation," Chem. Eng. Sci., **63**, pp. 217-227.

[34] Fresno, F., Yoshida, T., Gokon, N., 2010, "Comparative Study of the Activity of Nickel Ferrites for Solar Hydrogen Production by Two-Step Thermochemical Cycles," Int. J. Hydrogen Energy, **35**(16), pp. 8503-10.

[35] Chueh, W. C., and Haile, S. M., 2010, "A Thermochemical Study of Ceria: Exploiting an Old Material for New Modes of Energy Conversion and CO_2 Mitigation," Phil. Trans. Royal Soc. London A, **368**, pp. 3269-94.

[36] Chueh, W. C., and Haile, S. M., 2009, "Ceria as a Thermochemical Reaction Medium for Selectively Generating Syngas Or Methane from H_2O and CO_2," ChemSusChem, **2**(8), pp. 735-739.

[37] Lapp, J., Davidson, J. H., and Lipiński, W., 2012, "Efficiency of Two-Step Solar Thermochemical Non-Stoichiometric Redox Cycles with heat Recovery," Energy, **37**(1), pp. 591-600.

[38] Diver, R. B., Miller, J. E., and Allendord, M. D., 2008, "Solar Thermochemical Water-Splitting Ferrite-Cycle Heat Engines," J. Sol. Energy Eng., **130**(4), pp. 041001.

[39] Bazan, J. C., Gschaider, M. E., and Alimenti, G. A., 1999, "Gravimetric Study of Interaction of Water Vapour with Metallic Zinc," J. Thermal Analysis Calorimetry, **55**, pp. 569-579.

[40] Alimenti, G. A., Gschaider, M. E., Bazan, J. C., 2004, "Theoretical and Experimental Study of the Interaction of O_2 and H_2O with Metallic Zinc - Discussion of the Initial Step of Oxide Formation," J. Colloid Interface Sci., **276**(1), pp. 24-39.

[41] Vishnevetsky, I., and Epstein, M., 2007, "Production of Hydrogen from Solar Zinc in Steam Atmosphere," Int. J. Hydrogen Energy, **32**, pp. 2791-2802.

[42] Funke, H. H., Diaz, H., Liang, X., 2008, "Hydrogen Generation Hydrolysis of Zinc Power Aerosol," Int. J. Hydrogen Energy, **33**, pp. 1127-1134.

[43] Loutzenhiser, P. G., Galvez, M. E., Hischier, I., 2009, "CO_2 Splitting Via Two-Step Solar Thermochemical Cycles with Zn/ZnO and FeO/Fe_3O_4 Redox Reactions II: Kinetic Analysis," Energy Fuels, **23**(5), pp. 2832-2839.

[44] Ernst, F. O., Steinfeld, A., and Pratsinis, S. E., 2009, "Hydrolysis Rate of Submicron Zn Particles for Solar H_2 Synthesis," Int. J. Hydrogen Energy, **34**, pp. 1166-1175.

[45] Stamatiou, A., Loutzenhiser, P. G., and Steinfeld, A., 2010, "Solar Syngas Production Via H_2O/CO_2-Splitting Thermochemical Cycles with Zn/ZnO and FeO/Fe_3O_4 Redox Reactions," Chem. Mat., **22**(3), pp. 851-859.

[46] Stamatiou, A., Loutzenhiser, P. G., and Steinfeld, A., 2010, "Solar Syngas Production from H_2O and CO_2 Via Two-Step Thermochemical Cycles Based on Zn/ZnO and FeO/Fe_3O_4 Redox Reactions: Kinetic Analysis," Energy Fuels, **24**, pp. 2716-2722.

[47] Loutzenhiser, P. G., Barthel, F., Stamatiou, A., 2011, "CO_2 Reduction with Zn Particles in a Packed-Bed Reactor," AIChE J., **57**(9), pp. 2529-2534.

[48] Stamatiou, A., Loutzenhiser, P. G., and Steinfeld, A., 2012, "Syngas Production from H_2O and CO_2 Over Zn Particles in a Packed-Bed Reactor," AIChE J., **58**(2), pp. 625-631.

[49] Weiss, R. J., Ly, H. C., Wegner, K., 2005, "H_2 Production Zn Hydrolysis in a Hot-Wall Aerosol Reactor," AIChE: Particle Technology and Fluidization, **51**(7), pp. 1966-1970.

[50] Wegner, K., Ly, H. C., Weiss, R. J., 2006, "In Situ Formation and Hydrolysis of Zn Nanoparticles for H_2 Production 2-Step ZnO/Zn Water-Splitting Thermochemical Cycle," Int. J. Hydrogen Energy, **31**, pp. 55-61.

[51] Ernst, F. O., Tricoli, A. Pratsinis, S. E., Steinfeld, A., 2006, "Co-Synthesis of H_2 and ZnO by In-Situ Zn Aerosol Formation and Hydrolysis," AIChE J., **52**(9), pp. 3297-3303.

[52] Abu Hamed, T., Davidson, J.H., and Haltiwanger, J., 2007, "Hydrogen Production via Hydrolysis of Zinc Nanoparticles," AIChE 2007 Annual Meeting, Salt Lake City, Utah, November 2007.

[53] Hamed, T. A., Davidson, J. H., and Stolzenburg, M., 2008, "Hydrolysis of evaporated Zn in a hot wall flow reactor," J. Sol. Energy Eng., **130**, pp. 0410101-0410107.

[54] Abu Hamed, T., Venstrom, L., Alshare, A., 2009, "Study of a Quench Device for the Synthesis and Hydrolysis of Zn Nanoparticles: Modeling and Experiments," J. Sol. Energy Eng., **131**(3), pp. 031018 (9 pp.).

[55] Melchior, T., Piatkowski, N., and Steinfeld, A., 2009, "H_2 Production Steam-Quenching of Zn Vapor in a Hot-Wall Aerosol Flow Reactor," Chem. Eng. Sci., **64**, pp. 1095-1101.

[56] Loutzenhiser, P. G., Galvez, M. E., Hischier, I., 2010, "CO_2 Splitting in an Aerosol Flow Reactor Via the Two-Step Zn/ZnO Solar Thermochemical Cycle," Chem. Eng. Sci., **65**(5), pp. 1855-64.

[57] Ma, X., and Zachariah, M. R., 2009, "Oxidation Anisotropy and Size-Dependent Reaction Kinetics of Zinc Nanocrystals," J. Phys. Chem. C, **113**(33), pp. 14644-14650.

[58] Haltiwanger, J. F., 2011, "Zinc Aerosol Hydrolysis in a Transverse Jet Reactor," Ph.D. Dissertation, University of Minnesota-Twin Cities.

[59] Clarke, J. A., and Fray, D. J., 1975, "Oxidation Kinetics of Zinc Vapour," Conference Proceedings, High Temperature Chemical Reaction Engineering, I. Chem. E. Symposium Series No. 43.

[60] Clarke, J. A., and Fray, D. J., 1978, "The Rate of Deposition and the Morphology of Zinc Oxide Deposited from Zn(v)/CO/CO_2/Ar Gas Mixtures," J. Mater. Sci., **13**, pp. 1921-1925.

[61] Clarke, J. A., and Fray, D. J., 1979, "Oxidation of Zinc Vapour Hydrogen-Water Vapour Mixtures," Trans. Inst. Min. Metall. C, **88**, pp. C161-C166.

[62] Clarke, J. A., 1979, "Zinc Oxidation and its Implications in the Imperial Smelting Furnace," Chem. Ind., **6**, pp. 5-10.

[63] Lewis, L. A., and Cameron, A. M., 1995, "Oxidation Kinetics of Zinc Vapor in CO:CO_2 Mixtures: Part I. Comparison with Past Literature," Metall. Mater. Trans. B, **26B**, pp. 911-918.

[64] Lewis, L. A., and Cameron, A., 1995, "Oxidation Kinetics of Zinc Vapor in CO:CO_2 Mixtures: Part II. Application of Plug Flow Concepts," Metall. Mater. Trans. B, **26B**, pp. 919-924.

[65] Cox, A., and Fray, D. J., 2000, "Zinc Reoxidation in the Shaft of a Zinc-Lead Imperial Smelting Furnace-2: Zinc-Carbon-Oxygen System in Combination with Sinter and Coke Substrates," Trans. Inst. Min. Metall. C, **109**, p. C111.

[66] Cox, A., and Fray, D. J., 2000, "Zinc Reoxidation in the Shaft of a Zinc-Lead Imperial Smelting Furnace-1: Zinc-Carbon-Oxygen System with Deposition Initiated on a Quartz

Substrate and Subsequent Propagation on Zinc Oxide," Trans. Inst. Min. Metall. C, **109**, pp. C104.

[67] Osborne, J. M., Rankin, W. J., McCarthy, D. J., 2001, "The Oxidation of Zinc Vapour in CO-CO_2-N_2 Gas Mixtures," Metall. Mater. Trans. B, **32B**, pp. 37-45.

[68] Cox, A., and Fray, D. J., 2003, "The Kinetics of the Oxidation of Zinc Vapour Carbon Dioxide and Water Vapour on Quartz, Zinc Oxide, Sinter and Coke Substrates," Metall. Mater. Proc.: Principles and Technologies, **1**, pp. 95-105.

[69] Lewis, L. A., 1992, "Oxidation kinetics of zinc vapour," Ph.D. Dissertation, University of Manchester.

[70] Davis, M.E., and Davis, R.J., 2002, "Fundamentals of Chemical Reaction Engineering," McGraw-Hill Science/Engineering/Math, pp. 384.

[71] Levenspiel, O., "Chemical reaction engineering," Wiley, New York, pp. 501.

[72] Chueh, W. C., Falter, C., Abbott, M., 2010, "High-Flux Solar-Driven Thermochemical Dissociation of CO_2 and H_2O using Non-stoichiometric Ceria," Science, **330**, pp. 1797-801.

[73] Furler, P., Scheffe, J. R., and Steinfeld, A., 2012, "Syngas Production by Simultaneous Splitting of H_2O and CO_2 via Ceria Redox Reactions in a High-Temperature Solar Reactor," Energy Env. Sci., **5**(3), pp. 6098-6103.

[74] Sokolov, S., Bell, D., and Stein, A., 2003, "Preparation and Characterization of Macroporous α-Alumina," J. Am. Ceram. Soc., **86**, pp. 1481-1486.

[75] Stein, A., Li, F., and Denny, N. R., 2008, "Morphological Control in Colloidal Crystal Templating of Inverse Opals, Hierarchical Structures and Shaped Particles," Chem. Mater., **20**(3), pp. 649-666.

[76] Roine, A., Outokumpu HSC Chemistry for Windows , v7.0, Outokumpu Research, Pori, Finland.

[77] Porter, F.C., 1991, "Zinc handbook: properties, processing, and use in design," CRC Press, New York, pp. 648.

[78] Wagner, C., 1933, "Beitrag Zur Theorie Des Anlaufvorgangs," Z. Phys. Chem. B, **21**, pp. 25-41.

[79] Cabrera, N., and Mott, N. F., 1948, "Theory of the Oxidation of Metals," Reports on Progress in Physics, **12**, pp. 163-184.

[80] Morin, F., Beranger, G., and Lacombe, P., 1972, "Limits of Application for Wagner's Oxidation Theory," Oxidation of Metals, **4**, pp. 51-62.

[81] Mrowee, S., and Stokisa, A., 1973, "Discussion of 'Limits of Application for Wagner's Oxidation Theory'," Oxidation of Metals, **7**, pp.

[82] Berman, A., and Epstein, M., 2000, "The Kinetics of Hydrogen Production in the Oxidation of Liquid Zinc with Water Vapor," Int. J. Hydrogen Energy, **25**, pp. 957-967.

[83] Delalu, H., Vingalou, J., Elkhatib, M., 2000, "Kinetics and Modeling of Diffusion Phenomena Occurring during the Complete Oxidation of Zinc Powder: Influence of Granulometry, Temperature, and Relative Humidity of the Oxidizing Fluid," Solid State Sciences, **2**, pp. 2.

[84] Lv, M., Zhou, J., Yang, W., 2010, "Thermogravimetric Analysis of the Hydrolysis of Zinc Particles," Int. J. Hydrogen Energy, **35**(7), pp. 2617-2621.

[85] Park, K., Lee, D., Rai, A., 2005, "Size-Resolved Kinetic Measurements of Aluminum Nanoparticle Oxidation with Single Particle Mass Spectrometry," J. Phys. Chem., **109**(15), pp. 7290-7299.

[86] Rai, A., Park, K., Zhou, L., 2006, "Understanding the Mechanism of Aluminium Nanoparticle Oxidation," Combustion Theory and Modeling, **10**(5), pp. 843-859.

[87] Haltiwanger, J. F., Venstrom, L. J., and Davidson, J. H., 2009, "A Discussion of the Measurement of Zn to ZnO Conversion in Aerosol Reactors," ASME 3rd International Conference on Energy Sustainability, ES2009, July 19, 2009 - July 23, San Francisco, CA, United states, **2,** pp. 483-489.

[88] Palumbo, R., Léde, J., Boutin, O., 1998, "The Production of Zn from ZnO in a High-Temperature Solar Decomposition Quench Process--I the Scientific Framework for the Process," Chem. Eng. Sci., **53**, pp. 2503-2517.

[89] Watson, L. R., Theim, T. L., Dressler, R. A., 1993, "High Temperature Mass Spectrometric Studies of the Bond Energies of Gas Phase ZnO, NiO, and Cuo," J. Phys. Chem., **97**, pp. 5577-5580.

[90] Weidenkaff, A., Steinfeld, A., Wokaun, A., 1999, "Direct Solar Thermal Dissociation of Zinc Oxide: Condensation and Crystallization of Zinc in the Presence of Oxygen," Sol. Energy, **65**(1), pp. 59-69.

[91] Weidenkaff, A., Rellera, A. W., Wokaunb, A., 2000, "Thermogravimetric Analysis of the ZnO/Zn Water Splitting Cycle," Thermochemica Acta, **359**, pp. 69-75.

[92] Weidenakff, A., Reller, A., Sibieude, F., 2000, "Experimental Investigations on the Crystallization of Zinc: Direct Irradiation of Zinc Oxide in a Solar Furnace," Chem. Mater., **12**, pp. 2175-2181.

[93] Keunecke, M., Meier, A., and Palumbo, R., 2004, "Solar Thermal Decomposition of Zinc Oxide: An Initial Investigation of the Recombination Reaction in the Temperature Range 1100-1250 K," Chem. Eng. Sci., **59**, pp. 727-744.

[94] Stott, J. V., and Fray, D. J., 1971, "Oxidation of Zinc Vapour," *Advances in extractive metallurgy and refining*, Inst. Min. Metall., London, pp. 95-105.

[95] Leonard, R. L., 1985, "Oxidation Kinetics of Zinc Vapor in Zn-CO_2-CO Gas Mixtures," MS Thesis, Colorado School of Mines.

[96] Stansbury, K. L., 1987, "An Experimental Study of the Oxidation of Zinc Vapor," MS Thesis, Colorado School of Mines.

[97] Yaws, C.L., 2007, "The Yaws handbook of vapor pressure: Antoine coefficients," Houston, Tex. : Gulf Pub, Houston, Tex.

[98] Dell'Amico, M., and See, J. B., 1987, "Accretion reduction in the offtake of the Imperial Smelting Furnace," Pyrometallurgy '87, Anonymous Inst. Min. Metall., London, UK, pp. 305-346.

[99] Patankar, S.V., 1980, "Numerical heat transfer and fluid flow," McGraw-Hill, New York, pp. 197.

[100] Date, A.W., 2005, "Introduction to computational fluid dynamics," Cambridge University Press, New York, pp. 377.

[101] Yaws, C., 2010, "Yaws' transport properties of chemicals and hydrocarbons," Knovel.

[102] Mills, A.F., 2001, "Mass transfer," Prentice Hall, pp. 420.

[103] Turkdogan, E. T., 1965, "Diffusivities of Gases and Metal Vapours at Elevated Temperatures," Steelmaking: the Chipman conference, J. F. Elliott and T. R. Meadowcroft, eds., M.I.T. Press, Cambridge, Mass., pp. 77-87.

[104] Krishna, R., and Wesselingh, J. A., 1997, "The Maxwell-Stefan Approach to Mass Transfer," Chem. Eng. Sci., **52**(6), pp. 861-911.

[105] Wetter, M., 2011, "GenOpt: Generic Optimization Program," Lawrence Berkeley National Laboratory, **3.1.0**.

[106] Jones, A. C., Leedham, T. J., Wright, P. J., 1998, "Synthesis and Characterisation of Two Novel Titanium Isopropoxides Stabilised with a Chelating Alkoxide: Their use in the Liquid Injection MOCVD of Titanium Dioxide Thin Films," J. Mater. Chem., **8**, pp. 1773-1777.

[107] Kang, B., Lee, S., and Boo, J., 2000, "Growth of TiO_2 Thin Films on Si(100) Substrates using Single Molecular Precursors by Metal Organic Chemical Vapor Deposition," Surface and Coatings Technology, **131**(1-3), pp. 88-92.

[108] Wei, J., 1996, "Adsorption and Cracing of n-Alkanes Over ZSM-5: Negative Activation Energy of Reaction," Chem. Eng. Sci., **51**(11), pp. 2995-2999.

[109] Masel, R.I., 2001, "Chemical Kinetics and Catalysis," Wiley-Interscience, pp. 952.

[110] Nagao, K., Yunoki, H., Muraishi, H., 1978, "Differential Heat of Chemisorption. 1. Chemisorption of Water on Zinc Oxide and Titanium Oxide," J. Phys. Chem., **82**(9), pp. 1032-1035.

[111] Nagao, M., Kiriki, M., Muraishi, H., 1978, "Differential Heat of Chemisorption. 2. Chemisorption of Carbon Dioxide and Amonia on Zinc Oxide," J. Phys. Chem., **82**(24), pp. 2561-2563.

[112] Loutzenhiser, P. G., Meier, A., and Steinfeld, A., 2010, "Review of the Two-Step H_2O/CO_2-Splitting Solar Thermochemical Cycle Based on Zn/ZnO Redox Reactions," Materials, **3**(11), pp. 4922.

[113] Venstrom, L. J., and Davidson, J. H., 2011, "Splitting Water and Carbon Dioxide Via the Heterogeneous Oxidation of Zinc Vapor: Thermodynamic Considerations," J. Sol. Energy Eng., **133**(1), pp. 011017 (8 pp.).

[114] Galvez, M. E., Loutzenhiser, P. G., Hischier, I., 2008, "CO2 Splitting Via Two-Step Solar Thermochemical Cycles with Zn/ZnO and FeO/Fe3O4 Redox Reactions: Thermodynamic Analysis," Energy Fuels, **22**(5), pp. 3544-3550.

[115] Charvin, P., Abanades, S., Florent, L., Flamant, G., 2008, "Analysis of Solar Chemical Processes for Hydrogen Production from Water Splitting Thermochemical Cycles," Energy Conversion and Management, **49**, pp. 1547-1556.

[116] Mogensen, M., Sammes, N. M., and Tompsett, G. A., 2000, "Physical, Chemical and Electrochemical Properties of Pure and Doped Ceria," Solid State Ionics, **129**, pp. 63-94.

[117] Panlener, R. J., Blumenthal, R. N., and Garnier, J. E., 1975, "A Thermodynamic Study of Nonstoichiometric Cerium Dioxide," J. Phys. Chem. Solids, **3611**, pp. 1213-1222.

[118] Kaneko, H., Miura, T., Ishihara, H., 2007, "Reactive Ceramics of CeO_2-MO_x (M=Mn, Fe, Ni, Cu) for H_2 Generation by Two-Step Water Splitting using Concentrated Solar Thermal Energy," Energy, **32**(5), pp. 656-663.

[119] Kaneko, H., Ishihara, H., Taku, S., 2008, "Cerium Ion Redox System in CeO2-xFe2O3 Solid Solution at High Temperatures (1,273-1,673 K) in the Two-Step Water-Splitting Reaction for Solar H2 Generation," J. Mater. Sci., **43**(9), pp. 3153-61.

[120] Kaneko, H., and Tamaura, Y., 2009, "Reactivity and XAFS Study on (1-x)CeO_2-xNiO (x = 0.025-0.3) System in the Two-Step Water-Splitting Reaction for Solar H2 Production," J. Phys. Chem. Solids, **70**(6), pp. 1008-14.

[121] Abanades, S., Legal, A., Cordier, A., 2010, "Investigation of Reactive Cerium-Based Oxides for H_2 Production by Thermochemical Two-Step Water-Splitting," J. Mater. Sci., **45**, pp. 4163-4173.

[122] Le Gal, A., Abanades, S., and Flamant, G., 2011, "CO_2 and H_2O Splitting for Thermochemical Production of Solar Fuels using Nonstoichiometric Ceria and ceria/zirconia Solid Solutions," Energy Fuels, **25**(10), pp. 4836-4845.

[123] Le Gal, A., and Abanades, S., 2011, "Catalytic Investigation of Ceria-Zirconia Solid Solutions for Solar Hydrogen Production," Int. J. Hydrogen Energy, **36**(8), pp. 4739-48.

[124] Petkovich, N. D., Rudisill, S. G., Venstrom, L. J., 2011, "Control of Heterogeneity in Nanostructured $Ce_{1-x}Zr_xO_2$ Binary Oxides for Enhanced Thermal Stability and Water Splitting Activity," J. Phys. Chem. C, **115**(43), pp. 21022-21033.

[125] Scheffe, J. R., and Steinfeld, A., 2012, "Thermodynamic Analysis of Cerium-Based Oxides for Solar Thermochemical Fuel Production," Energy Fuels, **26**(3), pp. 1928-1936.

[126] Balducci, G., Islam, M. S., Kašpar, J., 2000, "Bulk Reduction and Oxygen Migration in the Ceria-Based Oxides," Chem. Mater., **12**, pp. 677-681.

[127] Mamontov, E., Egami, T., Brezny, R., 2000, "Lattice Defects and Oxygen Storage Capacity of Nanocrystalline Ceria and Ceria-Zirconia," J. Phys. Chem. B, **104**, pp. 111110-111116.

[128] Shah, P. R., Kim, T., Zhou, G., 2006, "Evidence for Entropy Effects in the Reduction of Ceria-Zirconia Solutions," Chem. Mater., **18**, pp. 5363-5369.

[129] Kim, T., Vohs, J. M., and Gorte, R. J., 2006, "Thermodynamics Investigation of the Redox Properties of Ceria-Zirconia Solid Solutions," Ind. Eng. Chem. Res., **45**, pp. 5561-5565.

[130] Colón, g., Pijolat, M., Valdivieso, F., 1998, "Surface and Structural Characterization of $Ce_xZr_{1-x}O_2$ CEZIRENCAT Mixed Oxides as Potential Three-Way Catalyst Promoters," J. Chem. Soc., Faraday Trans., **94**, pp. 3717-3726.

[131] Colón, G., Valdivieso, F., Pijolat, M., 1999, "Textural and Phase Stability of $Ce_xZr_{1-x}O_2$ Mixed Oxides Under High Temperature Oxidizing Conditions," Catal. Today, **50**, pp. 271-284.

[132] Giordano, F., Trovarelli, A., de Leitenburg, C., 2001, "Some Insight into the Effects of Oxygen Diffusion in the Reduction Kinetics of Ceria," Ind. Eng. Chem. Res., **40**, pp. 4828-4835.

[133] Miller, J. E., Allendorf, M. D., Diver, R. B., 2008, "Metal Oxide Composites and Structures for Ultra-High Temperature Solar Thermochemical Cycles," J. Mater. Sci., **43**, pp. 4714-4728.

[134] Lai, W., and Haile, S. M., 2005, "Impedance Spectroscopy as a Tool for Chemical and Electrochemical Analysis of Mixed Conductors: A Case Study of Ceria," J. Am. Ceram. Soc., **88**(11), pp. 2979-2997.

[135] Tuller, H. L., and Nowick, A. S., 1977, "Small Polaron Electron Transport in Reduced CeO_2 Single Crystals," J. Phys. Chem. Solids, **38**, pp. 859-867.

[136] Wang, S., Kobayashi, T., Dokiya, M., 2000, "Electrical and Ionic Conductivity of Gd-Doped Ceria," J. Electrochem. Soc., **147**(10), pp. 3606-3609.

[137] Incropera, F.P., and Dewitt, D.P., 2001, "Introduction to Heat Transfer," John Wiley & Sons, New York.

[138] Trovarelli, A., 2002, "Catalysis by Ceria and Related Materials," Imperial College Press, London, pp. 15-49.

[139] Petkovich, N.D., and Stein, A., 2012, "Hierarchically Structured Porous Materials: From Nanoscience to Catalysis, Separation, Optics, Energy, and Life Science," Wiley-VCH, Weinheim, Germany, pp. 55-130.

[140] Venstrom, L. J., Petkovich, N., Rudisill, S., 2012, "The Effects of Morphology on the Oxidation of Ceria by Water and Carbon Dioxide," J. Sol. Energy Eng., **134**(1), pp. 011005 (8 pp.).

[141] Umeda, G. A., Chueh, W. C., Noailles, L., 2008, "Inverse Opal Ceria-Zirconia: Architectural Engineering for Heterogeneous Catalysis," Energy Environ. Sci., **1**(4), pp. 484-6.

[142] Zhang, G., Zhao, Z., Liu, J., 2010, "Three Dimensionally Ordered Macroporous $Ce_{1-x}Zr_xO_2$ Solid Solutions for Diesel Soot Combustion," Chem. Comm., **46**, pp. 457-459.

[143] Wei, Y., Liu, J., Zhao, Z., 2011, "Highly Active Catalysts of Gold Nanoparticles Supported on Three-Dimensionally Ordered Macroporous $LaFeO_3$ for Soot Oxidation," Angew. Chem. Int. Ed., **50**(10), pp. 2326-2329.

[144] Liu, Y., Dai, H., Du, Y., 2012, "Controlled Preparation and High Catalytic Performance of Three-Dimensionally Ordered Macroporous $LaMnO_3$ with Nanovoid Skeletons for the Combustion of Toluene," J. Catal., **287**, pp. 149-160.

[145] Figliola, R.S., and Beasley, D.E., 2000, "Theory and Design for Mechanical Measurements," John Wiley & Sons, Hoboken, NJ, pp. 536.

[146] Ghia, U., Ghia, K. N., and Shin, C. T., 1982, "High-Re Solutions for Incompressible Flow using the Navier-Stokes Equations and a Multigrid Method," J. Comp. Phys., **48**, pp. 387-411.

[147] Steinfeld, A., and Palumbo, R., 2001, "Solar Thermochemical Process Technology" Encyclopedia of Physical Science & Technology," Meier, A., ed., pp. 237-256.

[148] Lovegrove, K., and Luzzi, A., 2001, "Solar Thermal Power Systems" Encyclopedia of Physical Science & Technology," Meier, A., ed., pp. .

Appendix A Uncertainty Analyses and Calibrations

In this appendix, I discuss the accuracy of the measurements in the Zn(g) oxidation and $CeO_{2-\delta}$ oxidation experiments, including a brief description of calibration techniques, where appropriate. First, I provide a list of all measurement instrumentation and the manufacturer reported accuracy. If calibration of the instrument was required, I describe the technique and accuracy. The sequential perturbation method for estimating measurement uncertainty is used to propagate measurement uncertainty, and the uncertainty estimated for the primary measured quantities is presented and discussed.

A list of instrumentation is provided in Table A-1, and includes mass flow controllers, a primary standard volumetric flow meter, gas composition analyzers, a digital mass balance, Pt-Pt/Rh (Type-R) and Chromel-Alumel (Type-K) thermocouple based temperature sensors, calipers, and a length scale. Mass flow controllers are used to control the rate of delivery of gases to the reactors. The precision of the flow controllers is 0.1% FSR. Additionally, the flow controllers are calibrated to maximize accuracy using a Sensidyne Gilibrator 2 volumetric flow meter, a primary flow standard that operates using first principles. The Gilibrator 2 measures the time required for a gas flow to displace a known volume, and is accurate to within ± 1% of the measured flow rate. The volumetric flow measurement is converted to mass flow using the ideal gas state equation and the barometric pressure and ambient temperature, both measured on the day of an experiment.

Gas composition is measured with either a quadrupole mass spectrometer (Inficon Transpector CPM) or a Raman laser gas analyzer (Atmosphere Recovery Inc., RLGA 129a). The mass spectrometer charges molecules in a gas sample using a high-voltage ionization source, and then separates the molecules in the mixture based on their mass-to-charge ratio. Charged molecules are accelerated down a cylindrical chamber

Table A-1 List of instrumentation used in the present study, the quantity measured, and the accuracy.

Instrument	Measurand	Accuracy
Hastings 202 MFC, 100 mL min^{-1} FSR	CO_2 gas flow rate	± 1% [a]
MKS 1153A MFC, 500 mL min^{-1} FSR	H_2O(g) flow rate	± 5 cc/min[b,c]
MKS 1179 MFC, 250 mL min^{-1} FSR	Ar/CO_2 flow rate	± 1% [a]
MKS 2179 MFC, 5000 mL min^{-1} FSR	Ar flow rate	± 1% [a]
Inficon Transpector CPM Mass Spectrometer	H_2 concentration	± 2% [a]
Atmosphere Recovery, Inc. Raman laser gas analyzer 129a	O_2, H_2, and CO concentration	± 0.02 mol% [a]
Sartorius GD-503-NTEP Balance	mass	± 0.0001 g [c]
Chromel-Alumel Thermocouple in steel sheath	temperature	± 1 K [d]
Pt-Pt/Rh Thermocouple in Alumina Sheath	temperature	± 3 K [d]
Calipers	tube i.d.	± 0.01 mm
Ruler	length	± 0.5 mm

[a] based on calibration described in this appendix

[b] assuming H_2O is an ideal gas at $T = 273$ K, $p = 1$ atm

[c] reported by manufacturer

[d] NIST standard bias errors

and subjected to a transverse electric field which forces all molecules except those with a single mass-to-charge ratio to the walls of the chamber. The molecules that are not forced to the wall pass through the chamber and are detected using a Faraday cup, which generates a current proportional to the flux of molecules. The mass spectrometer features high sensitivity, with the ability to detect gases at concentrations of 5 ppm. It is susceptible to fragmentation errors. Ionization of molecules can be energetic enough to break molecular bonds, converting, for example, CO_2 into CO and O. Fragmentation makes measurements of mixtures of like compounds challenging. In the CO_2-splitting experiments, CO_2 is often present at higher concentrations than CO, such that the CO signal in the mass spectrometer cannot be accurately differentiated from the fragmented CO_2 signal. Consequently, the Raman laser gas analyzer is used for CO_2-splitting experiments.

The mass spectrometer is calibrated using a H_2-Ar standard mixture. The standard mixture contains 4.97±0.05 mol% H_2, and is mixed with grade 5.0 purity Ar (99.999%) to obtain lower concentrations. The gases are mixed using the previously described mass flow controllers. The concentration of H_2 is correlated to the ratio of the signal strength of the H_2 ($i_{m/z=2}$) and Ar^{36} isotope ($i_{m/z=36}$), as shown in Figure A-1. Note that the instrument is not linear. The accuracy of the mass spectrometer is ±2% of the measured concentration of H_2.

The Raman laser gas analyzer detects H_2, CO_2, CO, or O_2 based on their visible light scattering signatures. A yellow Helium-Neon laser (wavelength 632 nm) is directed through the sampled gas. Each molecule in the gas shifts the color (wavelength, or energy) of the laser light differently, and a series of filters, lenses, and photodiodes detect the number of photons shifted into a given color. The number of photons shifted is proportional to the concentration of the molecule in the gas. Similar to the mass spectrometer, the Raman

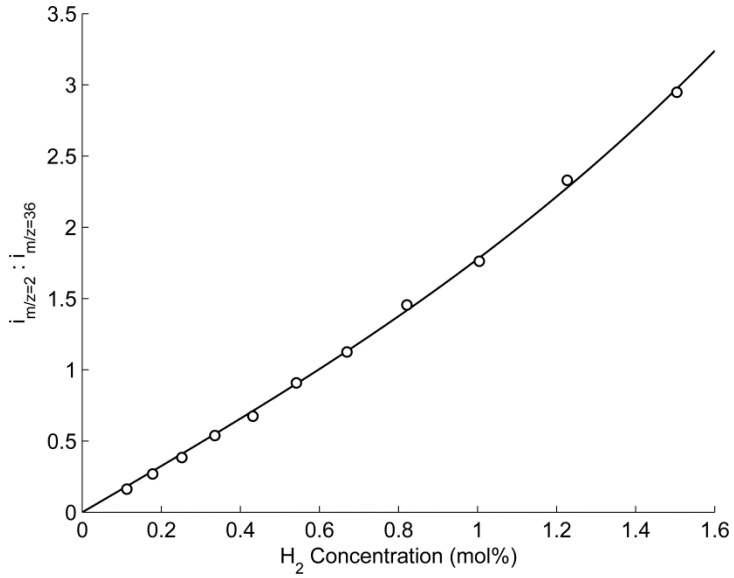

Figure A-1 Calibration curve for measuring H_2 with the quadrupole mass spectrometer.

laser gas analyzer is calibrated using mixtures of a solute (H_2, CO, O_2) diluted with grade 5.0 purity Ar. The mixture compositions are set using mass flow controllers. The calibration curve is stored internally in the software of the instrument, and the accuracy is better than ± 0.02 mol%.

The sequential perturbation method is used to propagate measurement uncertainty to the experimental results (Zn(g) oxidation rate, H_2/CO production rate, etc.). The essence of the method is to treat the data analysis as a "black box" routine that accepts measured variables and calculates the desired results. The "black box" routine is utilized multiple times. First, the nominal values of the desired results, $\vec{R}_{\text{nom}}$, are calculated using the nominal values of the measured variables, x_i.

$$\vec{R}_{\text{nom}} = f(x_1, x_2, x_3, \ldots x_i, \ldots x_{\text{N}}) \tag{A.1}$$

The measured variables are then sequentially perturbed by their measurement uncertainty and the "black box" routine run for each new value of the perturbed variable. The output of the "black box" routine includes the influence of the accuracy of the measured variable on the desired results, which have values perturbed away from the nominal results.

$$\vec{R}_{\mathrm{i}}^{+} = f(x_1, x_2, x_3, \ldots x_{\mathrm{i}} + \mu_{\mathrm{i}}, \ldots x_{\mathrm{N}}) \tag{A.2}$$

The difference between the nominal results and the perturbed results is the estimate of the uncertainty:

$$\mu_{\mathrm{R,i}}^{+} = \vec{R}_{\mathrm{nom}} - \vec{R}_{\mathrm{i}}^{+} \tag{A.3}$$

The process defined by equations (A.2) and (A.3) is for when measured variables are perturbed by adding the measurement uncertainty. This process is repeated perturbing the measured variables by subtracting the measurement uncertainty:

$$\vec{R}_{\mathrm{p,i}}^{-} = f(x_1, x_2, x_3, \ldots x_i - \mu_i, \ldots x_{\mathrm{N}}) \tag{A.4}$$

The overall uncertainty is then the root-sum-square of the average of the collection of uncertainty estimates.

$$\mu_R = \sqrt{\sum_{\mathrm{i}} \left(\frac{1}{2} \left(\mu_{\mathrm{R,i}}^{+} + \mu_{\mathrm{R,i}}^{-} \right) \right)^2} \tag{A.5}$$

Additional details of the sequential perturbation method are provided in Ref. [145].

The uncertainty is dependent on the magnitude of the result. Some typical values are shown in Table A-2.

Table A-2 Typical values for key results and their associated uncertainty estimated using the sequential perturbation method.

Result	Nominal Value	Uncertainty
Max. rate of H_2 production over 3DOM CeO_2 during isothermal chemical cycling	13.6 mL min^{-1} g^{-1}	±0.4 mL min^{-1} g^{-1}
Total volume of H_2 or CO produced over 3DOM CeO_2 during thermochemical cycling	0.9 mL g^{-1}	±0.1 mL g^{-1}
Heterogeneous Zn(g) oxidation rate at z = 24 mm in CO_2-splitting at T = 1150 K	3.8×10^{-6} mol cm^{-2} s^{-1}	$\pm0.3\times10^{-6}$ mol cm^{-2} s^{-1}
Steady rate of CO production during splitting of CO_2 by Zn(g) oxidation at T = 1100 K	1.05 mmol/min	±0.07 mmol/min

Appendix B Fully-developed velocity profile in an annulus

The mass flow inlet boundary condition at the annular Zn inlet in the 2D model for mass transfer and surface chemistry used in Part II features a fully-developed velocity profile. The equation for the velocity profile is given in equation (3.22), but the parameter F was left undefined. This parameter is developed in standard fluid mechanics textbooks, e.g., Munson *et al.* (2012). F has the units of pressure drop, and is related to a friction factor, f.

$$F = f\frac{\rho U_{\mathrm{Zn}}^2}{2d_{\mathrm{h}}} \tag{B.1}$$

For laminar flow, the friction factor is given by:

$$f = \frac{64\zeta}{\mathrm{Re}_{d_{\mathrm{h}}}} \tag{B.2}$$

where the parameter ζ is related to the geometry of the annulus.

$$\zeta = \frac{(R - r_{\mathrm{b}})^2\left(R^2 - r_{\mathrm{b}}^2\right)}{R^4 - r_b^4 - \left(R^2 - r_{\mathrm{b}}^2\right)^2 / \ln(R/r_{\mathrm{b}})} \tag{B.3}$$

Appendix C Validation of the 2D Mass Transfer Model

The details of the finite volume code written to solve the conservation of mass, momentum, and species on a structured, two-dimensional grid are presented in Chapter 3. Various aspects of the code are isolated for validation. The continuity and momentum equation solvers are validated against the shear-driven cavity flow problem and the species equation solver is validated against a Couette flow mass transfer problem. There is not an analytical solution to the shear-driven cavity flow problem, but the problem is commonly used for validation purposes. Results from my code are compared to the results from Ref. [146] and to the results obtained from the commercially available CFD code Fluent. The Couette flow mass transfer problem has an analytical solution, which is presented in detail in Ref. [102]. Comparison to the analytical solution on successively finer grids allows the order of accuracy of the discretization scheme to be checked.

The results of the validations show that the finite volume code successfully solves the governing equations of fluid flow in an axisymmetric domain with variable fluid properties and when there is a rapid rate of transverse mass transfer through a surface boundary. Both of these conditions are important in the model of the heterogeneous Zn(g) oxidation tubular flow reactor.

The Shear-driven cavity flow

The shear-driven cavity flow problem has square domain with sides of length L (Figure C-1). The west, south, and east walls are stationary and impermeable. The north wall translates at a constant rate U along the horizontal coordinate x. The shear induced by the motion of the north wall establishes circulation of fluid within the cavity. The benchmark velocity field is compared with the converged and grid independent velocity field predicted by my finite volume code in Figure C-2 for Re = 1000, which shows the horizontal

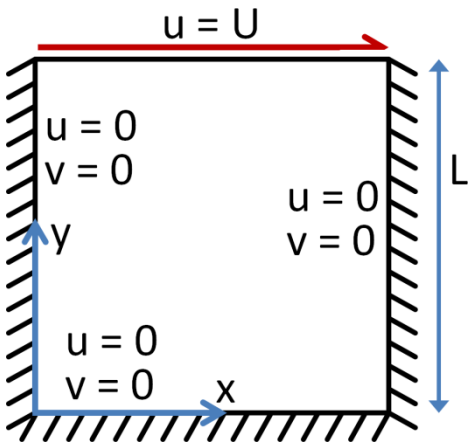

Figure C-1 The shear-driven cavity flow numerical domain and boundary conditions.

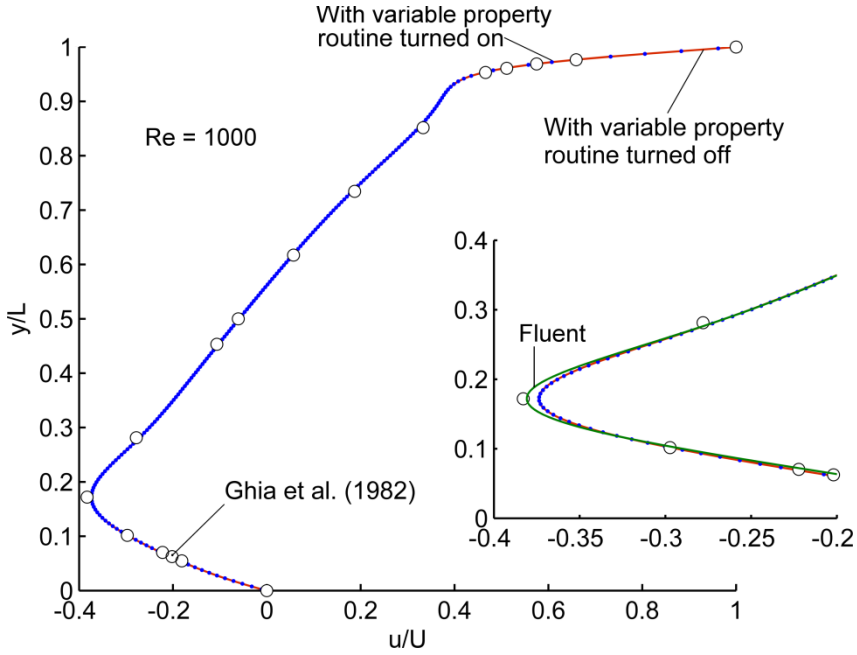

Figure C-2 The horizontal fluid velocity component along a vertical line at the geometric center of the cavity. The results with the variable fluid property routine turned on and off are compared with the benchmark solution given by Ref. [146] and, in the inset, with both the commercial CFD code Fluent and the solution given Ref. [146].

fluid velocity along a vertical line passing through the geometric center of the cavity. The maximum difference between the benchmark solution and the solution obtained from my code is 3%. Also included in the inset of Figure C-2 is the velocity obtained from Fluent. My code is in better agreement with the Fluent solution, with a maximum difference of 1.5%.

To check the variable property subroutine in my code, the shear-driven cavity flow problem was also solved with the variable property routines turned on, but while holding the properties fixed. The influence of the variable properties on the solution scheme is to add source terms in the discretized conservation of momentum equations. If the variable property routines are formulated correctly, the solver should converge to a solution in which these additional source terms are, within machine tolerance, zero. The horizontal velocity along the geometric center of the cavity computed with properties held fixed, but with the variable properties routine turned on is also shown in Figure C-2 with blue dots. The solution is indistinguishable from the solution in which the additional variable property viscous source terms were forced to zero, providing confidence that the variable property routines are correctly formulated and implemented in the 2D finite volume scheme.

The Couette flow mass transfer problem

To validate the species equation solver for conditions in which the net flux of mass across domain boundaries cannot be neglected, I used my code to solve for the mass transfer of a binary mixture in a fully-developed Couette flow with one species rapidly transported in the transverse direction. The problem geometry and boundary conditions are specified in Figure C-3. The flow channel has a height L. The lower interface is maintained by some mechanism external to the channel at a high concentration of species

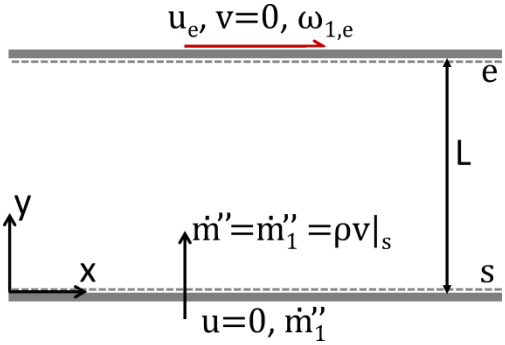

Figure C-3 The Couette-flow with the rapid transverse transfer of a single species in a binary mixture.

1, $\omega_{1,s}$, and is impermeable to species 2. There is thus a net transfer of *only* species 1 into the channel. The upper interface is maintained free of species 1 by a mechanism outside of the channel, i.e., $\omega_{1,e} = 0$, and is also impermeable to species 2. It is assumed that the system is isothermal and that the density and binary diffusivity are constant.

The analytical solution to this problem is given by Mills [102]. It is derived by solving the continuity and species conservation equations in the flow. For fully developed conditions, the solution is:

$$\frac{\omega_1 - 1}{\omega_{1,s} - 1} = e^{\left(\frac{\dot{m}'' y}{\rho \mathfrak{D}_{12}}\right)} \tag{C.1}$$

There are two types of problems. In the first type, the net rate of transfer of species 1, $\dot{m}''$, is known at $y = 0$. In this case, equation (C.1) is used to determine the mass fraction of species 1 at surface s by solving for $\omega_{1,s}$ with $y = 0$. Having determined the value of $\omega_{1,s}$, equation (C.1) may be used to plot the species 1 mass fraction profile. In the second type of problem, the mass fraction of species 1 is known at $y = 0$, and equation (C.1) is first used to determine the net rate of transfer of species 1, $\dot{m}''$. Equation (C.1).may then be used to plot the species 1 mass fraction profile, $\omega_1(y)$.

I validated my code using both types of problems by comparing the numerical result to the analytical result. For brevity, the comparison of the numerical and analytical results for the second type of problem is in Figure C-4. The net rate of transfer of species 1 across the channel is fixed to be 0.25 kg/s, the height of the channel is L = 1 m, and the product of the density and diffusivity is assigned a value of unity. The maximum difference between the analytical mass fraction profile and the numerical mass fraction profile is 3×10^{-5} with 200 uniformly spaced finite-volume cells. As a check on the order of accuracy of the discretization scheme—which is central difference in the interior nodes and forward/backward difference at the boundary nodes—the numerical and analytical solutions were compared for successively finer grids. Figure C-5 shows that, as expected, the numerical solution is second order accurate in the interior of the numerical domain and

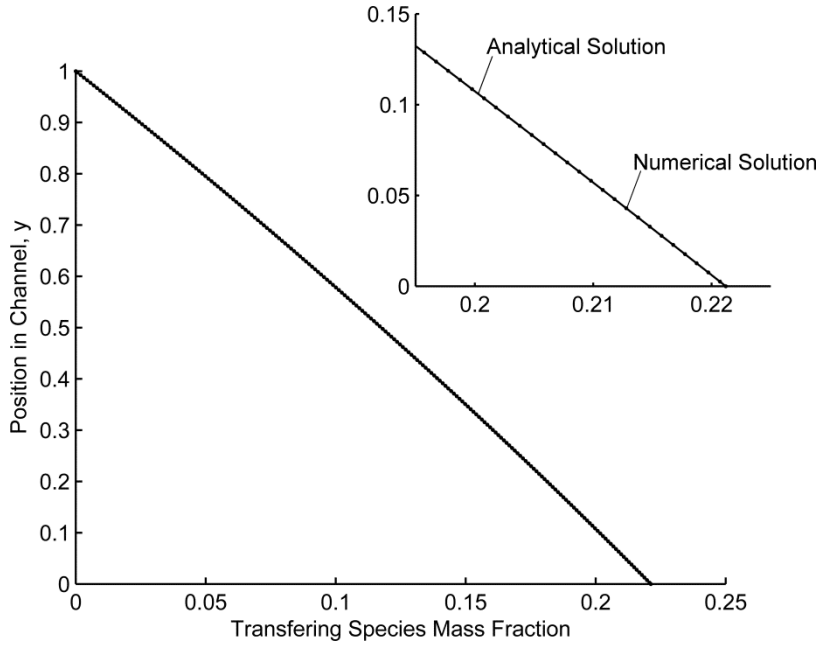

Figure C-4 Comparison of the numerical and analytical solutions to the high mass transfer rate Couette-flow problem. The transferred species is transported across the L=1 m tall channel at 0.25 kg/s ($\rho\mathfrak{D}_{12}$=1.)

first order accurate at the boundaries of the numerical domain, consistent with the central difference and forward/backward difference discretization schemes.

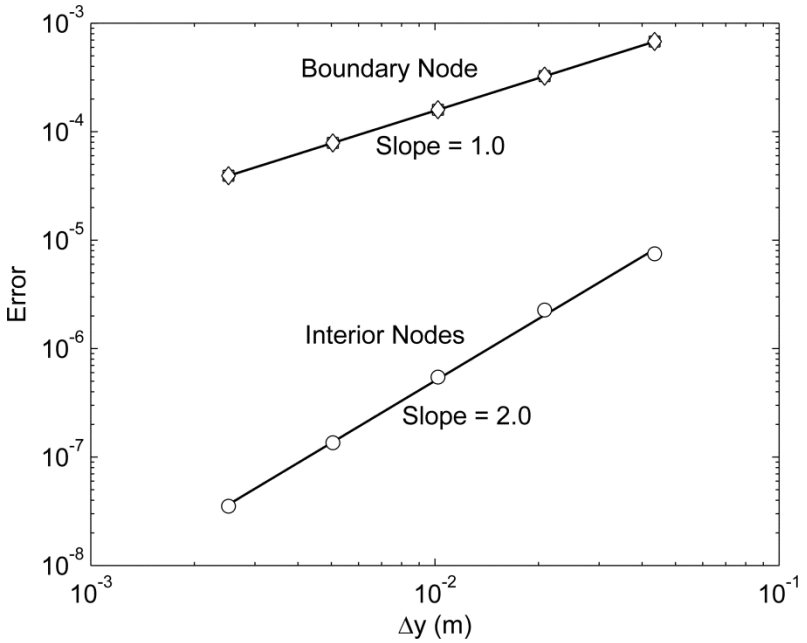

Figure C-5 The difference between the analytical and numerical solutions at the interior of the numerical domain and at the boundary of the numerical domain for successively finer grids. The slope of the best fit lines correspond to the order of accuracy of the numerical discretization scheme.

Appendix D Derivation of the Precursor Mechanism Rate Equation

The precursor mechanism is postulated to explain the apparent negative activation energy of the heterogeneous oxidation of Zn(g) by H_2O over the temperature range from 800 to 1050 K in Chapter 3. Here I derive the overall rate equation for the mechanism that relates the concentrations of the reacting species in the gas to the rate of the heterogeneous oxidation.

The precursor mechanism consists of two elementary chemical steps, given in equations (3.28) and (3.29) in Chapter 3. In the derivation that follows, the variables associated with the first step, equation (3.28), are denoted with a subscript '1'; the variables associated with the second step, equation (3.29), are denoted with a subscript '2'. The second step is assumed to be the rate-limiting step in the sequence, and the first step is assumed to be quasi-equilibrated. As such, the overall rate of the heterogeneous oxidation of Zn(g) is controlled by the rate of the second step:

$$r_2 = k_2[(H_2O)][Zn(g)] \tag{D.1}$$

k_2 is the forward reaction rate parameter, $[Zn(g)]$ is the concentration of gas phase Zn, and $[(H_2O)]$ is the concentration of adsorbed H_2O on the ZnO surface. The exact details of the adsorbed H_2O are unknown for the temperatures of the present study, but likely the H_2O molecules exist as surface hydroxyl groups with the oxygen atom nearest to the ZnO surface and the hydrogen atoms extending away from the surface. The stable formation of $Zn(OH)_2$ is reported for temperatures between 373 and 448 K [57].

The quasi-equilibrated rate of the first chemical step is given as:

$$r_1 = k_1[H_2O][*] - k_{-1}[(H_2O)] \cong 0 \tag{D.2}$$

k_1 and k_{-1} are the forward and reverse reaction rate parameters, $[H_2O]$ is the concentration of water in the gas phase, and $[*]$ denotes an available oxidation site on the ZnO surface. In quasi-equilibrium, the rate of the adsorption of H_2O is balanced by the rate of desorption of H_2O, and equation (D.2) provides a relationship relating the partial pressure of H_2O to the concentrations of vacant and occupied oxidation sites.

$$K = \frac{k_1}{k_{-1}} = \frac{[(H_2O)]}{[H_2O][*]} \tag{D.3}$$

One additional equation is required to provide and equation for r_2 that is a function of only the gas phase concentrations of water and Zn(g). This equation is provided by an oxidation site balance assuming that a fixed number of oxidation sites are available over a given area of ZnO:

$$[*]^o = [*] + [(H_2O)] \tag{D.4}$$

Substituting equation (D.3) into equation (D.4) provides an equation for the concentration of available oxidation sites:

$$[*] = \frac{[*]^o}{1 + K[(H_2O)]} \tag{D.5}$$

Equations (D.1), (D.3), and (D.5) are combined to obtain the desired expression for r_2:

$$r_2 = \frac{[*]^o k_2 K p_{H_2O} p_{Zn(g)}}{1 + K p_{H_2O}} \tag{D.6}$$

In equation (D.6), the concentrations of the H_2O and Zn(g) species in the gas phase are represented by their partial pressure, as is customary. The number of active sites is proportional to the area of the ZnO surface, and the specific rate of the heterogeneous oxidation of Zn(g) is,

$$r'' = \frac{r_2}{[*]^o} = \frac{k_2 K p_{H_2O} p_{Zn(g)}}{1 + K p_{H_2O}}, \tag{D.7}$$

which is equation (3.30) provided in Chapter 3.

Appendix E Constructing State Diagrams for Non-Stoichiometric Oxides

The CeO_2 $\delta - T - p_{O_2}$ state diagram shown in Chapter 5 was constructed using the thermodynamic data measured by Panlener *et al.* [117], who considered ranges of T, p_{O_2}, and δ relevant to solar thermochemical fuel production. The application of the data to calculate the non-stoichiometry for a given temperature and oxygen partial pressure is described below.

At equilibrium, the chemical potential of oxygen in the gas above ceria equals the chemical potential of the oxygen in the ceria (differences in the chemical potentials of oxygen in the solid and gas are what drive the oxidation or reduction of ceria). Treating the oxygen in the gas above ceria as ideal (an excellent assumption for the temperatures and pressures relevant to thermochemical fuel production), its chemical potential is given by:

$$\mu_{O_2^g} = \mu^o_{O_2^g}(T, p_{ref}) + RT \ln\left(\frac{p_{O_2^g}}{p_{ref}}\right) \tag{E.1}$$

The superscript 'g' on the O_2 indicates that the oxygen is in the gas phase. An 's' superscript will denote O_2 in the solid phase. The reference pressure, p_{ref}, is taken to be 1 atm, and for brevity will not be carried through in subsequent equations.

The chemical potential of oxygen in the solid is a much more complex function of temperature and ceria non-stoichiometry than the chemical potential of oxygen in the gas. The available thermodynamic models for the chemical potential of oxygen in the solid are only valid for lightly reduced ceria ($\delta \leq 0.05$) [35, 125], and therefore experiments like those completed in Ref. [117] are required to capture the non-stoichiometric behavior for deeper reduction. As noted, the chemical potential of oxygen in the gas and solid are equal at equilibrium so that

$$\mu_{O_2^s} = \mu_{O_2^g} = \mu^o_{O_2^g}(T) + RT\ln\left(p_{O_2^g}\right) \tag{E.2}$$

For convenience, equation (E.2) is rearranged to isolate the term with the oxygen partial pressure,

$$\Delta\bar{G}_{O_2^s} = \mu_{O_2^s} - \mu^o_{O_2^g}(T) = RT\ln\left(p_{O_2^g}\right), \tag{E.3}$$

and a partial molar Gibb's function of oxygen in the ceria is defined, $\Delta\bar{G}_{O_2^s}$. Equation (E.3) is a thermodynamic state equation, and fully defines the $CeO_{2-\delta}$ system at equilibrium. The non-stoichiometry is not explicitly represented in equation (E.3), but rather expressed implicitly through the partial molar Gibb's function. Using the definition of the Gibbs function,

$$\Delta\bar{G}_{O_2^s} = \Delta\bar{H}_{O_2^s} - T\Delta\bar{S}_{O_2^s}, \tag{E.4}$$

and dividing both sides of equation (E.3) by $-RT$ gives:

$$\left(\frac{\Delta\bar{S}_{O_2^s}}{R}\right) - \left(\frac{\Delta\bar{H}_{O_2^s}}{R}\right)\frac{1}{T} = -\ln\left(p_{O_2^g}\right) \tag{E.5}$$

The functional form of the transformed state equation (E.5) that of a line if the partial molar enthalpy and entropy functions ($\Delta\bar{H}_{O_2^s}$ and $\Delta\bar{S}_{O_2^s}$) are independent of temperature. Remarkably, for many non-stoichiometric solids, including ceria, temperature independence is observed. Exclusive dependence of the $\Delta\bar{H}_{O_2^s}$ and $\Delta\bar{S}_{O_2^s}$ functions on non-stoichiometry allows the thermodynamic state equation to be extrapolated to higher or lower temperatures than were used in the experiments to determine $\Delta\bar{H}_{O_2^s}(\delta)$ and $\Delta\bar{S}_{O_2^s}(\delta)$. This unique characteristic was taken advantage of in constructing Figure 5.1, which shows isotherms for temperatures higher than considered experimentally ($T \geq 1800$ K).

Appendix F Time Constant Analysis of the Pt-Pt/Rh Thermocouple Probe

The speed of the temperature response of the Pt-Pt/Rh thermocouple protected in an alumina sheath to changes in its environment is estimated by use of a step function input. I briefly describe the model of the thermocouple probe (wire + protective sheath) used to simulate the temperature response and I describe the application of the model to estimate the time response error in the IR imaging furnace system.

A schematic of the thermocouple probes is provided in Figure F-1. Consider an energy balance on the control volume with control surfaces indicated by the dashed line. For simplicity, it is assumed that the temperature is uniform in the control volume (lumped capacitance analysis), and that the probe exchanges energy with its surroundings via radiation. Conduction along the probe length is neglected. The conservation of energy in the control volume relates the rate at which energy is exchanged between the thermocouple probe and the surroundings and the rate at which energy is stored in the probe.

$$\frac{d\mathrm{E}}{dt} = \dot{Q} \tag{F.1}$$

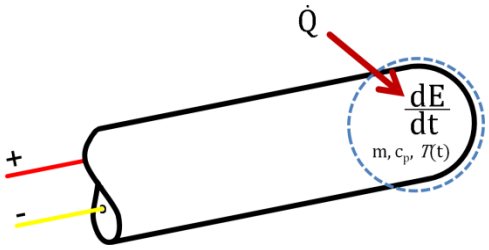

Figure F-1 Sketch of the Pt-Pt/Rh thermocouple protected in an alumina sheath, showing the control volume over which energy is balanced. Heat is transferred via radiation from the hot surfaces in the IR furnace system.

The change of energy in the thermocouple probe causes its temperature to change according to:

$$d\mathrm{E} = mc_p dT \tag{F.2}$$

Energy exchange with the surroundings is represented by Newton's Law of Cooling,

$$\dot{Q} = h_r A(T_\infty - T), \tag{F.3}$$

where h_r is the heat transfer coefficient and T_∞ is the temperature of the body that the thermocouple probe is in thermal contact with. For radiation, which is inherently non-linear, the heat transfer coefficient is highly dependent on both the temperature of the thermocouple probe and the temperature of the surface with which it exchanges energy, T_∞. Substituting equations (F.2) and (F.2) into equation (F.1) and rearranging provides an ordinary differential equation for the rate of temperature change of the thermocouple probe:

$$\frac{dT}{dt} = \frac{h_r A}{mc_p}(T_\infty - T) \tag{F.4}$$

Equation (F.4) is a linearized form of the non-linear radiation heat transfer problem, with the non-linearities lumped into the heat transfer coefficient, h_r. The time constant of the probe is defined as the ratio of the heat capacity of the probe to the heat transfer conductance:

$$\tau = \frac{mc_p}{h_r A} \tag{F.5}$$

The time constant, a measurement system dependent quantity, is not known *a priori*, and an experiment is conducted to obtain the time constant in the IR imaging furnace system. Substituting the definition of the time constant into equation (F.4) and rearranging the terms one last time provides another useful form of the ordinary differential equation:

$$\tau \frac{dT}{dt} + T = T_\infty \tag{F.6}$$

T_∞ need not be a constant, and if the time history of T is known, T_∞, the temperature that the thermocouple probe would measure if its time constant approached zero, can be calculated.

The time constant of the thermocouple probe in the IR furnace is measured by exposing it to a step change in temperature. The experimental set-up is identical to that used for thermochemical cycling of porous ceria (Figure 6.5), except that the there is no sample and alumina disk present, as shown in Figure F-2. For the time constant experiment, the IR furnace is set to a fixed power output, and allowed to thermally equilibrate over the course of hours. The fixed power output is maintained by holding the temperature of the control thermocouple, T1, at 1100 K. A second thermocouple, T2, initially located away from the center of the center of the concentrated IR irradiation is suddenly, at t = 0, plunged into the center and rapidly heated to a new steady-state temperature. The time history of the change, shown in Figure F-3, provides an estimate of the first-order time constant.

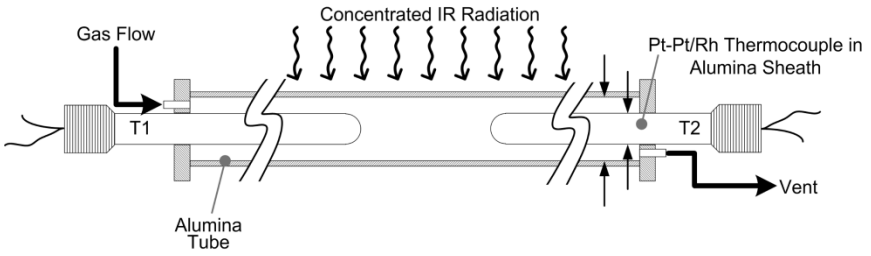

Figure F-2 The IR furnace reactor system, as set up for the thermocouple probe time constant experiment.

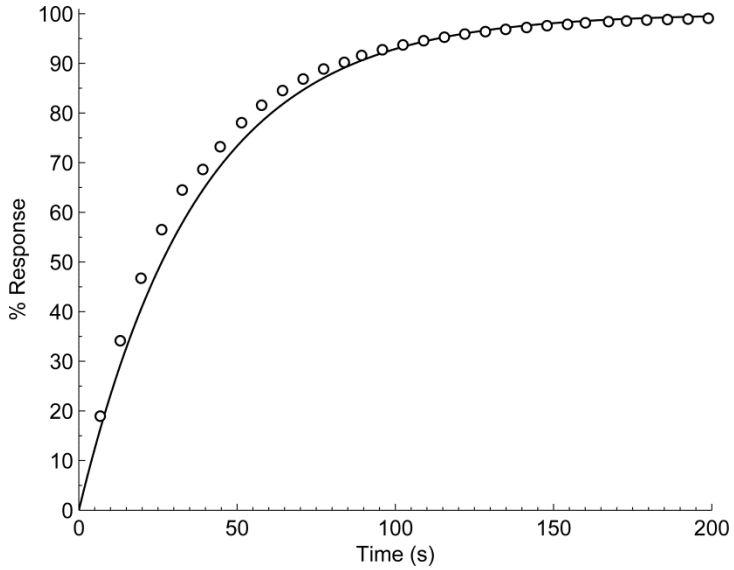

Figure F-3 The time response of the Pt-Pt/Rh thermocouple protected in an alumina sheath when exposed to a step change in temperature in the IR imaging furnace system

To extract the time constant from the data, the exact solution of equation (F.4) is used, as provided in Ref. [145]:

$$\Gamma(t) = \frac{T(t) - T_\infty}{T_o - T_\infty} = e^{-t/\tau} \tag{F.7}$$

where Γ is the "error fraction" of the output temperature, defined as the difference between the measured temperature and the temperature that would be measured for an infinitely fast response, normalized by the total change in temperature. Regression of the temperature response is most convenient by plotting the error fraction versus time on a semilog plot, which is equivalent to the transformation of equation (F.7) into:

$$\ln \Gamma = -\left(\frac{1}{\tau}\right) t \tag{F.8}$$

Equation (F.8) is in a linear form, and a curve fit through the data provides an estimate of the slope, which is related to the first-order time constant as shown. This analysis is

completed for the thermocouple probe response in the IR furnace system, and is shown in Figure F-4. The time constant, as determined from a linear regression, is 38± s.

With the time constant of the thermocouple probe in the IR furnace system in hand, the error incurred from the time lag of the thermocouple probe embedded in the ceria samples during the thermochemical cycling experiments is estimated. Equation (F.6) is used to correct the temperature measured by the thermocouple probe during thermochemical cycling, using the data for 3DOM CeO_2 as an example. The corrected, T_∞, and uncorrected, T, temperatures are shown in Figure F-5, along with the rates of O_2 and CO measured. When the furnace power is increased to rapidly heat the 3DOM CeO_2, the uncorrected temperature rises at a maximum rate of ~800 K/min. The corrected temperature shows that the heating rate is actually closer to 2000 K/min. The dramatic difference leads to substantial underreporting of the temperature. The maximum uncorrected temperature during reduction is 1470 K and the maximum corrected temperature during reduction is ~1800 K, a 300 K difference. The overshoot error leads to O_2 evolution above what would be expected based on the uncorrected temperature, and makes comparison to thermodynamic chemical equilibrium challenging. It is interesting to note that the peak rate of O_2 evolution occurs at approximately the same time at which the corrected temperature reaches a maximum, t = 145.7 min and t = 145.8 min in cycle 34, respectively. The correlation suggests that O_2 evolution from ceria is linked to the rate at which it can be heated, corroborating the results presented in Figure 6.10.

Similar to the overshoot error during the reduction half cycle, an undershoot error is incurred during the oxidation half cycle. The difference between the minimum uncorrected temperature and the minimum corrected temperature is ~200 K in any given cycle. The consequence of the undershoot error is that the kinetics of CO production are underpredicted. Furthermore, Figure F-5 shows that CO production occurs non-isothermally.

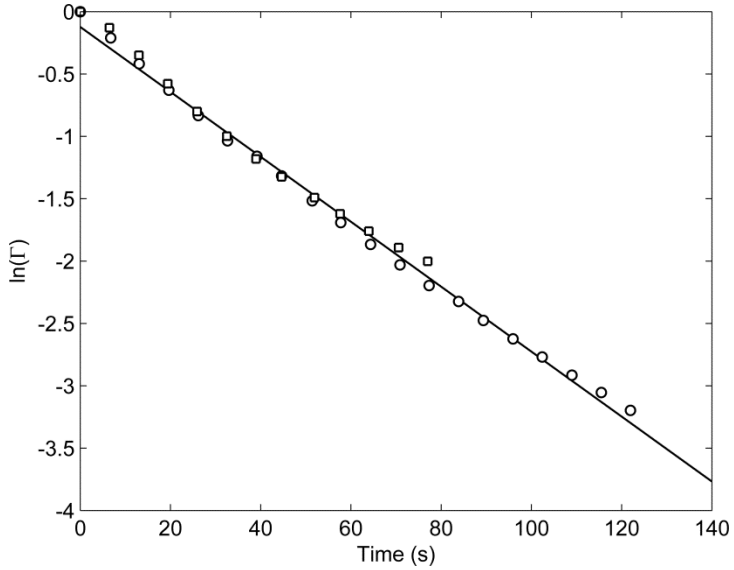

Figure F-4 Plot of the logarithm of the error fraction of the temperature response of the Pt-Pt/Rh based thermocouple probe (circles). The data for a repeat of the step change experiment is also shown to demonstrate repeatability (squares).

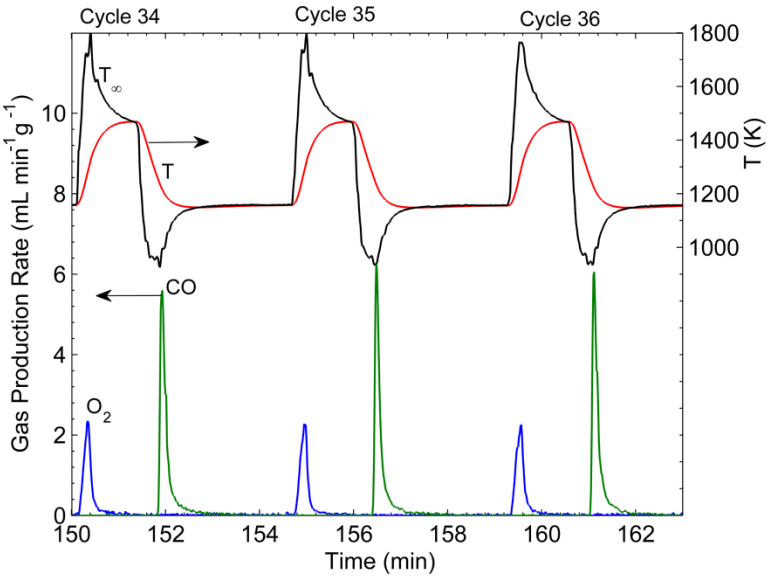

Figure F-5 The temperature recorded by the thermocouple probe embedded in the 3DOM CeO_2 during cycled 34-36, T, and the corresponding corrected temperature, T_∞. Also included in the figure are the rate of O_2 and CO production.

Appendix G Thermochemical Cycling Data

The rate of O_2 and CO production measured in every cycle and for every sample tested in the thermochemical cycling apparatus, along with the temperature measured by the thermocouple probe embedded in the sample, is compiled in this appendix. The data for commercial CeO_2 is presented first, followed by the data for 3DOM CeO_2, NOM CeO_2, and D-3DOM CeO_2. A baseline shift in the Raman laser gas analyzer over the first hour of cycling D-3DOM CeO_2 prevented the measurement of O_2. In Figure 6.11, O_2 productivity for the first 15 cycles is based on an extrapolation of data from cycles 20 to 30.

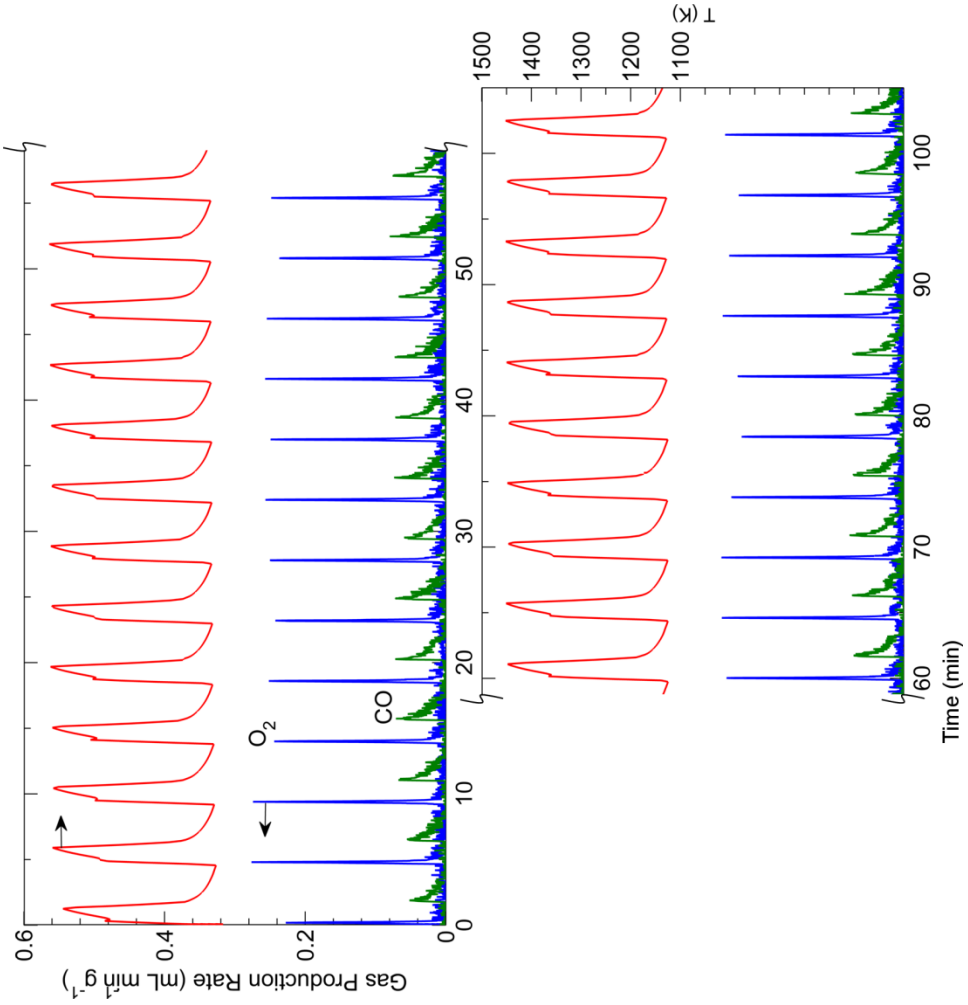

Figure G-1 The rate of O_2 (blue line) and CO (green line) production and the temperature measured by the Pt-Pt/Rh thermocouple probe embedded in the sample during 23 thermochemical cycles of the low porosity commercial CeO_2.

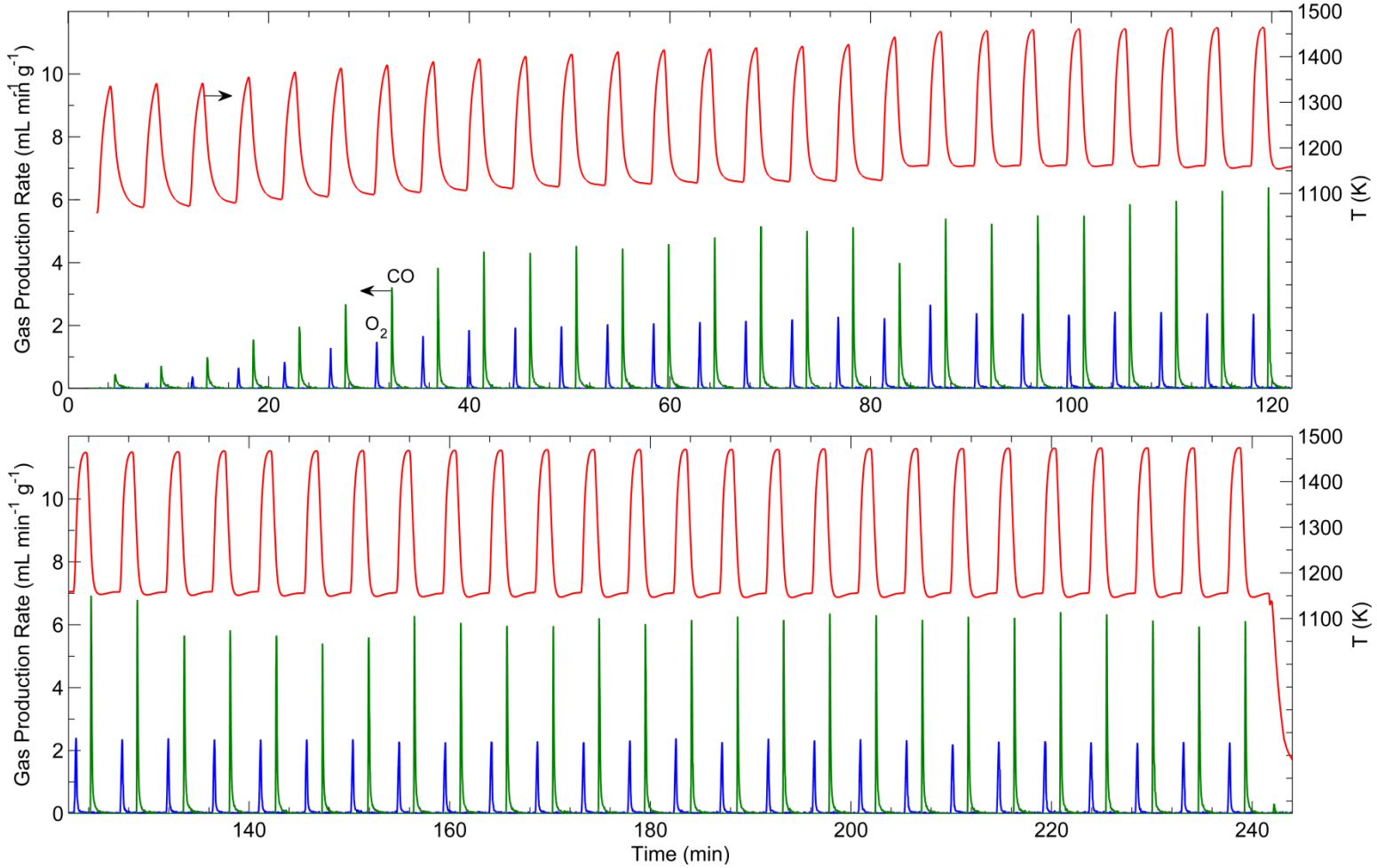

Figure G-2 The rate of O_2 (blue line) and CO (green line) production and the temperature measured by the Pt-Pt/Rh thermocouple probe embedded in the sample during 53 thermochemical cycles of 3DOM CeO_2.

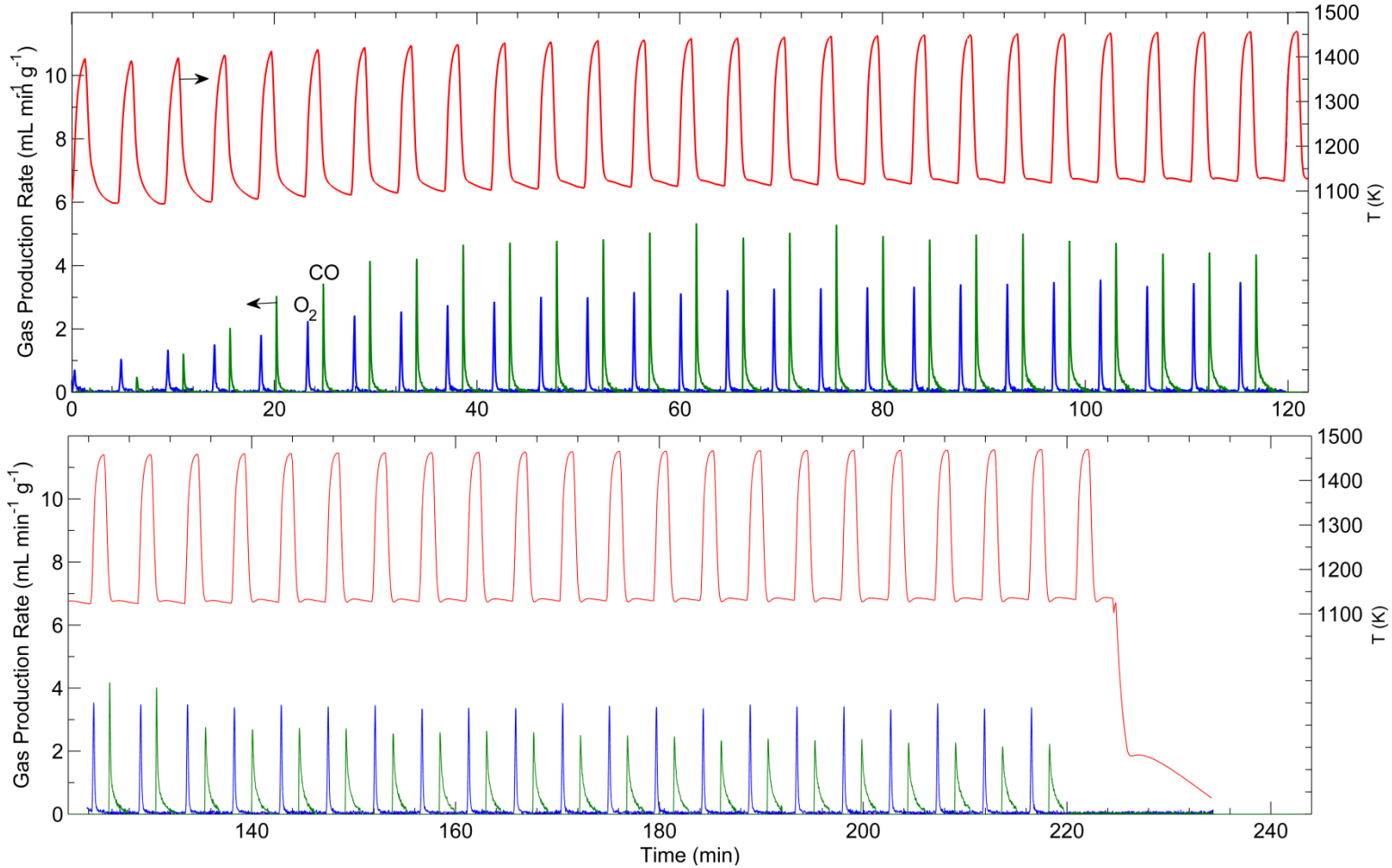

Figure G-3 The rate of O_2 (blue line) and CO (green line) production and the temperature measured by the Pt-Pt/Rh thermocouple probe embedded in the sample during 49 thermochemical cycles of NOM CeO_2.

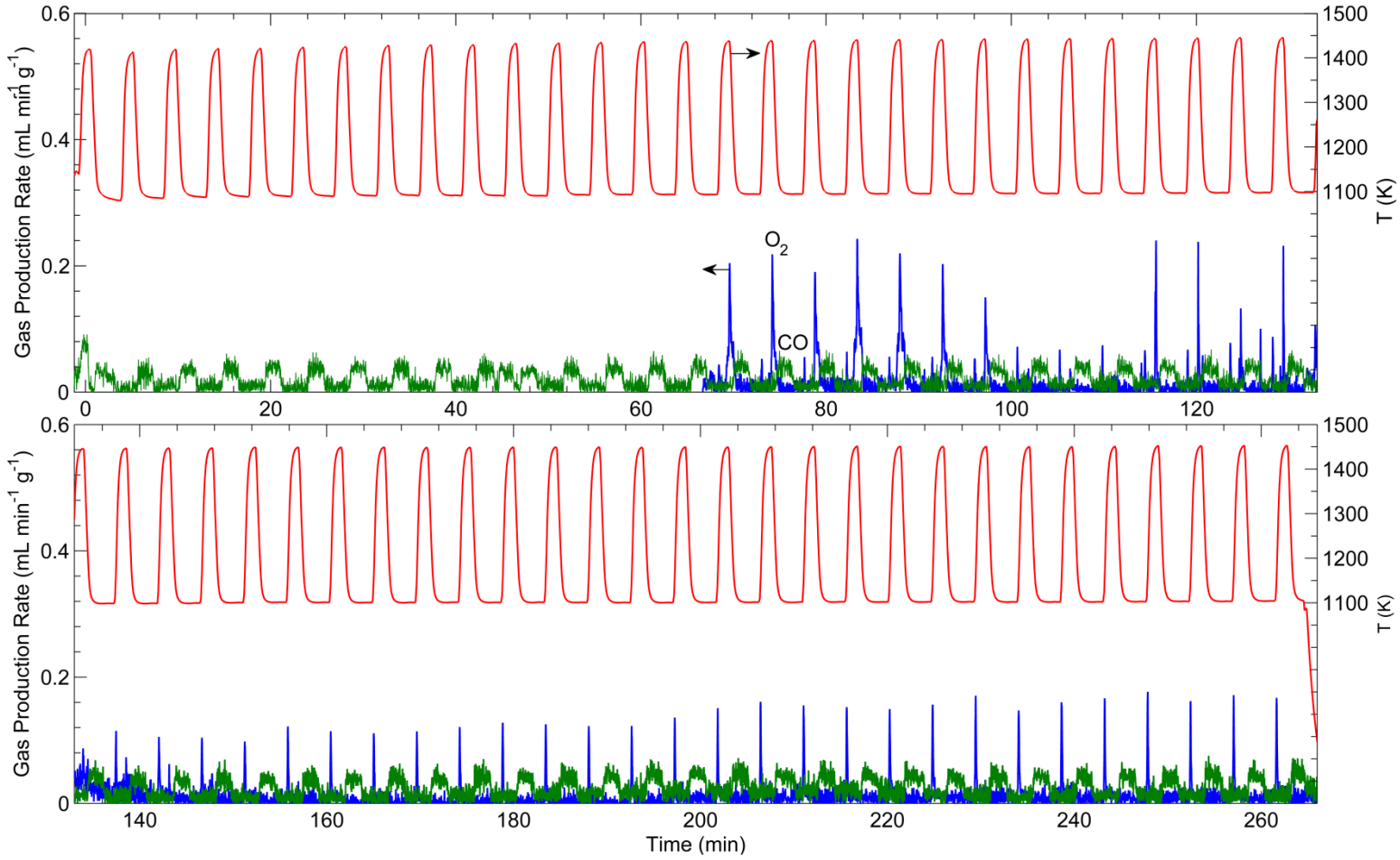

Figure G-4 The rate of O_2 (blue line) and CO (green line) production and the temperature measured by the Pt-Pt/Rh thermocouple probe embedded in the sample during thermochemical cycling of D-3DOM CeO_2.

Appendix H Copy of Letter Permitting Republishing of Journal Articles in Thesis

Luke Venstrom <venst001@umn.edu>

FW: ASME PUBLICATIONS PERMISSION REQUEST FORM SUBMISSION

1 message

Beth Darchi <DarchiB@asme.org> Fri, Jun 22, 2012 at 11:10 AM
To: "lvenstro@me.umn.edu" <lvenstro@me.umn.edu>

Dear Mr. Venstrom:

It is our pleasure to grant you permission to use the following ASME materials;

- "Splitting Water and Carbon Dioxide via the Heterogeneous Oxidation of Zinc Vapor: Thermodynamic Considerations", by Venstrom, L.J. and Davidson, J.H., Journal of Solar Energy Engineering, Volume 133, 2011

- Figures 1,4,5,6 and Tables 1,2 from "The Effects of Mophology on the Oxidation of Ceria by Water and Carbon Dioxide," by Venstrom, Petkovich, Rudisill, Stein, and Davidson, Journal of Solar Energy Engineering, Volume 134, 2012

as cited in your letter for inclusion in a Doctoral Thesis entitled The Oxidation of Zinc Vapor and Non-stoichiometric Ceria by Water and Carbon Dioxide to Produce Hydrogen and Carbon Monoxide to be published by University of Minnesota - Twin Cities.

Permission is granted for the specific use as stated herein and does not permit further use of the materials without proper authorization. Proper attribution must be made to the author(s) of the materials, and no alterations of the materials is permitted in any material manner.

As is customary, we request that you ensure full acknowledgment of this material, the author(s), source and ASME as original publisher. Acknowledgment must be retained on all pages printed and distributed.

Many thanks for your interest in ASME publications.

Sincerely,

Beth Darchi

Permissions & Copyrights

ASME, 3 Park Avenue

New York, NY 10016

T: 212-591-7700

F: 212-591-7841

E: darchib@asme.org

-----Original Message-----
From: webmaster@asme.org [mailto:webmaster@asme.org]
Sent: Thursday, June 21, 2012 2:47 PM
To: permissions@asme.org
Cc: lvenstro@me.umn.edu
Subject: ASME PUBLICATIONS PERMISSION REQUEST FORM SUBMISSION